Delft University of Technology

Department of Precision and Microsystems Engineering

Development of an Atomic Force Microscope

Name: Jan W. Obrebski

Report no: ME 10.014

Coach: Eric S. Buice, Jonathan Ellis, Jo Spronck

Professor: Rob Munnig Schmidt

Specialization: Mechatronic System Design

Type of report: MSc thesis

Date: 12th May 2010

Contents

Preface

This master report presents the development of an Atomic Force Microscope (AFM) vertical scanner for surface topography measurements. The report is organized in the following manner. Chapter 1 presents the executive summary of the research, Chapter 2 summarizes the AFM technology, Chapter 3 discusses the design of the AFM scanner, Chapter 4 presents the identification of the scanner and design of the feedback controller, Chapter 5 treats the calculation of the measurement uncertainty achievable with the scanner, and Chapter 6 presents conclusions and recommendations for further improvement.

Chapter 1

Executive summary

The culmination of this research resulted in a submission and acceptance to the 10^{th} eu**spen** international conference. The executive summary of this thesis is essentially the extended abstract submission, which has been modified from its original form due to updated results. The original conference proceedings is appended in Appendix B.

1.1 Abstract

This abstract presents the development of an Atomic Force Microscope (AFM) vertical scanner for surface topography measurements, which is composed of a single axis positioning stage with an integrated metrology system and AFM probe. The scanner is meant to track and measure a maximum topography step of 10 μm with a measurement resolution of less then 0.1 nm and an uncertainty of less than 10 nm (1σ) at a controllable bandwidth of at least 2 kHz.

1.2 Positioning stage

The design goal of the scanner positioning stage is to provide an accurate movement in one degree of freedom while constraining all other degrees of freedom without introducing errors due to friction and hysteresis. As can be seen in Figure 1.1 and 1.2, a monolithic flexure stage is chosen, constructed from aluminium and driven by a piezoelectric stacked actuator. Four leaf springs guide the moving element in a single direction (z-axis) with relatively low stiffness (0.5 N/μm) while the remaining degrees of freedom are constrained by the relatively high stiffness of the leaf springs. This ensures the stage guiding performance and immunity to straightness errors of the piezoelectric drive. The required stiffness of the piezoelectric actuator is determined by a first resonant frequency greater than 6 kHz to meet the desirable controller bandwidth. This leads to a stiffness of 12 N/μm. Using this combination a low actuation force level, less than 5 N, is achieved which limits the disturbance force and frame deformation on the structural frame that supports the capacitance gage used for position information and the AFM probe used for force feedback. The movable stage frame possesses circular and triangular cut-outs for mass reduction with moderate loss of stiffness. The presence of the triangular cut-outs yields a non-uniform stiffness distribution across the stage frame elements, which results

in a complex, higher order bending shape of the structure when an actuation force is applied. The cut-outs were designed to shape the stage deflection to minimize its net deformation affecting the displacement and force measurement. In this manner, the elastic deformation and the related measurement error was effectively reduced by 60%. The structure is optimized such that the higher resonance modes occur at frequencies greater than 8 kHz which allows for advanced control schemes and higher bandwidths. The picture of the assembled scanner is shown in Figure 1.2.

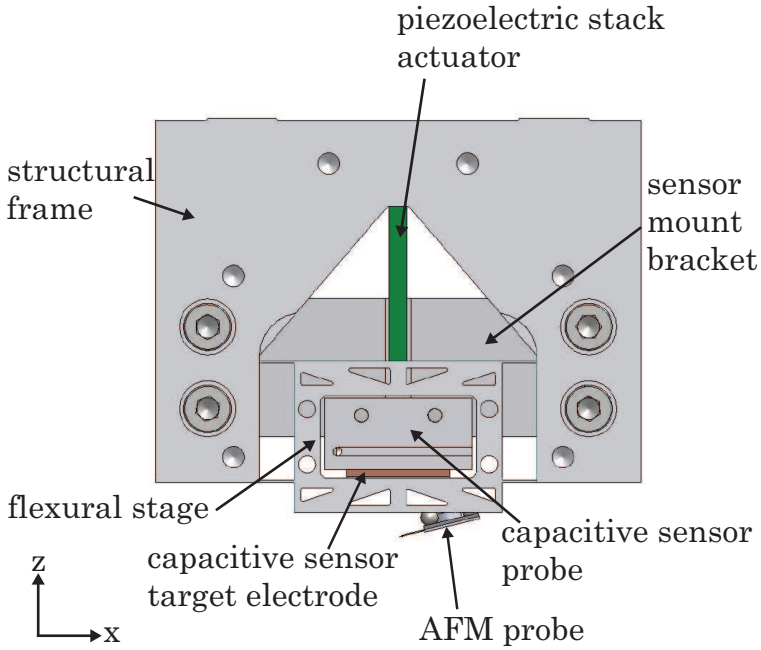

Figure 1.1: Partial assembly with front metrology bracket removed.

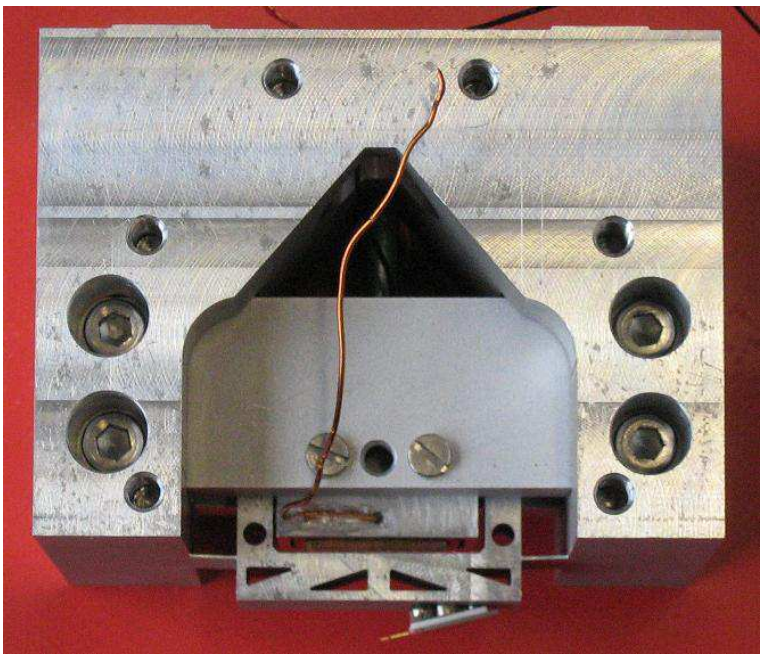

Figure 1.2: Picture of the assembled AFM scanner with cover removed.

1.3 Capacitive probe

The capacitive probe was developed together with the structural stage, such that the desired resolution and noise levels are achieved without imposing any constrains on the stage design. The capacitive probe is positioned inside the moving stage to obey the Abbé principle, see Figure 1.1. The capacitive probe is held by two brackets rigidly connected to the structural stationary frame of the stage, which allows for easy adjustment of the sensing gap between the probe electrode and the target electrode attached to the moving part of the stage. The metrology and force frame are not separated from each other due to the very small actuation forces in the force loop. Additionally, the squeeze film damping occurring between cap gauge probe and target electrodes was kept to a minimum to ensure that there are no appreciable forces acting on the electrodes when positioning at high velocity, preventing deformation of the electrodes and/or the structural frame. The capacitive sensor signal demodulation is performed by an AC demodulation bridge [1]. The capacitive sensor was additionally calibrated by the laser interferometer of 1 nm measurement uncertainty.

1.4 AFM probe

The AFM probe used is a commercial self-sensing and self-actuating Akiyama probe [2], which does not require an external shaker nor a detection system, thus providing a compact configuration. The probe is mounted to the stage by means of a kinematic mount consisting of 3 spheres, a pre-loading magnet and magnetic steel plate, which yields a good repeatability of the mount when exchanging the probe. Additionally, the probe wiring is soldered to the silver pads painted on a layer of UV glue which covers the pre-loading plate, creating an electrical

contact with the probe. The pre-amplification circuit for the Akiyama probe is integrated into the stage assembly in order to keep the probe wiring as short as possible and hence to minimize the parasitic effects. The electronic circuits for Akiyama probe excitation and modulation of its oscillation frequency were realized.

1.5 Feedback controller

The positioning stage dynamics was identified via the laser vibrometer frequency response experiments. The obtained transfer functions confirmed the analytical and FEM models used in the research. Additionally, the frequency response was measured by the capacitive position feedback sensor and was the the autoregressive model with exogenous input (ARX) was developed for the feedback controller design. The designed PI controller with a notch filter was successfully implemented and the closed loop bandwidth of over 2 kHz was achieved. Figures 1.3 and 1.4 show the measured closed loop frequency response and a 13 μm step response, respectively.

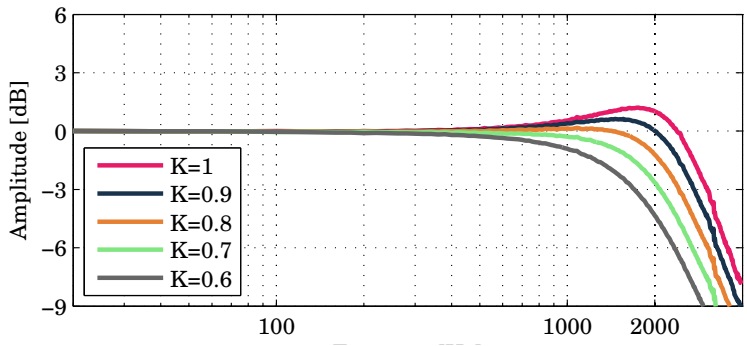

Figure 1.3: Closed loop frequency response for different controller gains.

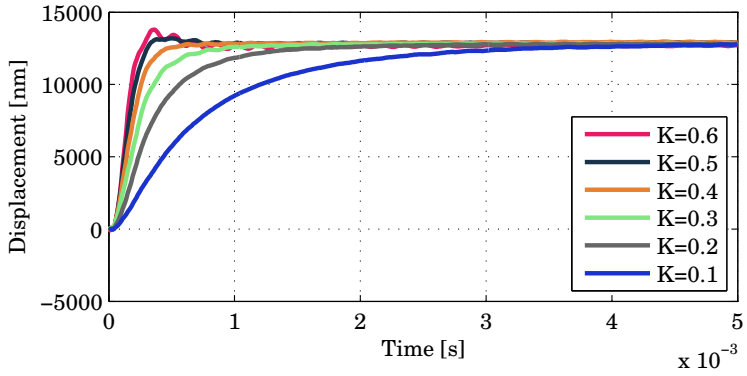

Figure 1.4: Stage response to a 13 μm step input for different controller gains.

1.6 Error budget

An error analysis was performed to determine not only the overall error of the system, but also to see which components are the most significant contributors to improve in the future. The error contributors considered during this investigation are: thermal expansion, Abbé and Cosine errors, scanner elastic deformation, static calibration uncertainty of the capacitance gage sensor, capacitance gage and amplifier noise, and elastic deformation of the capacitance gage electrode. The individual error contribution values are listed in Table 1.1, resulting in an overall error estimation of 2 nm (1σ). From Table 1.1, it can be seen that the largest error contribution is a result from the structural frame elastic deformation due to the actuation force. . Additionally, there is a significant error due to the thermal variations of the temperature controlled environment followed by the scanner elastic deformation. The thermal expansion causes a spurious force feedback due to thermal growth of the scanner and the erroneous position feedback due to the capacitive sensor gap change. The scanner elastic deformation is caused mainly by the stress induced in the stationary structural frame by the frequency dependent piezoelectric actuation forces. In order to limit the related error, the movable mass was reduced to minimize the inertia forces and the stationary structural frame was designed for the high stiffness with additional stiffening obtained from metrology frame brackets.

Table 1.1: Error contributions and their values.

Component	Variance [nm^2]	Standard deviation [nm]
Thermal expansion	0.64	0.8
Scanner elastic deformation	1.44	1.2
Static calibration uncertainty	1	1
Abbé and cosine errors	0.504	0.71
Capacitive sensor/amplifier noise	0.49	0.7
Capacitive sensor elastic deformation	0.16	0.4
Total	4.25	2

Chapter 2

Atomic Force Microscopy

2.1 Introduction

The first Atomic Force Microscope (AFM) was reported in 1986 [3]. The name originates because the AFM is directly measuring intermolecular forces with atomic resolution. There has been extensive investigations and studies on the AFM technology in physics, biology, chemistry, electronics, materials (especially polymers), and manufacturing, etc. Several techniques have been utilized for probe sensing, e.g.: force, optical, thermal, magnetic or electrical interactions between probe and surface [4]. AFM is part of the scanning probe microscopes (SPM) family because the measurement is based on sample-probe interactions. More specifically, in AFM, the principle of interaction between the sample and the probe is based strictly on the force interaction, mostly inter atomic. This makes it part of scanning force microscope group (SFM). However, the class of AFM microscopes is limited to the probe surface interaction of the purely inter atomic nature [4]. AFM technology, which has already been present and developed for more than two decades, not only established new standards in a variety of scientific and industrial fields but, most importantly, set up new challenges and horizons for the future.

2.2 Working principle of AFM

There are numerous ways to build an AFM. Various modes of operation and modulation, different probes, numerous sensing and actuation techniques make it difficult to describe its working principle. Many papers describe the AFM's method of operation in one particular configuration, which narrows the viewpoint on the AFM technology. The description outlined in this section might seem oversimplified, however, it underlines the basic functional components of an AFM and the idea behind the technique without indicating any specific manner used to realize its functionality. A typical AFM system consists of a micro cantilever integrated with a sharp tip which together are being referred to as an AFM probe. The AFM measurement relies on the predefined, let us assume, horizontal sample-probe scan. In addition there is a vertical sample probe scan occurring simultaneously to maintain a constant contact force. The probe tip interacts with the measured sample due to the forces, F_{ts}, arising between the two. These forces are non-linear with respect to the tip sample vertical separation, z, as shown in

Figure 2.1(a)). The changing force affects the static and dynamic behaviour of the probe. This behaviour is measured by the AFM probe and kept at the constant level by the probe vertical positioning relative to the sample in a feedback loop. In this manner, the tip sample interaction force, F_{ts}, is maintained at a constant value and the change of the probe sample vertical position is an indication of the scanned surface topography. In AFM systems, there is typically a separate displacement sensor measuring the probe displacement that was necessary to maintain the constant force, F_{ts}. The measured displacement is the final measure of scanned topography. The operation of an AFM machine relies on the concept of 'nulling', being a specific case of feedback operation [5] as: *"The high sensitivity of a non-linear or rather variable phenomenon is exploited by using it as a sensor in a system that is driven to maintain a constant output value compared to some reference. The drive signal is taken as the output measurement"*. This idea was frequently put in practice also in other machines, like in Scanning Tunnelling Microscopes (STM) and in an assay balance [5]. To summarize, the 'nulling principle' deals with the non-linear force-distance relationship. Furthermore, the measurement of the probe's behaviour is easier than the direct measurement of the sample. In addition, the probe tip enables the suitable 'read out' of the atomic forces which are transduced directly by the cantilever to the feedback loop. An exemplary AFM scheme is depicted in Figure 2.1(b).

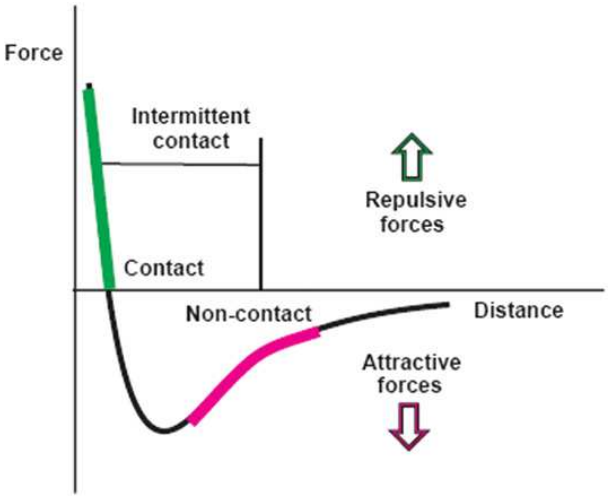

(a) SFM force-displacement curve; (Figure 1 from [6]).

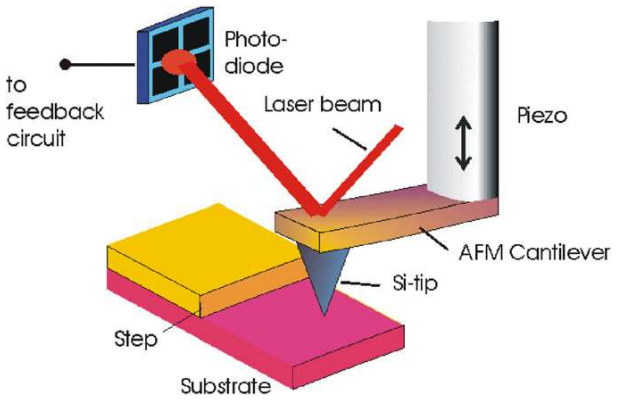

(b) Typical AFM schematic; (Figure 2 from [6]).

2.3 Operational modes

The following section describes possible AFM operational modes. Figure 2.1(a) shows the force, F_{ts}, curve between the end of an AFM (SFM) tip and the sample surface as a function of the distance, z, between them. Additionally, three different tip-sample interactions are indicated. While approaching the sample, the tip is attracted by long range (van der Waals) forces which initially increase as the tip gets closer to the sample. However, van der Waals attraction reaches its maximum at a certain distance and, approaching the sample from that point on, the attraction gets weaker until it finally drops down to a zero force balance and finally reverses

the direction of action, i.e. the tip is being repelled from the sample due to the dominance of the repulsive, short range, (Pauli) force. There are also many other force components to the interaction (which are discussed in a later section) and the force curve from Figure 2.1(a) indicates the dominant, attractive and repulsive regions together with their non-linearity and non-monotonicity. It is clear that the force curve is much steeper at a small separation distance and that the force curve changes its slope in the repulsive region. Figure 2.1(a) divides the approach curve into three regions, namely non-contact, intermittent contact, and contact mode. Due to the complexity of physical effects on the atomic scale level, it is difficult to indicate at which particular point the tip is in contact with the surface [6]. The contact mode is referred to as a static mode, while the non-contact or intermittent contact modes are called dynamic modes [4]. The following sections discuss these modes in further detail.

2.3.1 Contact operational mode

Contact operational mode (C AFM), or alternatively 'repulsive mode' [7], was the first technique in which AFM imaging was demonstrated. C AFM probe sensing is performed merely in the steep repulsive regime with a very sensitive force-distance relation. The measurement technique is as follows. The AFM probe is brought in contact with the sample and an initial interaction force, F_{ts}, is exerted on the probe resulting in the cantilever deflection setpoint. A typical range of contact force is between 10^{-6} N and 10^{-7} N [8]. The varying interaction force changes the deflection of the probe cantilever according to the Hook's law. The probe tip and cantilever work mechanically in series, hence the cantilever is typically by far more compliant than the tip [9]. Under this condition the cantilever bending is a valid indication of the interaction forces. During horizontal scanning the cantilever deflection, z_c, is kept constant by the vertical positioning system. The positioning system displacement necessary to achieve this provides the topography/force change [6]. Mathematically, one can retrieve the image by mapping $z(x, y, F_{ts} = \text{const.})$ [9], where z is the registered probe vertical position and x and y represent the coordinates at which the data point is taken. Atomic resolution is achievable in C AFM, however, it is difficult to implement it in practice [9]. C AFM suffers from a number of limitations [9]. Similarly to classic stylus instruments, a common problem in AFM is the tip damage caused by shear forces arising from adhesion and friction [9]. This introduces additional measurement uncertainties and might require additional tip characterization or replacement. Besides, short range forces are very strong and this might discriminate this technique in some cases as it can cause wear on atomic scales or tip shearing from the cantilever [6]. Another issue is the instability of the probe. This may happen if [9]

$$k < max\left(\frac{\partial^2 V_{ts}}{\partial z^2}\right) = k_{ts}^{max}, \tag{2.1}$$

where k is the cantilever stiffness, V_{ts} is the tip-sample interaction potential, and k_{ts} is the force curve slope in Figure 2.1(a). The reason for instability is the cantilever has a lower stiffness than the interaction force gradient, which typically results in the phenomenon of 'snap into contact' or 'jump into contact' [9]. The slope of the force curve changes depending on the operation point. Conversely, the slope of the cantilever force curve (which is its stiffness)

is nominally constant for all the operational points. In other words, at some point on the force curve, the attractive force becomes higher than the cantilever elastic force and thus the cantilever is pulled towards the sample surface. Further, in C AFM, long range interaction forces are directly fed into the imaging signal, which is decreasing the imaging resolution [9]. The best resolution is achieved if the interaction between the probe and the sample is between the tip and the sample atoms. However, in C-AFM, the rest of the probe may also interact with the sample. Another disadvantage is the low frequency $1/f$ or 'pink' noise that is difficult to be eliminated in the static AFM [9]. The typical scanning speeds of C AFM are of the order on 75 μm/ [6]; however the imaging speed is dependent on vertical scanner bandwidth and surface topography.

2.3.2 Dynamic operational mode

In dynamic mode AFM, the cantilever is oscillating and its position is servo controlled to maintain a constant force between the tip and the sample [6]. The oscillation of the probe is very close to its natural frequency, f_0 [9], and must have a drive signal. The vertical AFM scanner is not sufficiently fast to shake the probe [10], thus external shakers must be utilized. There are a number of techniques used to excite the cantilever, such as piezoelectric [11, 12], magnetic [10], thermal bimorph [13, 14], electrostatic [15] and acoustic [10]. There is a distinction between two possible dynamic scanning techniques, which depend on the relative probe-sample distance while scanning. If the probe does not come into physical contact with the sample in any part of the oscillation cycle, this the non-contact (NC) AFM. If contact is made it, is referred to as intermittent contact (IC). In the case of NC AFM, the amplitude of oscillation is typically between 5 nm and 15 nm [7]. This is much less than the average tip-sample distance. The oscillation must be small enough to register dynamic changes introduced by weak, long distance force interactions [7]. In NC AFM, the force interaction may be either both repulsive and attractive or just attractive [6], which depends on how close to the surface the probe is positioned. The range of these interaction forces is 10-12 pN [7]. This relatively low force might be considered as a disadvantage, since the resolution of measurement is low; however, it can be seen as an advantage when non-destructive sample examination is desired (e.g. in bioscience). NC AFM is relatively rarely used in standard imaging applications [4], however it has applications in study of strong magnetic structures and is referred to as Magnetic Force Microscopy [6]. In the case of an alternative dynamic mode, namely the intermittent contact (IC) AFM mode (also called 'tapping mode'), the situation is reversed. The amplitude of probe oscillation is bigger than the probe sample separation [16]. Furthermore, when fully extended, the tip 'taps' the sample atoms and is subjected to the short range repulsive forces. IC AFM mode involves strong probe-sample interaction (i.e. repulsive forces), similar to the C AFM and thus provides much better measurement resolution than NC AFM [9]. In IC AFM the probe is excited at amplitudes typically in the range of 20-100 nm [7]. As for the working mechanism of dynamic AFM measurement one should note that the tip-sample interaction is reflected in the actual probe oscillation characteristics, such as amplitude, phase, or natural frequency of vibration. There are techniques which use these quantities as an input to the feedback loop

when tracking surface topography [16]. Because the probe and sample interact for a certain time without physical contact, the horizontal scanning in dynamic AFM can be faster than in C AFM and on average is performed at the rates from 180 μm/s to 250 μm/s [6]. The speed limit in this case is imposed by the vertical positioning time constant [6], rather than by the sample topography. However the sample flatness still has some influence on the measurement speed [6]. Two major techniques are used to servo control the cantilever in dynamic mode AFM: amplitude modulation (AM) and frequency modulation (FM). Additionally, phase modulation (PM) is sometimes used, but much less than AM or FM modes. In all three modulation techniques the cantilever is excited at the resonant frequency, f_0, or reasonably close to it with a fixed amplitude, A_0, [6]. In AM the vertical position of the cantilever is varied to maintain a constant vibration amplitude and consequently, a constant tip-sample distance [6]. The major limitation of AM is that the vibrational amplitude changes with a time constant, t_{AM}, defined as [6]

$$t_{AM} = \frac{2Q}{f_0}, \tag{2.2}$$

where Q is the mechanical quality factor. This modulation technique is too slow for environments with a high Q, such as vacuum [9]. This limitation motivates the use of frequency modulation, which is independent of the quality factor. In frequency modulation mode, the cantilever tip is positioned relative to the sample surface to maintain a constant cantilever oscillation frequency set point [16]. The time constant for FM is given by [6]

$$t_{FM} = \frac{1}{f_0}. \tag{2.3}$$

By overcoming the quality factor dependency for AM, FM is the preferred choice in dynamic AFM operations [9]. In PM mode, the change in phase of the cantilever is observed and is subsequently used for the vertical feedback. PM mode is relativity difficult to implement when compared to AM and FM mode operation, and as such is less frequently used as a feedback mechanism [10]. However, it is common to monitor the change in phase of the measured signal, while utilizing AM or FM as the feedback mechanism, to measure other surface properties such as energy dissipation [10].

2.3.3 Static mode versus dynamic mode

Some static mode limitations can be solved by operating in dynamic mode. The large advantage of dynamic AFM is achieving the smaller probe degradation by adhesion and friction diminishing effects [7]. However other C AFM limitations may also be eliminated in dynamic AFM [9]. One such limitation is the cantilever stability encountered in C AFM. The instability problem of soft cantilevers in C AFM [9] can be solved by oscillating the cantilever at an amplitude, A, which is large enough to provide a restoring force, i.e.

$$kA = max(-F_{ts}(z)). \tag{2.4}$$

Further, the low frequency $1/f$ noise can be reduced in dynamic AFM if the natural frequency of the cantilever f_0 is higher than the $1/f$ noise corner frequency [9]. Lastly, in FM AFM,

the attenuation of the long-range force contributions to the imagining signal may be achieved by a proper choice of the cantilever oscillation amplitude A, which should be small and the probe average position should be close to the surface [9]. To summarize, although the dynamic AFM reduces some of the C AFM limitations, they both face the problem of a non-monolithic imaging signal, which means the interaction force changes non-monolithically along the tip-sample distance range which is an issue for feedback control [9]. The following section briefly discusses the forces present between the SFM tip and sample.

2.4 Tip-sample forces

There are several interaction forces between the probe tip and the sample in SFM. Thus far the discussion of the tip-sample interaction was referring to Figure 2.1(a), which describes van der Waals and Pauli repulsive contributions. This curve is based on the so-called Lennard-Jones (L-J) potential theory. The L-J potential, $V_{L-J}(z)$, is given by [6]:

$$V_{L-J}(z) = -4\epsilon_{L-J}\left[\left(\frac{\sigma_{L-J}}{z}\right)^6 - \left(\frac{\sigma_{L-J}}{z}\right)^{12}\right], \tag{2.5}$$

where σ_{L-J} is the position of the minimum potential, ϵ_{L-J} is the depth of the minimum potential, and z is the tip-sample distance. This L-J potential results in the interaction force, $F_{L-J}(z)$, govern by[10]

$$F_{L-J}(z) = k_{L-J}\left[-\left(\frac{\sigma_{L-J}}{z}\right)^2 + \frac{1}{30}\left(\frac{\sigma_{L-J}}{z}\right)^8\right], \tag{2.6}$$

where k_{L-J} is a constant depending on tip and sample geometries and materials. In Equation (2.6) the attractive Van der Waals component (the first term) and the repulsive Pauli component (the second term) are clearly distinguished [10]. This relationship shows the repulsive term dominates at the shorter distances, due to the near six order magnitude difference. As the tip further approaches the sample, the repulsive Pauli force becomes dominant [6]. In order to provide a quantitative distinction between the tip-sample interaction types, the short range forces (Pauli) act in the range of 1 nm [9] and the long range van der Waals forces act in the range of 100 nm in vacuum [9]. The Pauli force is caused by overlapping electron orbitals when the atoms are very close to each other [6]. Van der Waals force is caused by three major force contributors: the orientation force between molecules due to the dipole moment they both posses, the induction force between a polar and non-polar molecule (also referred to as the Debye force) and a dispersion force between the non-polar molecules (also referred to as the London force) [6]. The discussion of the tip-sample should not be limited exclusively to the L-J potential forces. Other forces present in the tip-sample interaction are: adhesive forces, capillary forces, electrical forces, magnetic forces, chemical forces and elastic contact forces. These forces are comprehensively described and discussed in the context of AFM/SFM by Buice [17] and Yacoot and Koenders [6].

2.5 AFM probes

2.5.1 AFM cantilevers

The typical AFM cantilever is a slender beam with a rectangular cross section, referred to as a 'diving board' cantilever [10]. Common dimensions, spring constants, and resonant frequencies of these cantilevers are listed in Table 2.1. There also exist other cantilever shapes, such as the

Table 2.1: Typical rectangular bar cantilevers in AFM, (Table II from [10]).

Parameter	Value range	Contact	N-C	I-C
Width [μm]	25-60	50	28	30
Thickness [μm]	0.7-7.5	2	3	4
Spring constant [N/m]	0.01-91	<0.2	3	40
Resonant frequency [kHz]	7-420	20	75	300

triangular truss [10] however they are not frequently encountered neither in scientific publications nor commercial probe designs. The triangular design has the advantage of having a higher stiffness against torsion and is typically used in C AFM [10]. The remaining part of this section is devoted to the 'diving board' design. AFM cantilevers are sensitive to bending but are also significantly sensitive towards torsion [18, 10]. The typical topography imaging cantilever relies on the bending of the clamped cantilever, however there are cantilever designs which are twisting in a 'torsional tapping' operation [19]. This is accomplished by placing the tip at an offset position from the centre line of the cantilever, which introduces the torsional moment on the cantilever while tapping the surface [10, 20]. Even though torsional cantilevers allow probe oscillation at higher frequencies, the most dominant probe architecture is a rectangular, symmetric prism cantilever. The manufacturing technology of cantilevers has developed rapidly in the recent years, providing a mass produced and reliable product [6]. AFM cantilevers are typically comprised of mono crystalline silicon (Si) and silicon nitride (Si_3N_4) [10]. A comprehensive summary of physical materials used in typical AFM cantilevers and their properties are listed in Yacoot and Koenders [6] in Table 1. From the Table 2.1 that the particular cantilever design depends on the application and operational mode. Both in static and dynamic modes, the probe resonance frequency, f_0, should be high enough to achieve a fast detection response. In C AFM, f_0 is much higher than the desired detection bandwidth, in order to prevent resonant excitation of the cantilever, where the resonance frequency is in the order of 10 kHz [9]. In dynamic AFM, the probe is stimulated at its natural frequency, which is typically in a range of from 10 to 1100 kHz [9], which allows higher scanning bandwidth. A high f_0 may be obtained in two ways: using short cantilevers (optimization) or artificially lowering the effective quality factor of the probe (Q control [21]). Static mode cantilevers are more compliant when compared to the dynamic mode cantilevers in order to achieve a higher sensitivity to the bending moment which increases measurement sensitivity. The low cantilever stiffness is also less invasive to the sample or tip. The above discussion creates a requirement on the probe to have a high resonance and low stiffness not mutually exclusive. Optimization for low mass is the way to achieve it [22]. As far as the geometry of cantilever, the short cantilevers were

reported to suffer less noise due to thermal motion, and can be used to image at higher scan speeds in tapping mode [23]. Another requirement for the cantilever would be the small electrical resistance to avoid building up an electrical potential at the probe tip [4]. The quality factor of the probe Q is another important feature of the probe. On one hand, a high Q increases the measurement sensitivity in the dynamic modes. However it limits the achievable bandwidth in AM AFM [4, 6]. This contradiction is overcome by FM AFM, described in the former section. Some cantilevers require special reflective coatings (mostly aluminium or chromium/gold [24]) to improve reflectivity of the face used in an optical read-out system, which is described later. Both Garcia [16] and Yacoot and Koenders [6] treat this topic extensively.

2.5.2 Detection methods

The following section describes the potential detection methods of AFM probe sensing. AFM detection means the measurement of dynamic or static behaviour of the probe [4], which is the geometrical response of a cantilever. Cantilever response may be measured with sub-nanometre resolution which allows high imaging resolution [4]. Ideally, the point of measurement should be coincident with the tip-sample point of interaction [25], in order to obey basic measurement principles, such as the Abbé principle. The practical implementation of it is difficult and interaction forces are detected mostly by monitoring the close neighbourhood of the tip at the cantilever [4]. There are two common sensing techniques: optical and electrical. Optical methods utilize the so called 'beam bounce' or interferometry while the electrical methods use piezoresistive or piezoelectric effects.

2.5.2.1 Optical measurement techniques in AFM

The most common sensing technique is the optical lever method, also called the beam bounce technique. The beam bounce sensing system relies on focusing a laser beam on the end of an AFM cantilever. The light is reflected from the reflective face of the cantilever and focused onto a quadrant photodiode position sensitive device (PSD) [4]. As the cantilever deflection changes, the position of the deflected laser beam on the PSD also changes vertically. The two axis measurement is possible with this technique. The vertical PSD readout (up-down) is used for topography recording while the lateral (left-right) is used for recording of the torsion of the cantilever. On one hand it is advantageous feature which allows a two axis measurement, however it requires a very cautious alignment of the beam to eliminate the cross-talk between the axes [4]. Furthermore, provided there are no special measures taken, the beam bounce technique can be sensitive to the vertical movement of the whole detection system [4]. Special cantilevers must be used for this sort of readout, since not only the top face must be highly reflective, but also the cantilever width must be bigger than the incident laser spot [4]. A detailed study in the limiting factors of the beam bounce detection sensitivity is presented by Fukama *et. al.* [26]. The signal to noise ratio for the optical lever is limited by the laser spot size at the PSD, shot noise and diffraction. An alternative optical solution is the interferometric sensing. Laser interferometry provides good measurement of cantilever deflection and the vibration amplitude at high frequencies with minimal influence on the lever [27]. The

interferometric methods used in AFM are based on homodyne and heterodyne techniques [4]. They rely on the interferometry principle (e.g. [28]). In a very simplified description, the target (i.e. cantilever) position is sensed by the path difference of light travelling via stationary and moving (target) paths, which is detected by light intensity. The differential interferometer for AFM detection was developed by Sasaki *et. al.* [29] and Schoeneberger and Alvarado [30]. Yacoot and Koenders [6] write that these designs are difficult to implement and support alternatives by Oral *et. al.* [31] and Ruf *et. al.* [32] which use fibre interferometer. What is appealing there is the possibility of feeding the interferometer signal directly into feedback loop [6], making the feedback loop simpler and more stable. The beam bounce and optical interferometry have relative advantages and disadvantages. They are both fast and equally sensitive [33, 34]. Interferometers directly measure the normal displacement of the cantilever and with appropriate designs this movement can be separated from the vertical movement of the entire machine [6]. If the traceability is the concern, the interferometry technique is also advantageous. Two axis measurement of the beam bounce allows the friction measurements to be taken, but suffers from the cross-talk between two axes. Additionally, the noise levels in interferometers are lower than in beam bounce systems [6]. Despite the relative advantages of interferometry against 'beam bounce' it still remains a less attractive alternative in many instances as the optical arrangement is complicated and the cost are higher when compared to the 'beam bounce' method [4]. Both methods impose similar requirements on the cantilever, such as size and reflectivity, require precise and time consuming alignment [6], occupy significant space of the machine, and cause local heating of the cantilever due to the incident laser beam [6]. The local heating decreases the sensitivity and contributes to the noise level of the measurement [6]. These limitations have led to the developments of electrical measurement methods.

2.5.2.2 Electrical measurement techniques in AFM

Commonly used self sensing techniques in AFM include: capacitive, piezoelectric, piezoresistive sensing. The piezoresistive detection is utilized by connecting a cantilever as a resistor in a Whinstone bridge [35]. The cantilever bending is sensed by a change in cantilever resistance [35]. The technique is based on the well known strain gauge principle and inherits its major limits such as Johnson, $1/f$ noise, temperature sensitivity, and heat generation [4]. The sensitivity of the sensor can be expressed as the resistance change per unit cantilever deflection [35]. It has been reported that piezoresistive detection has a resolution, typically 10^{-4} nm/$\sqrt{\text{Hz}}$, which is 1 order of magnitude lower than the resolution of optical sensing techniques, typically 10^{-5} nm/$\sqrt{\text{Hz}}$ [4]. In most of the designs the resistor is formed close to the base of the cantilever and not at the tip. Power consumption of a piezo-resistor is in the range of milliWatts, which is considered to be a relatively large value [6]. Another detection method which transforms the cantilever bending into voltage signal is the piezoelectric effect based sensing. The sensing elements in the piezoelectric detection in AFM are the thin piezoelectric films, typically PZT or ZnO deposited on the cantilever [36]. The sensing mechanism is a piezoelectric film is sandwiched between two electrodes and attached to an AFM cantilever [12]. The

vibration of the cantilever is excited by a voltage applied between the electrodes and a current through the piezoelectric layer is measured. The change of the admittance is induced by the piezoelectric effect due to the bending deformation of a piezoelectric layer. Hence the change of the admittance indicates the change in cantilever dynamics. The amplitude resolutions of different designs in self sensing piezoelectric cantilevers span the range of 0.05 nm and 0.1 nm [36]. These films are typically used as a sensor and as the actuator that determines the amplitude and frequency of the cantilever oscillation [4, 36, 6]. This is a significant advantage of this sensing method, since the cantilevers with integrated piezoelectric actuators, in contrast to the external actuators in AFM, provide more accurate tuning and stable operation without spurious vibrational modes. Using the same inverse piezoelectric effect, one can also actuate the cantilever vertically by superposition of a DC voltage on a piezoelectric layer [37], however the travel range is smaller in comparison to a standard external vertical feedback stage. Rogers *et. al.* [36] developed a piezoelectric cantilever for lever excitation, deflection sensing and tip-sample spacing control, however with a limited vertical range of 1.5 μm. The vibration amplitude is sensed by measuring the change of current through the layer, similarly as described by Itoh and Suga [12]. The current is used in the feedback loop to produce a voltage which actuates the piezoelectric layer vertically, thus eliminating the need for a separate vertical scanner. The heat generation and thermal drift are relatively negligible in the case of the piezoelectric sensing in contrast to the piezoresistive sensing [4]. Additionally, the self actuation makes it a favourable choice against the piezoresistive sensing. Capacitive sensing is the last of self-sensing techniques used in AFM. Brugger *et. al.* [38] discusses an exemplary design, where two adjacent single crystal silicon beams form the electrodes for sensing, one carrying the AFM tip and being bended by the tip-surface interaction; the other being a base counter electrode. They are mounted to the vertical carrier and separated from each other by the layer of SiO_2 at the clamping. The capacitance change between these two is a measure for the probe-sample interaction. Literature indicates the capacitive sensing is reliable and accurate method for monitoring the cantilever deflections [38]. The capacitive sensing technique may provide measurements in two orthogonal directions [39], similar to beam bounce technique. Micro-capacitor sensing in AFM has been implemented [15], where the capacitive sensor acts like a resonator with phase control. Measuring corresponding shifts of the oscillation frequency of one of the electrodes is the sensing mechanism. This design is also self actuating, however, the vertical actuation signals are influencing the force sensing signals [37].

2.5.2.3 Self-actuated and self-sensing cantilevers

There are some designs reported, which incorporate the oscillation movement and sensing in one cantilever. Watanabe and Fuji [40] presented the piezoelectric actuator for cantilever oscillation together with piezoelectric read-out for the sensing. Moreover, there exist designs, (e.g. [41]) combining the piezo-resistive deflection sensing together with the piezoelectric actuation in the vertical direction. The piezoelectric cantilevers are favourable in terms of self-actuation possibilities. In contrast to the capacitive cantilevers there is no affection of the cantilever resonant frequency due to an AC excitation voltage. There is a group of cantilevers, which

have all three functionalities integrated, that is the oscillation, the detection, and the vertical positioning of the tip [11, 37]. The very important group of AFM self actuated and self sensing cantilevers are the tuning quartz forks described more in detail in the following passage. The tuning forks are based on quartz crystals. They operate in the same way as the tuning forks used in the quartz watches [4]. The tuning fork is oscillating due to the AC voltage applied to it with a predefined frequency, as it possesses the piezoelectric properties [4]. The sensing principle relies on monitoring the current flowing through the fork which in turn is proportional to the lever arm vibration amplitude and the changes in the damping [4]. The advantages of tuning fork cantilevers are its great internal stability [4], low internal energy dissipation, possibility of self actuation and self sensing, and a high quality factor Q [4]. The Q factor is a result of an oscillation mode in which both prongs of the fork oscillate out of phase to each other [9]. This favourable dynamic behaviour appears if the eigen frequencies of the two prongs are equal, and if they are not, the must be tuned fork appropriately [9]. Early tuning fork probes relied on attaching a tip to one of the prongs and oscillating the fork in the vertical plane. Alternative design is where the tuning fork is integrated (glued) with a separate micro fabricated cantilever carrying a tip [42]. The fork is oscillating in its 1^{st} flexural mode which induces a periodically changing mechanical stress in the cantilever legs. To accommodate this stress, the cantilever deforms such that its free end, where the tip is located, moves in plane perpendicular to the fork plane. Such an arrangement additionally tackles one of the tuning fork limitations, mainly it allows to adjust the natural frequency of the tuning fork and at the same time the cantilever stiffness to a desired value, which is rather difficult in the standard tuning fork designs as the prongs are usually quite stiff [42]. This design is called Akiyama probe or in abbreviation A-probe, after the name of its inventor. This probe has a Q range of 400-1000. Some articles discussing the early versions of A-probe quote the values of Q to be 2480 for the tuning fork and 35 for the cantilever [42], however the probe should be treated as a single coupled resonator with these values matched and hence there is a single Q value associated with it. The quartz tuning forks offer a stable, mechanically simple sensing mechanism with minimal external electronics.

2.5.3 AFM tips

The following passage discusses the AFM tip technology. AFM tip is a crucial element of the whole machine because it is directly interacting with the sample atoms. Typical important parameters are the geometry of the tip, material from which it is manufactured, and the current condition of the tip. In order to achieve high resolution, the tip should be as sharp as possible, ideally consisting of a single atom at the tip end, which interacts with sample atoms [9]. The sharp tip can follow rough surface or examine trenches in the structure surface, which is directly linked to the resolution of the AFM measurement [6]. The sharpness of the silicon tip can be as low as 1 nm tip radius [43], however the commercially available tips are available in the range of radius of 5-10 nm [6]. Giessibl [9] names even further requirement on the AFM tip, namely the appropriate coordination of the front atom. The front atom pointing in the [1 1 1] direction has better bonding configuration to the ‘neighbouring’ structure which implies

better stability of the tip [9]. Another aspect is the opening angle of the tip or aspect ratio. Firstly, one would wish to image with a small opening angle, since the whole body of the tip (not only the front atom) is interacting with the sample via long range forces [6]. By having a high aspect ratio tip, the interaction of the long range forces is reduced. Additionally, it is desirable to have a larger tip aspect ratio than the aspect ratio of a trench or groove enabling better measurement quality of the groove in terms of depth and width [6]. An opening angle of the tip influences the tip convolution [6] and the image it produces is directly depending on its opening angle. In a step response, the measured step has an inclination of less than 90° due to the tip convolution. The tips are typically made of Si_3N_4, Si, and recently, also from carbon nano tubes (CNT) [6]. The shape of the tip depends on the material used and the fabrication process [4]. Silicon tips are typically in the shape of irregular polyhedrals and Si_3N_4 tips are symmetric pyramids [4], which are typically sharper when compared to tips constructed out of Si. There are special techniques to sharpen the already manufactured tip, such as oxidation, ablation/depositing using focused ion beams (FIB) or by electron beam (e-beam) [4]. When wear of the tip is of concern, it is preferred to use a diamond-coated or a CNT tip [4, 6]. CNT are favourable because they define their own structure in the very repetitive way and aspect ratio of 10:1 is achievable [4]. Tips may also be mounted under an angle to the cantilever, such as in the case of A-probe, so one can observe the tip position at the sample while looking at the cantilever from the top via an optical microscope. The last important matter related to AFM is its condition, called also the tip characterization. This topic is reviewed comprehensively by Yacoot and Koenders [6].

2.6 AFM scanners

The following section discusses the AFM scanning system. The first section treats the possible arrangements of scanning motion. The second section describes and compares different scanner architectures.

2.6.1 Scanning methods

The cantilever in AFM is to be positioned relative to the sample in three dimensions in order to record the surface topography. There are several ways to realize the scanning of the tip relative to the sample. The cantilever can be held still and the sample is then positioned in three dimensions, referred to as the ‘scanning sample’. This technique is only feasible for small and lightweight samples, since the sample inertia is a limit in dynamic positioning [44]. Alternatively, the sample can be held stationary and the cantilever is scanned relative to the sample in three dimensions. This is referred to as ‘tip scanning’. Tip scanning offers the advantage of virtually unlimited sample size, however, it has drawbacks related to the complicated sensing, especially when optical readout is preferred [45]. In a third concept, the X-Y motion is handled by a stage that moves the sample while the Z motion is handled by an actuator moving the cantilever up and down [44]. Such an arrangement eliminates the coupling between vertical and horizontal movement, hence higher speeds and bandwidths are achievable for both

horizontal and vertical scanning. This configuration is especially promising for high accuracy topography tracking with large scanning ranges [44]. Contemporary designs use more often the independent motion between the planar scan and vertical scan. X-Y plane motion is either a tooth-saw triangular shape or rectangular shape trajectory. Triangular shape trajectory uses a triangle wave in the fast direction and a linear ramp in the slow direction [10]. The rectangular trajectory scan involves just straight lines in the fast directions, recorded from one side to the other, closely separated along the slow scanning axis. Some AFM experiments scan the sample twice, starting at first with the left to right motion, and repeated the scanning from right to left. The topography data can differ to some extend, but proper interpretation and comparison can yield useful topographical information. The scanning ranges for commercial X-Y actuators are between 0.4 μm and 400 μm [10].

2.6.2 Possible scanner designs

There are five different conceptual approaches of realizing an AFM scanner: 'piezoelectric tube scanner', 'tripod scanner', 'stacked scanner', 'resonating scanner' or rigid scanner. One of the earliest AFM scanners - the piezoelectric tube scanner is comprised of a tube with four electrodes on its outer diameter [44, 45]. The two electrodes opposite to each other are shifted in phase, so the applied voltage to those electrodes will stretch out one of them and shorten the other. This way, the tube bends, creating a raster scan movement of the free end of the tube. In addition, there is an inner electrode providing a uniform elongation of the tube in the z-direction. The advantages of this solution are reported to be its simplicity, large scan ranges between 10 and 100 μm, and small capacitances [45]. Piezoelectric tube scanners, however, possess a number of disadvantages. Both horizontal and vertical scans have low first mechanical resonances, correspondingly in the range of a few hundred hertz and of a few kilohertz [45]. Another disadvantage is the so called scanner bow phenomenon. The raster scanning motion generated by lateral bending of the tube causes inherently a change of the vertical position of the probe [44, 45]. This influences the AFM measurement and has to be removed from the AFM data by post processing [45]. The scanning bow phenomenon is discussed in detail by Rifai and Youcef-Toumi [46, 47] and by Tien *et. al.* [48]. Another solution, the tripod scanner, was also one of the very first designs in positioning SFM [3]. It comprises three orthogonally glued piezoelectric stacks [45]. This technique is not appealing due to the scanner bow presence, low scan range and low resonance frequency [45]. Another design, called the stacked scanner, eliminates the scanning bow problem. The stacked actuator consists of various scanning actuators, usually piezoelectric stacks, implemented on top of each other (e.g. [49, 44]), which allows eliminating the scanner bow. This is called serial implementation and it predefines the fast and slow axes of motion, which can be a disadvantage [45]. In short, stacked design offers absence of the 'scanner bow' and high resonance frequencies, however is typically quite complex system. A different concept for AFM scan is the resonant scan [50]. It employs a resonating tuning fork for fast X-Y scanning while the vertical scan is performed by the piezoelectric actuator [45]. Such an arrangement results in the inhomogeneous resolution of the image, which is caused by the sinusoidal scanning pattern [45]. Currently, it is

most common to use is the ‘rigid scanner’, based typically on a flexure mechanism driven by a piezoelectric actuator [4, 51, 52, 53, 54]. The scanning directions are arranged parallel which gives possibility for free choice of the fast scanning direction. The flexure based design suffers from much lower coupling between different translational directions in comparison to its alternatives [55]. Besides, the forces and displacements achievable with stacked piezoelectric actuators are higher than in the case of piezoelectric tubes [53]. The non-linear effects are more pronounced in the case of flexure piezoelectric stacks. Nevertheless, they are removed during closed loop operation [55]. The piezoelectric stacks offer an ultimately high resolution but somewhat limited range. This can be, however, solved by the mechanical amplification flexures, that is flexural levers, or by combination of the flexure with a coarse positioner [4].

Chapter 3

AFM scanner design

The following chapter is organized in the following manner. Section 3.1 discusses the requirements of the scanner, Section 3.2 outlines the general view on the designed scanner, Section 3.3 discusses the AFM probe used in the design, and Section 3.4 presents a more detailed description of subsequent components of the scanner and discusses aspects of their design.

3.1 System requirements

The goal of this research is to develop an AFM scanner for surface topography measurements. The requirements of the system are as follows: the scanner is to provide the ability to track and measure a maximum topography step of 10 μm with a measurement resolution of less than 0.1 nm and an uncertainty of less than 10 nm (1σ) at a controllable bandwidth of at least 2 kHz. The scanner should track the vertical topography of the sample. The tracked sample is positioned in the horizontal, X-Y, plane by means of a separate positioning stage. The primary function of the scanner is to follow the scanned sample topography along the path predefined by the horizontal positioning system. The vertical scanner must be compatible with a structural frame of the overall metrology system. This can be achieved by a kinematic mount system, allowing a fine, adjustable scanner position. The mounting and adjustment system is beyond the scope of the assignment. The final requirement of the scanner is the maximum volume it occupies, which is a cube with an edge length of 100 mm. This is for the integration in a complete metrology system, which requires that the scanner is compact and limited in size. The system specifications defining the required measurement range, resolution and uncertainty are straightforward to interpret. Nevertheless, the requirement of the minimum scanner bandwidth is somewhat less straightforward from the system specifications perspective. A bandwidth of 2 kHz means the scanner is able to follow an input signal, arising from the topography, with a frequency of 2 kHz. It also indicates the frequency at which the interaction force, F_{ts}, can be measured and controlled. In dynamic AFM, vertical scanner bandwidth partially determines the minimum detectable interaction force, F_{ts}, [14] and partially determines the maximum achievable scanning speed [49]. Nevertheless, the scanning speed is affected by the tip convolution and sample topography, which is primarily not known. Therefore, it is typically up to a microscope operator to determine the scan speed for a particular sample. Hence,

a bandwidth requirement is not determined by a measurement speed. Furthermore, the bandwidth is often represented as a measure of a bounded disturbance rejection. In case of an AFM scanner, a topography change can be seen as a disturbance entering the system. However, the sample topography is not known, yet deterministic, hence it is not possible to determine a bandwidth requirement based on the acceptable error caused by a disturbance. High bandwidth is, however, an overall trend in contemporary AFM scanners, since they achieve higher scanning speeds and thus higher thermal stability of the measurement. The bandwidth requirement is not determined from measurement specifications but is based on a reasonable target value for the system.

There are also other measurement technologies well established in the field of surface metrology: optical microscopy, white light interferometer (WLI), scanning transmission microscopy (STM), scanning electron microscopy (SEM) and stylus profilometry. They are a potential alternative to an AFM measurement system. There are advantages which AFM has in contrast to its counterparts and they are discussed in the remainder of this section. Similar to TEM, SEM, or stylus profilometry, AFM enables imaging at sub-nanometre resolution. The resolution of an optical microscope is limited by the light wavelength up to approximately 200 nm. Sub-nanometre vertical resolution is achievable with WLI, however the measurement range is lower than with AFM. Moreover, the horizontal resolution of WLI is typically in the range of 500 nm, which is much less than of AFM. Lastly, the optical imaging techniques do not provide distinction between a positive and negative topography change, which requires prior knowledge of the surface topography. TEM and SEM are limited to electrical conductive surfaces. AFM extends their capabilities to non-conductive materials, for example polymers. Additionally, AFM measurements are much simpler to perform than TEM or SEM measurements. AFM machines are also cheaper than their TEM and SEM counterparts and their price continuous to decrease, which makes them a wide spread scientific and industrial tool. Stylus profilometers, on the other hand, suffer from the probe and sample degradation, which is less pronounced than in AFM, since lower contact forces can be achieved. Requirements for the measurement setup, the ability to measure topography features of up to 10 μm in with a resolution of less than 0.1 nm limit the possible solutions. Moreover, the above discussion of the relative merits of AFM with respect its counterparts confirms the choice of AFM to be an adequate technological solution towards the final product specifications.

3.2 Scanner overview

3.2.1 Mode of operation

The purpose of the AFM scanner is to measure machined samples. From the discussion presented in section 2.3, the intermittent contact scanning mode was most suitable for this application. The contact AFM was not considered the right choice primarily due to extensive probe damage, lower imaging speed, stability issues, and more difficult realization of the sub-nanometre resolution. Conversely, NC operational mode has worse resolution than IC mode. In addition, there is no need for a non-contact imaging in the case of examining the machined

structures. As for wear, the condition of the AFM tip might be a subject of concern, however it can be limited by the proper adjustment of the tapping parameters.

3.2.2 Scanner design

The system specifications can lead to variety of possible solutions and consequently different designs. The scanner developed in this research is an integrated mechatronic system, comprising different components, interrelated to each other in their functionality. The design process of such a device yields a system oriented thinking rather than designing components independently. Hence, it is difficult and less descriptive to discuss the development process of such machine in a systematic way, describing the development of subsequent components separately. This is why the following section outlines the overall design and the main components of the scanner. Further sections treat these components independently. In this manner the main concept and certain dependences between subsystem components can be observed, which allows for more clear understanding of the design steps taken. The mechanical design of the scanner with its protective cover removed is depicted in Figure 3.1. Figure 3.2 describes the partial

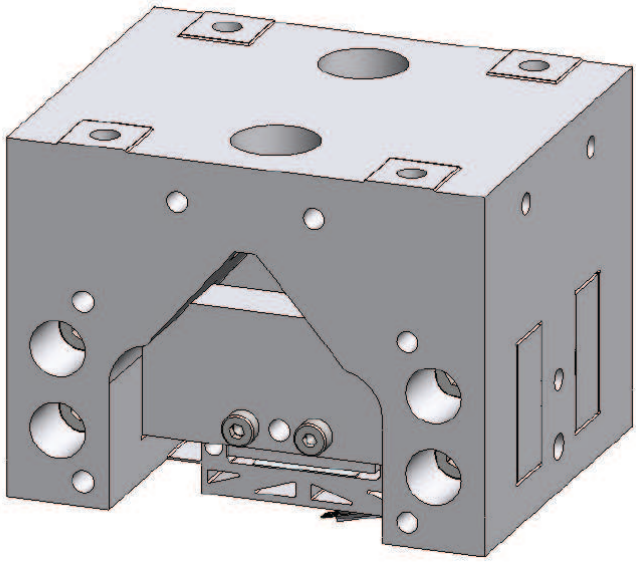

Figure 3.1: AFM scanner assembly with its protective cover removed.

assembly of the scanner without some front view components in order to show the scanner interior part. The scanner is comprised of a flexural positioning stage driven by a piezoelectric stack actuator in the vertical direction (z-axis). The position feedback of the stage is realized by an integrated capacitive metrology system. The capacitive sensor is mounted to the structural frame and is placed inside the flexural stage. The stage is positioning a self-sensing and self-actuating Akiyama probe [2]. The AFM probe taps the scanned specimen and provides a force, F_{ts}, feedback for the piezoelectric actuator controller. The topography measurement is performed by the AFM probe sensing an interaction force, F_{ts}, and the measured signal is sent

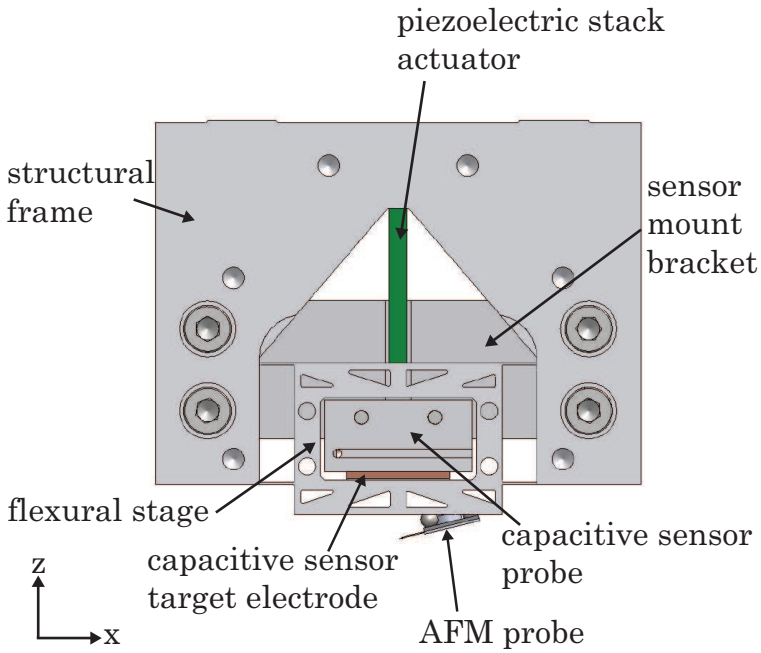

Figure 3.2: Partial assembly of the scanner.

to the feedback controller. The feedback controller generates an output signal correcting for the error between the setpoint value of, F_{ts}, and the current force signal in the loop. This signal is send to the piezoelectric actuator, which actuates the flexural stage, and hence the AFM probe, in order to achieve the set-point value,F_{ts}, by varying the probe vertical position, z. The stage displacement necessary to attain the set point is measured by the capacitive sensor and is a direct measure of scanned topography. The following sections of this chapter describe the development and design of main scanner components. The technical drawings of all designed mechanical parts of the scanner assembly are included in Appendix A.

3.3 AFM probe

A commercially available Akiyama probe (A-probe) was selected to measure the sample topography. The reasons the A-probe was selected were for its self sensing and self actuating capabilities and excellent achievable imaging performance. Having a probe that has a self actuating characteristics eliminates the need for an external shaker which reduces the inertia of the dynamically positioned mass and results in a compact sensor. Furthermore, the A-probe eliminates the need of an external optical measurement system by its inherent self sensing characteristic. By eliminating the optical measurement system commonly employed to measure the AFM tip behaviour, overall space savings can be achieved and no tedious adjustment and re-adjustment of the laser is required. This further enhances the probe's compact and simplistic design. Another advantage of the probe is an extremely stable oscillation of the tuning fork, due to the high stiffness it possess, providing a natural frequency of approximately 325

kHz [2]. Concurrently, Si cantilever has low stiffness providing suitable force sensitivity. The probe is pre-mounted on a ceramic plate with electrical connection pads which allows a direct mount to the stage and an easy probe replacement. The next section describes the principle of its operation. The following section discusses the design of a probe mount on the positioning stage.

3.3.1 Working principle of the Akiyama probe

The A-probe consists of the quartz tuning fork and micro machined silicon cantilever glued to the top face of the fork prongs , as shown in Figures 3.3(a) and 3.3(b). The quartz fork is

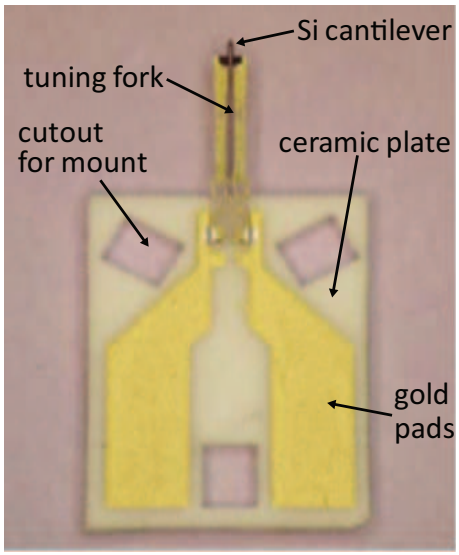

(a) Akiyama probe pre-mounted on a ceramic plate [2].

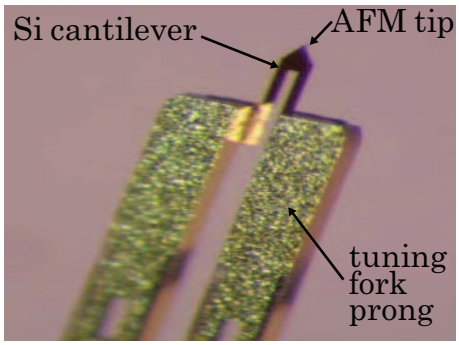

(b) Akiyama probe tuning fork [2].

Figure 3.3: Akiyama probe force sensor.

excited to resonate in its lowest eigenmode by means of a voltage signal applied directly to its electrodes. The resulting motion is the flexural vibration of the prongs in the horizontal, X-Y, plane a 180° phase difference between each prong. The micro machined cantilever connecting the prongs is asymmetrically glued onto the tuning fork. It is not lying in the horizontal plane intersecting the centre of inertia of the fork. Such an arrangement forces the twisting motion of the prongs while oscillating, due to the elastic reaction force arising from the cantilever.

The twist of the prongs is followed by the glued ends of the silicon cantilever and consequently yields a small amplitude vertical vibration of the cantilever end. This occurs due to the vertical, z, component of the cantilever end motion. The induced vibration results in a significantly amplified out of plane motion along the z-axis of the cantilever, where the tip is placed. The A-probe is an oscillatory force sensor, which can be seen as a coupled oscillator. Its dynamic characteristic, such as the resonance frequency, f_0, or the quality factor, Q, depend on the separate characteristics of the tuning fork and the cantilever. The probe is oscillated at its first resonance frequency and taps an examined surface. The interaction force, F_{ts}, changes the amplitude and resonance frequency of the probe, hence it can be detected by reading the piezoelectric output current of the tuning fork. During scanning the change of the natural frequency, Δf, is tracked by a phase lock loop (PLL) circuit and used as the feedback signal for the vertical positioning in order to keep the interaction force constant.

3.3.2 A-probe electronics

The following section treats the basics of the A-probe electronics and presents the development of the printed circuit boards used to operate the probe. The basic layout of the A-probe electronic functional blocks are shown in Figure 3.4 and present the overview of the A-probe circuitry. The A-probe voltage signal is pre-amplified, adjusted in phase and amplitude and

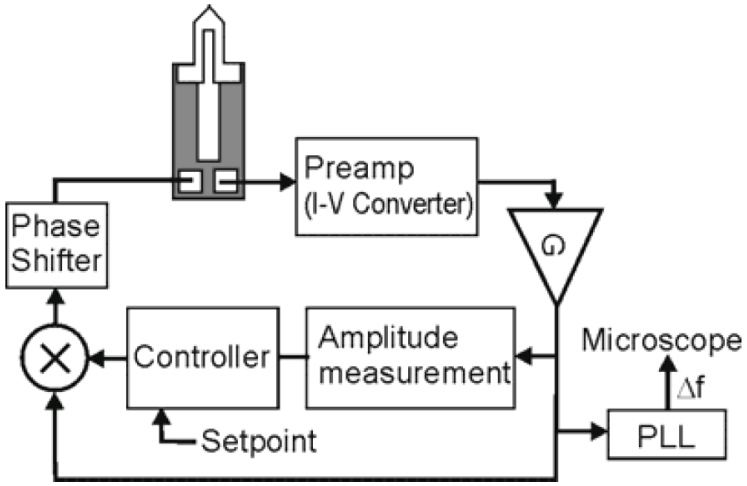

Figure 3.4: Akiyama probe electronics layout [2].

fed to the probe to achieve a desired probe oscillation. This is referred to as the self-oscillation block. Outside of this block there is a phase lock loop, which is detecting the change in the A-probe oscillation frequency, i.e. the change in the tip sample, F_{ts}, interaction force. This detected frequency change is directly fed to the AFM feedback system to vertically reposition the probe and reach the desired force setpoint, F_{ts}, under closed loop operation. The printed circuit boards for the A-probe operation were developed according to the exemplary electronic schematics from the manufacturer [2]. The electronics were divided into two boards, the pre-amplification board and the self oscillation board with a PLL readout circuit. Both printed

circuit boards were designed in Eagle 6.5 package. The following section explains these two circuits. First, the pre-amplification beard is discussed. Its electronic schematic and PCB board design are presented in in Figures 3.5 and 3.6. The pre-amplification board provides

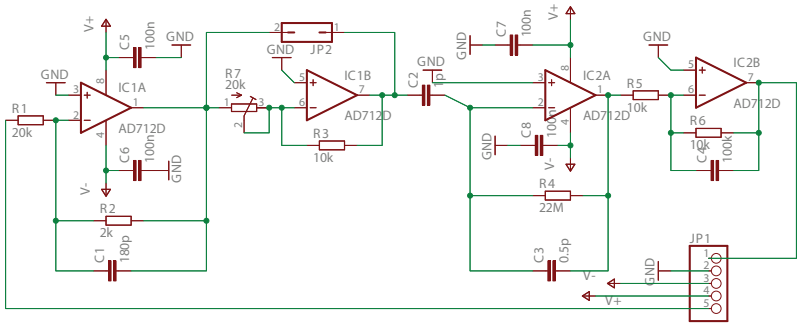

Figure 3.5: Pre-amplification board schematic.

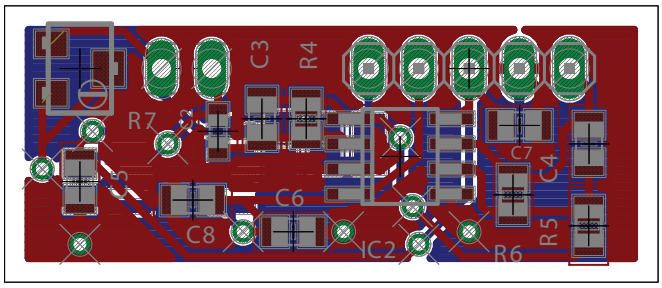

Figure 3.6: Pre-amplification board.

the input/output wiring, JP2, to the probe electrical contacts. The input voltage of 1 V_{p-p} to 3 V_{p-p} is attenuated by the inverting AD712 opamp, IC1A, of the gain equal to 1:10. The other inverting AD712 opamp, IC2A, with a 22 MOhm feedback resistor is acting as a current to voltage converter and transforms the piezoelectric current from the tuning fork into voltage which is further manipulated in the circuit. The third AD712 inverting opamp, IC1B, with the potentiometer at its inverting input and the 1 pF capacitor, C2, at its output is used to tune the voltage across C2 to compensate the parasitic voltage between the vibrating fork prongs, so only the piezoelectric current is read from the tuning fork. The last AD712 opamp placed on the board, IC2B, is a voltage follower with a gain of 1 with its output being the output of the pre-amplification circuit. The board possesses a 5 pin header connector to the central board for the input voltage, output voltage, ground, positive and negative supply voltage. The wires between the prong pads and the components C3, R4, IC2A and C2 are kept as short as possible to reduce the parasitic effects [2]. Moreover, a large ground plane is created at both sides of the board, which additionally guards the connection between these components and effectively reduces the noise. It is recommended by the probe supplier, to keep the wires between the pre-amplification board are as short as possible. To accommodate this, the pre-amplification board

was designed to fit into the stage, parallel to the metrology brackets, see Figure3.7, and hence limit the cable length and related parasitic effects. The board dimensions were determined by the clearance available for it inside of the stage assembly, 14 mm x 30 mm, see Figure 3.6. The second board developed, the 'self oscillation and PLL board', covers the remaining modules

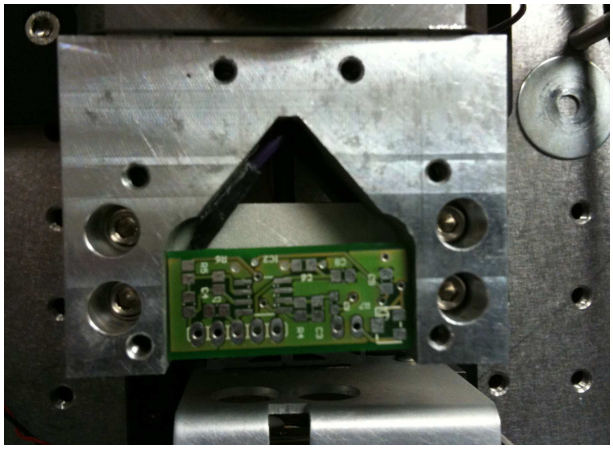

Figure 3.7: Pre-amplification board inserted into the stage structural frame.

presented in Figure 3.4. Its design is shown in Figures 3.8 and 3.9. First, the self oscillation circuit is discussed. It covers the amplitude measurement block, phase shifting block, amplitude adjustment and amplitude control block. The function of these blocks is to fine tune the amplitude and phase of the A-probe oscillation, to match its piezoelectric and mechanical characteristic for the best measurement sensitivity. The pre-amplified piezoelectric voltage signal from the pre-amplification board enters the self oscillation circuit and is amplified by 8.1 in the inverting OP467 amplifier, IC1A. The IC1A output is fed to both the multiplier AD633 and the amplitude measurement circuit. The latter is formed by a full wave rectifier and low pass filter. The full wave rectifier is created by the OP467 opamp, IC1C, and two rectifying diodes D1 and D2. The rectifier output is further low pass filtered by the active low pass filter formed by the OP467 opamp. IC1D, the feedback resistor R10 and the feedback capacitor C11. The IC1D output gives essentially the DC amplitude signal. Further on, this signal enters the proportional integral (PI) controller, with the adjustable feedback gain resistor, R1, and the amplitude adjustment potentiometer, R9. The adjusted and tuned amplitude DC signal is further multiplied by the initial AC signal by the AD633 multiplier. The multiplier output is the AC voltage of a tuned and adjusted amplitude. This signal enters the phase shifter in the next stage. The phase shifter is created by a high pass filter, formed by the potentiometer, R13, in an RC configuration with the capacitor C3, and an active, 'fixed' low pass filter formed by the IC13A feedback branch C24 and R14. In this manner both the phase and amplitude of the voltage signal are adjusted, as shown in Figure 3.4. The other working block of the board, the phase locked loop, PLL, works outside of the 'self-oscillation' circuit, hence it does not affect the probe oscillation. The output of the IC1A opamp is fed to the precision comparator, AD790. The precision comparator has the LATCH pin connected to the V_{LOGIC} pin, hence the latch is disabled and it works as a simple comparator of voltage inputs V+ and V- with negative logic. The positive input of AD790 is connected to the ground, hence the comparator acts as a square

wave generator. When the input V- is negative, the comparator output is 1, and when it becomes positive, the comparator output is 0. The output of the comparator enters the single chip phase lock loop, XR2212, as a square wave, which is manipulated easier than the sinusoidal signal by the phase detection circuitry. The PLL loop chip reference signal, the frequency of the internal voltage oscillator, can be adjusted by the R27 timing resistor, connected to the TIM-R pin number 12 of the PLL chip. The frequency of the variable crystal oscillator, VCO is

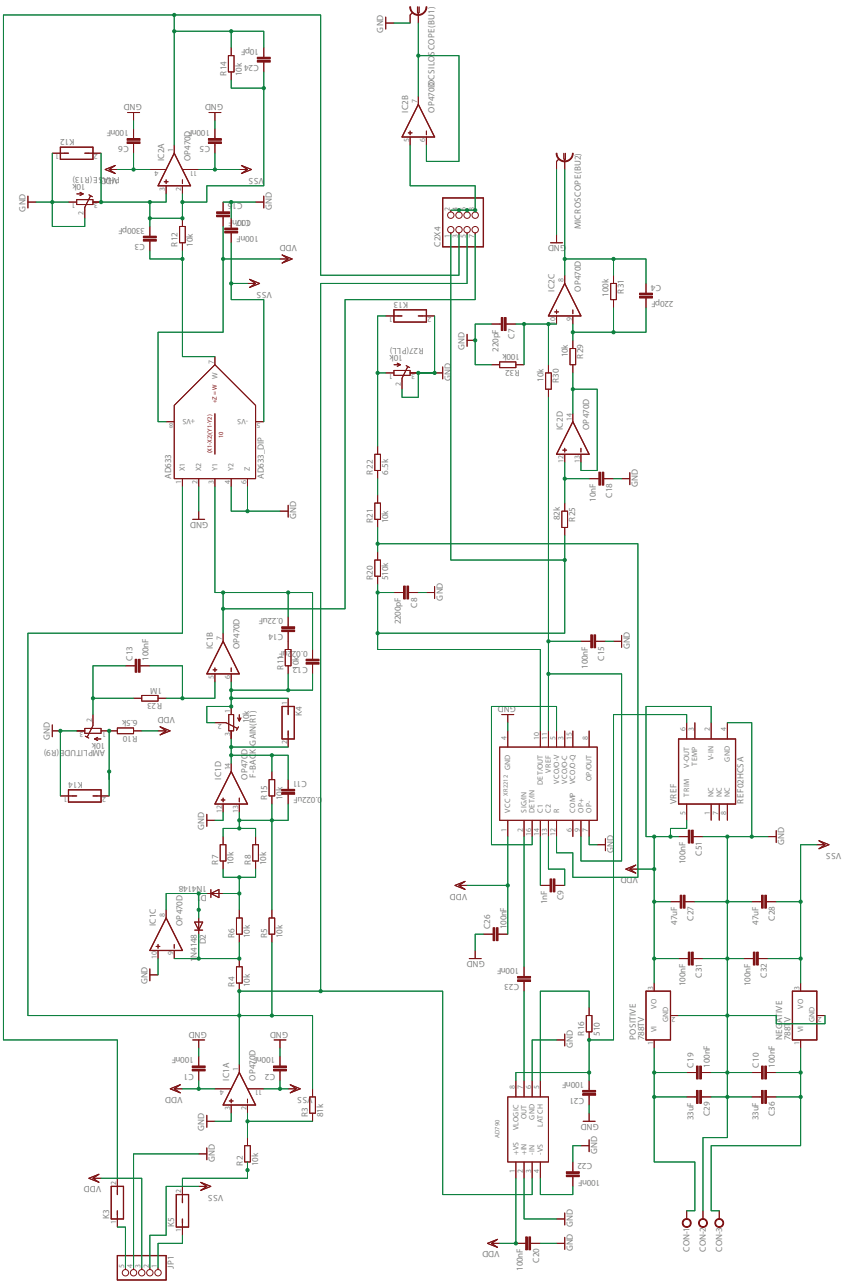

Figure 3.8: Self-oscillation and PLL board schematic.

linearly depending of the R27 setting. Thus the VCO frequency of the PLL chip can be closely matched with the frequency of the probe self-oscillation. The VCO voltage source output, pin 5, is fed back to the phase detector input, 0-det I, at pin 16 of XR2122. The other input of the phase detector is the square wave signal coming from the comparator, AD790, output, which

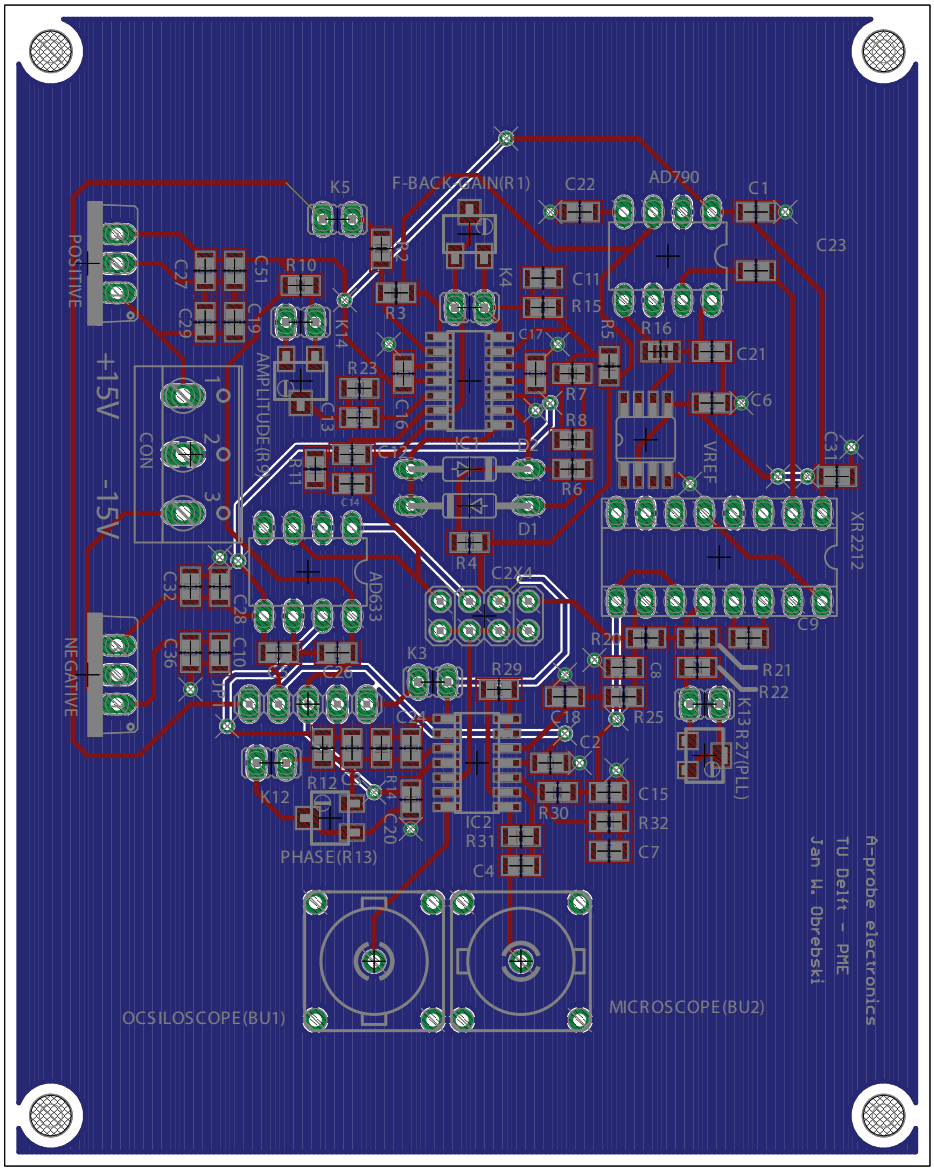

Figure 3.9: Self-oscillation and PLL board.

is internally amplified in the PLL chip just before entering the phase detector. The phase detector gives the output, DET/OUT, which is a frequency difference between its two inputs, with the output swing, DET/OUT, being expressed relative to the internal voltage reference value, V_{REF} at pin 11 of XR2122. The V_{REF} and DET/OUT are subtracted from each other by the OP467 opamp, IC13C, so their difference is the negative or positive change of the A-probe frequency, which is a direct output to the microscope.

3.3.3 Probe mount

The A-probe is pre-mounted onto a ceramic plate, as indicated in Figure 3.3(a). The ceramic pad has three rectangular cut-outs. Theses cut-outs are theoretically exact dimensions and the centre lines of the longer edges of the cuts are placed under 120° with respect to each other. These features allow the A-probe plate to be mounted to a structure by a kinematic mount using six point contacts. The probe mounting is realized in this development by utilizing three stainless steel spheres. The spheres rest on the sharp edges of the circular cut-outs made in the bottom face of the stage, see Figure 3.10. Spheres are held by glue layers filling the holes. In theory, the kinematic mount between three spheres and three cut-outs in the ceramic plate is formed by a six point contact, which constraints six degrees of freedom of the plate. These points are the midpoints of the longer edges of the probe plate rectangular cut-outs. In practice, the contacts between the ceramic plate and steel spheres are made by very small contact areas and depend on the stiffness of both components and the preload force applied to hold the plate against the spheres. However, a six point contact is a valid approximation for discussion of the mount. Such a mount provides a deterministic, repeatable positioning of the probe relatively to the stage. This is favourable if the probe must be exchanged due to tip degradation. Potential drawbacks of a kinematic mount are a low stiffness it provides and a low load capability of the mount. These are, however, not subject of concern, since the forces exerted on the mount, mostly the inertia force of the probe and its preload system, are low. Figure 3.10 depicts all components forming the mount. The ceramic plate makes contact with positioning spheres

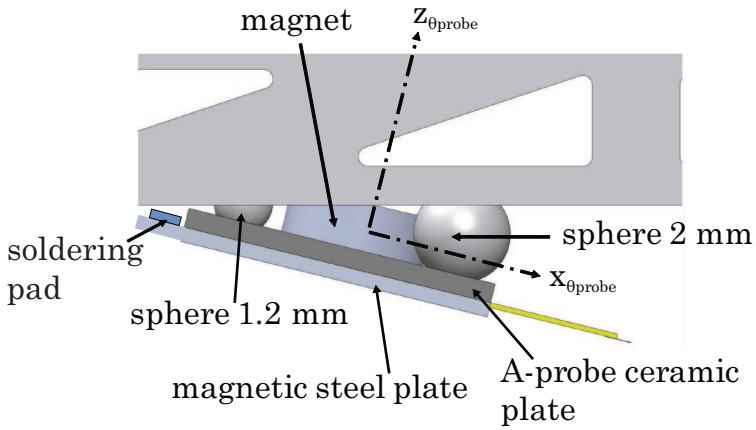

Figure 3.10: AFM probe mounting to the positioning stage.

from one side and is preloaded by a magnetic stainless steel (SS431) plate. The drawing of the steel plate is included in Appendix A in draft number P90427b-100-00010d. The steel plate has a UV glue layer substrate deposited on one face to form an electrical insulator. To form the individual electrical contact between the plate and ceramic plate of the A-probe, two silver pads were painted onto the glue. The silver pads connect to two solder pads, which are soldered to an electrical cable. This way, an electrical cable does not need to be soldered to the probe, which makes the probe exchange faster and easier. The desired preload force exerted by

the stainless steel plate onto the A-probe is achieved by a permanent magnet, which is glued to the positioning stage. The magnetically preloaded kinematic mount is shown in Figure 3.11. As indicated in Figure 3.10, the AFM probe is mounted to the stage under an angle

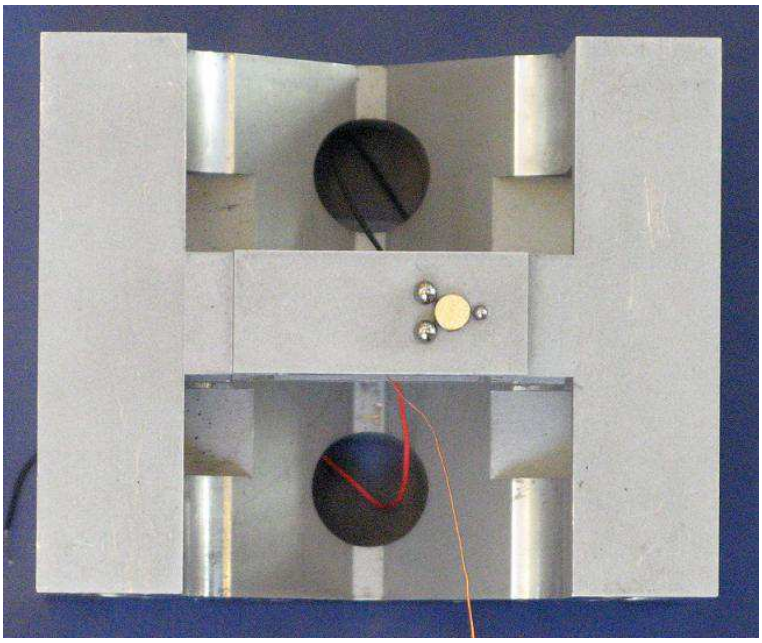

Figure 3.11: Probe mount spheres and a preloading magnet.

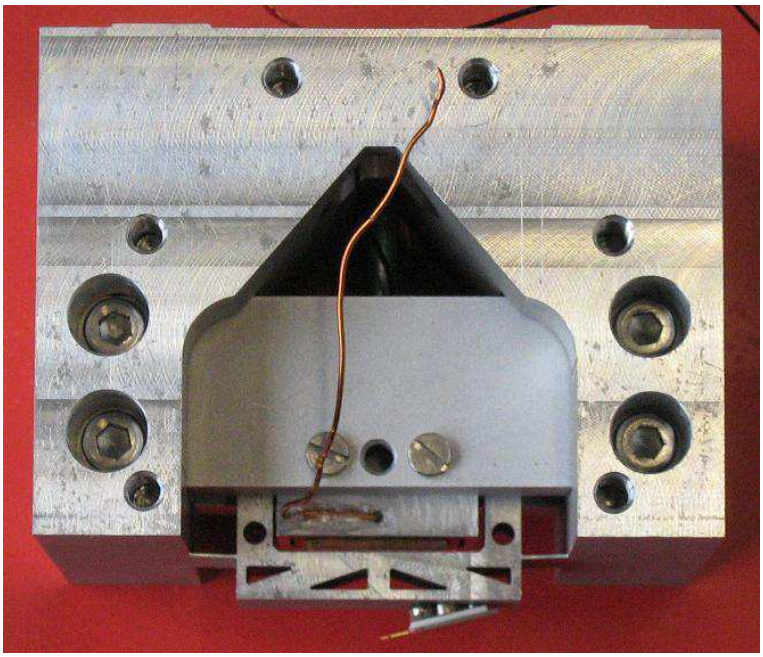

Figure 3.12: Mounted probe with a preloading magnetic plate.

θ_{probe} equal to 13°. There are two reasons for mounting the probe under this angle. First, the angle was chosen to avoid collision between the A-probe stainless steel preload plate and sample surface during measurements. Secondly, the A-probe tip is creating an angle with the

probe cantilever and hence in order to optimally tap the sample it is recommended by the probe supplier to place the probe under an angle within 10° to 15° relatively to the sample plane. The alignment angle of 13° was achieved by placing the probe on two spheres of 2 mm diameter and one sphere of 1.2 mm diameter. The spheres are graded 100 and 48 respectively which corresponds to the symmetric tolerances on the diameter of 12.7 μm and 2.54 μm, respectively [56]. These tolerances and the manufacturing tolerances on the position and diameter of cut-outs in the stage for the sphere placement, see Appendix A, introduce the achievable angle range of $13° \pm 2°$. The magnet is placed within the triangle formed by centres of the three circular cut-outs in the stage to assure appropriate preloading. The magnet is in turn is glued to the stage at a 13° angle to enhance the magnetic induction field it creates at the steel plate face. The magnetic pulling force exerted by the magnet must be sufficient to hold the mounted mass, the mass of the probe and the steel plate, under the static condition, to overcome the gravity forces. More importantly, the magnetic pulling force should hold these masses under the dynamic conditions, to overcome the dynamic inertia forces due to the acceleration of the stage. The required pulling force is calculated for the static and dynamic critical situation in which the stage is oscillating with an amplitude of A_m = 5 μm at a frequency of f_b = 2 kHz. The pulled mass, m_{pull} is equal to 0.12 g. The force exerted on the mass due to the gravity acceleration and the acceleration of the stage is expressed as

$$F_{mount} = m_{pull}\left[g + A_m(2\pi f_b)^2\right]. \tag{3.1}$$

The approximated value of F_{mount} is equal to 0.096 N. The magnet used in the mount is a NdFeB magnetic disc of radius R_m equal to 3 mm, length l_m of 1 mm and residual flux density, B_r, between 11700-12100 Gauss [57]. The pulling force exerted by the magnet on the steel plate, which is placed at the distance d_m equal to 0.55 mm from the magnet face, is calculated as follows. The magnetic induction at the point placed at the axis of the magnetic disc at the distance from the magnet is approximated by [58]

$$B = 0.5B_r\left[\frac{(l_m + d_m)}{\left[R_m^2 + (l_m + d_m)^2\right]^{0.5}} - \frac{d_m}{\left(R_m^2 + l_m^2\right)^{0.5}}\right], \tag{3.2}$$

where B_r is the lowest residual flux density specified for the magnet (B_r = 11700 Gauss). The induction B at this point is calculated to be 2.29 Gauss and is related to the pulling force, F_{magn}, which is exerted on the steel plate, expressed by [58]

$$F_{magn} = 0.577B^2\pi(0.03937R)^2, \tag{3.3}$$

where B is the magnetic induction in kilogauss and F_{magn} is in pounds. The F_{magn} recalculated into SI force units is equal to 0.148 N. The pulling force was additionally calculated via an on-line magnetic pulling force calculator [59]. The returned value is equal to 0.18 N. The static and dynamic equilibrium of the mount is considered in the $x_{\theta(probe)} - z_{\theta(probe)}$ coordinate system, which is the $x-z$ coordinate system rotated by an angle θ_{probe} clockwise, see Figure 3.10. There is a reaction force arising from the two grooves of the plate along negative $x_{\theta(probe)}$ forming an equilibrium with F_{magn} and F_{mount}. The mount would work if the magnetic pull force, F_{magn} is greater than the F_{mount} component along the $z_{\theta(probe)}$ direction, where

$$F_{pull} > F_{mount}cos\left(\theta_{probe}\right), \tag{3.4}$$

Equation (3.4) is theoretically satisfied with a safety margin of 36%. In case the magnetic force approximation was not valid within the safety factor taken, safety precausions are to attach additional, 1 mm diameter, magnets to the stage which would enhance the magnetic induction enetering the steel plate and hence increase the magnetic pull force.

3.4 Flexural stage design

3.4.1 Overview

The flexural stage is a key element of the developed AFM scanner. The monolithic structure is shown in Figure 3.13. One can distinguish the movable stage part, contained in the red box in Figure 3.13, and a stationary structural frame, contained in the green box in Figure 3.13. The movable stage consists of a rectangular frame guided by four parallel leaf springs and is monolithically integrated into the structural frame. The monolithic design was chosen to achieve a stress free and strain free instrument. Furthermore, monolithic machining allows much more precise alignment of the stage components than manual assembly. Additionally, a potential interface wear of assembled components is eliminated by the monolithic design. The monolithic structure was manufactured by a combination of wire electro discharge machining (wire EDM) and milling processes. A detailed view of the part is presented in Appendix A in the draft titled P90427b-100-0001c. The mechanical structure of the stage has several functions. Its main purpose is to hold the AFM probe and guide it along the z-direction ensuring a constant interaction force between the tip and sample surface. The AFM probe is mounted to the bottom face of the stage, designated as face 'd' in Figure 3.13. Moreover, the flexural elements are to provide the necessary preload for a piezoelectric stack actuator. In addition, the stage has an integrated metrology system for position feedback which will be discussed in detail in a subsequent section of this chapter. As indicated in Figure 3.2, there is a counter electrode of the capacitive sensor attached to face 'c' of the stage moving frame. The movable stage position measurement is performed by sensing of the gap between the counter electrode and a stationary capacitive probe mounted to the structural frame. Hence, the structural frame of the stage provides the base for the metrology frame attachment and adjustment. The structural frame possesses a mounting interface to an overall microscope frame via four M4 bolted connections in the top face of the structural frame. The operational bandwidth specification of the scanner requires that the positioning stage has a sufficiently high resonance frequency. It is desirable to design a system having the first resonant mode of the structure, which is controllable and observable, at frequency of at least 6 kHz to control the system at frequencies below the resonance peak. It is also possible to integrate sophisticated control schemes to allow closing the loop at even higher bandwidth, however of 6 kHz was chosen as the target resonance frequency in order to make a simple control solution feasible. The positioning stage is based on a flexural guidance mechanisms. There are certain advantages of this approach [5]. Flexural mechanisms are practically wear free if not overactuated. Thus their performance is unaffected by external factors through their life. A potential distortion of the flexures is only possible via corrosion or fretting. The motion of the flexures is repeatable, continuous and smooth. More-

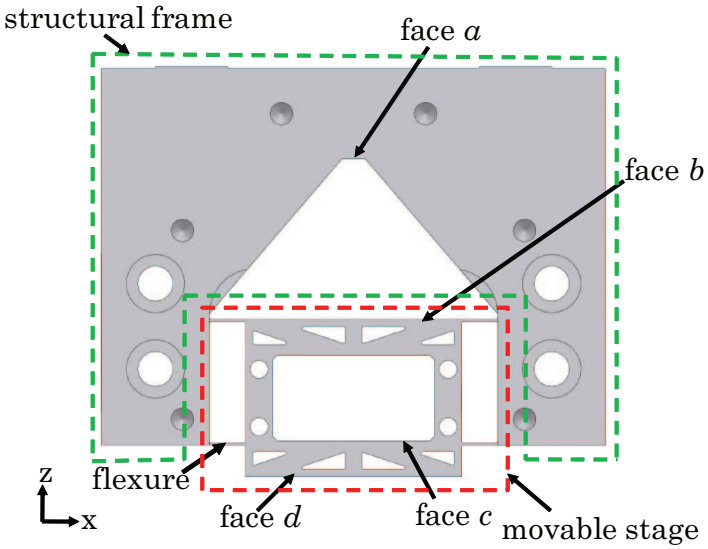

Figure 3.13: Flexural stage - front view.

over, it can be precisely determined and predicted from the known actuation forces applied to the flexures. Conversely, a precise force can be exerted by controlling the flexure displacement. Nevertheless, these assumptions are valid for the operation of flexures in their elastic region. There are also potential disadvantages of using flexures [5]. Flexures have somewhat limited load capacity and restricted displacements. The hysteresis effect, caused by the dislocation movement, is present in most materials. Flexures suffer from a relative low stiffness against undesirable out of plane motion, which may induce unintended off-axis motion.

3.4.2 Design concept

The actuation of the stage is realized by a piezoelectric actuator, inserted in between faces 'a' and 'b', see Figure 3.13. A voltage controlled strain of the actuator exerts a force on the face 'b' and is further transformed to the leaf springs, which become elastically deformed and guide the movable frame mass. The actuation forces along the z-direction are transferred into the stage displacement via the leaf springs while forces in all other directions are nominally blocked and decoupled via corresponding low compliance mechanisms. This topic is covered in detail in Section 3.4.3. The moving frame is in series with the flexural springs and hence is also subjected to an elastic deformation prior to actuator force. This deformation, in particular the deformation of faces 'c and 'd' introduces an error in AFM measurement, since these faces are coupled to the metrology system. Deformation of the face 'c' directly affects the position of the AFM probe, consequently generating a signal from an elastic deformation of the stage due to actuation force. The deformation of face 'd' is transformed to the deformation of the counter electrode of the capacitive sensor, which introduces an erroneous position feedback of the stage. Both of these errors contribute to an overall measurement uncertainty and should be kept as small as possible. The actuation force is simultaneously exerted on face 'a', and transformed further into the structural frame of the stage. The deformation of the structural frame is less pronounced than the frame deflection, however it is important to see it as a potential measure-

ment error contribution. The deformation of the stage movable frame is depending on its own stiffness, the ratio of this stiffness to the flexures stiffness and the actuation force value. To reduce the frame deformation, the flexures are designed to be very compliant. This approach has a numerous benefits. First, the stage travel is accomplished with a lower actuation force. Second, the stage frame becomes stiffer relative to its guidance. Finally, the local deformation of the stage frame caused by elastic bending moments transformed to it from flexures is minimized. With a compliant guidance design, a limited deformation of the stage components can be achieved. Another important design objective is a high resonance frequency of the stage. To meet both design objectives, high resonance frequency and low stiffness leaf springs, a stage with a low mass must be designed. The stiffness necessary to accomplish a high resonant frequency is obtained by using a high stiffness piezoelectric actuator. The total stage stiffness becomes a sum of the flexure stiffness and the actuator axial stiffness if an actuator is preloaded by flexures at all instances. This condition is valid if the sum of the maximum inertia force of the stage and the gravity force of the stage are lower than the preload force

$$F_{preload} > m_s \left((2\pi f_b)^2 A_{\delta zmax} + g \right), \tag{3.5}$$

where g is the gravitational acceleration, m_s is the overall dynamic mass of the stage, f_b is the bandwidth, $A_{\delta zmax}$ is the maximum amplitude of stage oscillation, and $F_{preload}$ is the preload exerted on the actuator. A high stiffness was the most important parameter while choosing an actuator. The actuator is described in Section 3.4.6. The is a rectangular block with a rectangular cut-out along the y-direction in the centre. The frame is formed by four beams, as indicated in Figure 3.14(b), two vertical beams AD and BC, and two horizontal beams AB and CD. The cut-out is created for capacitive sensor placement and is determined by the sensor dimensions. Such an architecture allows the position feedback measurement along the axis of stage actuation. In addition, the AFM probe tip is placed on this axis. In this manner, the Abbé principle is theoretically obeyed, which is important from the metrology and feedback control perspective. There are some additional benefits for a movable frame arrangement. The frame height along the z-direction allows for sufficient spacing between leaf springs, which yields a high rotational stiffness $K_{\theta_y M_y}$, as discussed in Section 3.4.3. The stage height accommodates for the flexures' vertical separation and a necessary offset between the bottom flexures and the stage face 'd', which is providing a necessary clearance for the stage cover, described in Section 3.4.10. Further, the frame enables a significant mechanical decoupling of the stress and the resulting deformation introduced by the actuator in the horizontal beam, AB, from the horizontal beam, CD. A simplified sketch of the movable stage frame elastic deformation is depicted in Figure 3.14(a). The importance of limited elastic deformation of the beam CD was outlined in the former Section. Moreover, the elastic deformation of beam AB requires an additional actuator stroke, to achieve the necessary stage displacement. In general, the frame ABCD must be stiff to limit the elastic deformation of beams CD and AB. Moreover, the high frame stiffness is important for obtaining a high second natural frequency of the stage, in which the frame is rocking and beams AB, BC, CD and AD are resonating in their flexural modes. This topic is discussed in Section 3.4.9. Alternatively, the movable frame mass should be low, to achieve high resonance frequencies of the stage. The movable stage frame

was optimized for low mass and high stiffness. The mass of beams AB and CD is reduced by triangular cut-outs, as indicated in Figure 3.14(b). The stiffness of these beams is provided by the links AF, BF, DG and GC, marked in red in Figure 3.14(b). These links connect the corners of the beams to their centre points. These links provide effectively most of the beam bending stiffness. The material not effectively contributing to the beam stiffness is removed by triangular cut-outs. The effective stiffness material is symmetrically distributed along the links AF, BF, DG and GC. Furthermore, links EF and GH are designed to transform the forces and the resulting stress in the beams and additionally stiffen the horizontal beam members. Another reason for introducing the triangular cut-outs into beam CD was an optimization for its desired deformation shape. The non-uniform material distribution along the beam length in the x-direction induces a higher order bending of the beam, involving the local folding of the material, which in turn, effectively reduces the net deformation of the beam. Beam deformation shaping generates effectively less elastic deformation than in the case of a uniform beam element. This topic is treated in detail in Section 3.4.5. The mass of the vertical beams AD and BC is reduced by circular cut-outs, as shown in Figure 3.14(b). The circular holes provide also a uniform stress distribution and stress flow, which is important for high stiffness of the beam and consequently of the whole frame ABCD. Chamfers in the inner part of the movable frame are designed to additionally stiffen the frame structure. Another mass reducing cut-out is the through hole along the x-direction, shown in Figure 3.15, which is a 3 mm sliding fit hole. A pin is inserted and used as a stiffening and securing connection between the movable and structural part of the stage while manufacturing and handling. The optimization for low mass and high stiffness of the frame was performed with ANSYS software. The cut-outs in the movable frame reduce the mass of the stage by over 21%. The elastic deformation of the stage is discussed in detail in Section 3.4.5. The stage is manufactured from Aluminium 7075-T6 due to the low density of this material. Further benefit of using 7075-T6 alloy is its ultimately high yield stress limit, which is important for the leaf spring design. Another advantage of this alloy are its favourable manufacturability properties and stress relieved treatment to reduce warping. The monolithic structure is symmetric with respect to the X-plane and Y-plane.

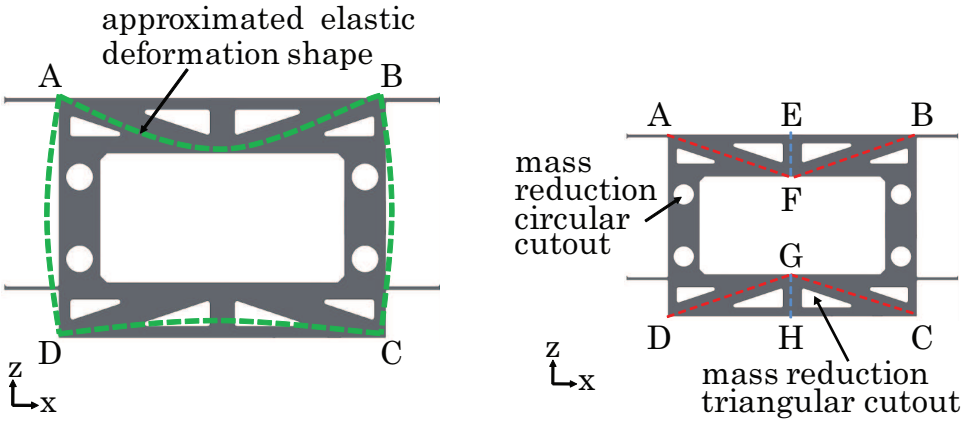

(a) Simplified shape of stage elastic deformation.

(b) Mass reduction and deflection shaping cut-outs.

Figure 3.14: Movable stage frame.

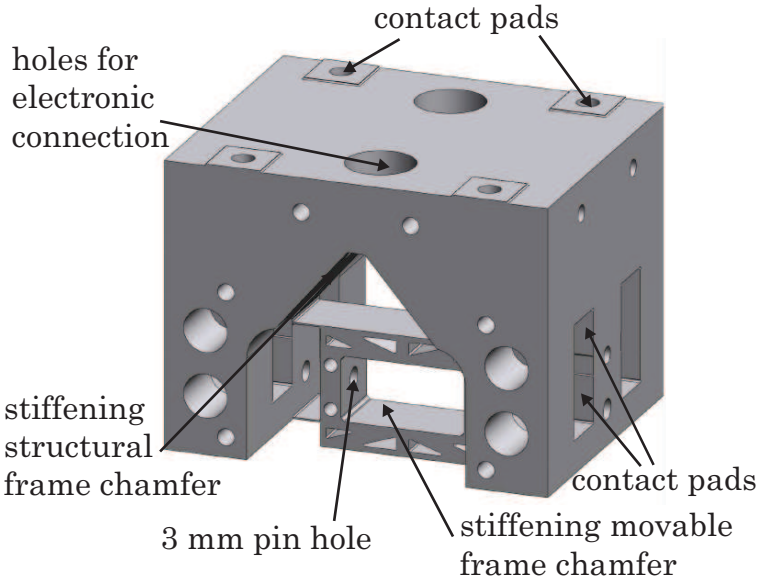

Figure 3.15: Flexural stage - isometric view.

Symmetry in these planes diminishes the stage deformation due to the thermal expansion. As indicated in Figure 3.15, there are contact pads designed for the stage mount to an overall frame and contact pads for capacitive sensor mounting bracket assembly. The contact pads define the contact area between the contact surfaces. There are two holes in the top face of the stage meant for electrical cable connections of the electronic components, including the piezoelectric actuator, capacitive sensor, and AFM probe. A static analysis of the system was performed, both analytically and with finite element software, to determine the movable stage frame stiffness, computation of flexures stiffness, and stress analysis for an optimal design.

3.4.3 Flexures stiffness

Leaf springs are thin, slender beams typically used as motion guides. Using the coordinates of Figure 3.14(b) the designated dimensions are L_f along the x-axis, H_f, along the z-axis, and W_f along y-axis. The nominal dimensions of leaf springs guiding the stage are: H_f is 0.22 mm, W_f is 10 mm and L_f is 4 mm. Leaf springs used in this design are manufactured with fillets at their ends, see Appendix A, with a radius specified between 0.1 mm and 0.2 mm to reduce stress concentration. Fillets effectively shorten the beams, which stiffens the flexures. The following analytical discussion neglects the presence of fillets for simplicity. Detailed structural study of the leaf springs with fillets is carried out with finite element simulation. The four leaf springs configuration, as shown in Figure 3.13, yields a parallelogram flexural stage guidance along the z-direction. The flexures deflect in an 's-shape' when the stage is parallel translating along the z-direction. While guiding, a leaf spring has a zero slope at its ends defined by $\frac{dz}{dx}_{(x=0)} = 0$ and $\frac{dz}{dx}_{(x=L_f)} = 0$. The part connected to the structural frame has zero displacement $z_{(x=0)} = 0$. Basic elasticity theory yields the bending equation describing leaf spring

deformation as

$$M_b = EI_y \frac{d^2z}{dx^2}, \tag{3.6}$$

where M_b is the bending moment due to the force F_z, E is the modulus of elasticity and I_y is the moment of inertia about the y-axis of the beam. Applying the boundary conditions for an 's-shape' deflection, the expression for the stiffness, $k_{F_z\delta z}$, of a single leaf spring in the z-direction due to the force F_z is [60]:

$$k_{F_z\delta z} = \frac{12EI_y}{L_f^3}, \tag{3.7}$$

where

$$I_y = \frac{W_f H_f^3}{12}. \tag{3.8}$$

Since the four leaf springs are working mechanically in parallel, the total stage stiffness is a sum of individual leaf spring stiffnesses

$$K_{F_z\delta z} = \frac{412EI_y}{L_f^3} = \frac{4EW_f H_f^3}{L_f^3}. \tag{3.9}$$

Using Equation (3.9), the value of $K_{F_z\delta z}$ was calculated and is equal to 0.477 N/μm. The stiffness $K_{F_z\delta z}$ was additionally calculated with FEM analysis, resulting in 0.508 N/μm. Figure 3.16 depicts a simulated travel of 10 μm due to actuation force of 5.08 N. The difference in

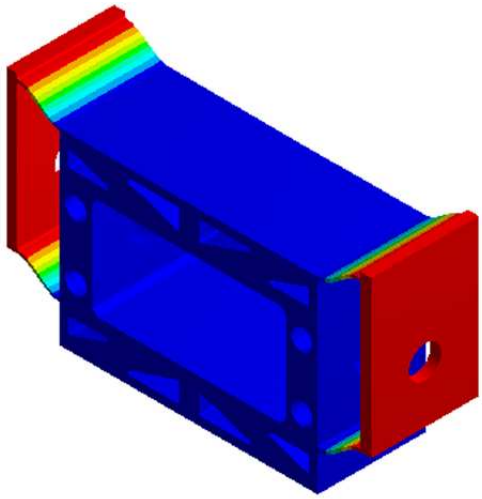

Figure 3.16: Flexures displacement of 10 μm due to 5.08 N force (red = 0 μm, blue = -10.3 μm).

analytical and FEM result is visible due to the flexure fillets were included in the FEM model whereas they were not covered by the analytical approximation. The manufacturing tolerances of the flexures, see Appendix A, span the possible $K_{F_z\delta z(FEM)}$ range from 0.424 N/μm to 0.61 N/μm. Similar to Equation (3.9), the stage stiffness, $K_{F_y\delta y}$, in the y-direction due to the force F_y applied to it is approximated by [60]

$$K_{F_y\delta y} = \frac{412EI_z}{L_f^3} = \frac{4EW_f^3 H_f}{L_f^3}. \tag{3.10}$$

The calculated value of $K_{F_y\delta y}$ is equal to 986 N/μm and is considerably higher than $K_{F_z\delta z}$, since W_f is significantly higher than H_f and, consequently, I_z is much larger than I_y. The stiffness of a leaf spring in its longitudinal, x-direction is also considerably higher than in the z- direction. This is expressed by

$$k_{F_x\delta x} = \frac{W_f H_f E}{L_f}. \tag{3.11}$$

The resulting stage stiffness, $K_{F_x\delta x}$, is approximated by

$$K_{F_x\delta x} = \frac{4W_f H_f E}{L_f}, \tag{3.12}$$

and equals 150 N/μm. The flexure axial stiffness is important for the rotation of the stage about the y-axis due to a moment M_y. In this case, the flexures work in tension and compression to generate a counter moment $-M_y$. Assuming that, the movable stage frame rotation, θ_y, yields an elastic axial deformation of a flexure by

$$\delta x_{\theta_y} = 0.5 d_z sin(\theta_y) \approx 0.5 d_z \theta_y, \tag{3.13}$$

where d_z is the vertical distance between flexures. The static equilibrium for a moment M_y and the axial reaction, F_x, in each of the flexures is

$$M_y = 2F_x d_z. \tag{3.14}$$

Using the Hook's relation for the axial deformation, the moment is

$$M_y = \frac{W_f H_f E d_z^2 \theta_y}{L_f}, \tag{3.15}$$

which yields the approximate rotation stiffness,

$$K_{\theta_y M_y(F_x)} = \frac{M_y}{\theta_y} = \frac{W_f H_f E d_z^2}{L_f}. \tag{3.16}$$

The calculated value of $K_{\theta_y M_y(F_x)}$ is $7.18 \cdot 10^3$ Nm/rad. The stiffness $K_{\theta_y M_y}$ should not be, however, limited to the flexure axial stiffness contributions. In addition to displacement δx_{θ_y}, a rotation θ implies a vertical displacement of the flexure δz_{θ_y}. Due to δz_{θ_y}, flexures create bending reaction forces and hence the counter moment to the M_y input. Similar to derivation of Equation (3.16), one can formulate the stiffness contribution of flexure bending deformation $K_{\theta_y M_y(F_z)}$ to the rotational stiffness $K_{\theta_y M_y}$. The rotation θ_y yields the vertical deformation of the flexure

$$\delta z_{\theta_y} = 0.5 \theta_z d_x, \tag{3.17}$$

where d_x is the horizontal distance between the flexure bending reaction forces. The static equilibrium may be written as

$$M_y = 4\delta z_{\theta_y} k_{F_x\delta x} 0.5 d_y, \tag{3.18}$$

and the resulting stiffness

$$K_{\theta_y M_y(F_z)} = \frac{E W_f H_f^3 d_x^2}{L_f^3}. \tag{3.19}$$

The value of $K_{\theta_y M_{y(F_z)}}$ is 79 Nm/rad and is significantly lower than $K_{\theta_y M_{y(F_x)}}$. The value of the stage stiffness $K_{\theta_y M_y}$ depends on the actual contributions of $K_{\theta_y M_{y(F_x)}}$ and $K_{\theta_y M_{y(F_z)}}$ to the rotation resistance. It is difficult to qualitatively evaluate the total stiffness $K_{\theta_y M_y}$, since the actual bending and axial contributions are not known. The $K_{\theta_y M_y}$ stiffness was calculated with a FEM analysis and is estimated to be $1.35 \cdot 10^3$ Nm/rad. The stiffness $K_{\theta_y M_{y(F_x)}}$ is contributing to the stage resistance against rotation θ_y, however, the influence of $K_{\theta_y M_{y(F_z)}}$ is visible by a somewhat reduced value of $K_{\theta_y M_y}$ than directly predicted from $K_{\theta_y M_{y(F_x)}}$. A leaf spring possesses a low torsional stiffness, which is given by [60]

$$k_{M_x\theta_x} = \frac{k_1 W_f H_f^3 G}{3L_f}, \tag{3.20}$$

where k_1 is expressed by

$$k_1 = 1 - \frac{192 H_f}{\pi^5 W_f} \sum_{n=1,3,5\ldots}^{\infty} \frac{1}{n^5} tanh\left(\frac{n\pi d}{2H_f}\right), \tag{3.21}$$

and G is the shear modulus. The torsional stiffness of the stage about the x-axis, $K_{M_y\theta_y}$, is then

$$K_{M_x\theta_{x(T)}} = \frac{4k_1 L_f H_f^3 G}{3L_f}. \tag{3.22}$$

The calculated value of $K_{M_x\theta_{x(T)}}$ is 0.13 Nm/rad. A stage rotation, θ_x, additionally invokes flexure displacements in the y-and z-directions. The associated elastic reaction forces along the y-and z-directions create reaction moments and hence rotational stiffness contributions to $K_{M_x\theta_{x(F_y)}}$ and $K_{M_x\theta_{x(F_z)}}$. Similar to the case of $K_{M_y\theta_y}$, the total stiffness, $K_{M_x\theta_x}$, is a result of all three stiffness contributions, $K_{M_x\theta_{x(T)}}$, $K_{M_x\theta_{x(F_y)}}$ and $K_{M_x\theta_{x(F_z)}}$. The value of $K_{M_x\theta_x}$ was calculated by FEM analysis and is estimated to be $2.54 \cdot 10^3$ Nm/rad. To summarize, the flexure stage possesses a relatively low stiffness in the z-direction whereas the remaining degrees of freedom are considered significantly stiffer. This emphasises the guidance functionality of the stage. A measure of stage guidance along the z-direction can be expressed as a ratio of the off-axis stiffness and the compliant guiding stiffness as

$$R_{x-z} = \frac{K_{F_x\delta x}}{K_{F_z\delta_z}} \approx 320, \tag{3.23}$$

$$R_{y-z} = \frac{K_{F_y\delta y}}{K_{F_z\delta_z}} \approx 2000. \tag{3.24}$$

The maximum expected stage rotations, θ_x and θ_y, were approximated. The maximum force (5.08 N) required for a full stroke stage translation with an offset from the stage axis with maximum possible offsets in y and x, both equal to 0.1 mm, would result in stage rotations, θ_x, equal to 0.37 μrad and θ_y equal to 0.2 μrad.

3.4.4 Mobility analysis

The concept of mobility was used in the design of the positioning stage [60]. Mobility analysis represents flexural elements as links, connected to rigid bodies via joints, providing certain

Table 3.1: Stage stiffness summary.

Symbol	Value
$k_{F_x\delta x}$	150 N/μm
$k_{F_y\delta y}$	986 N/μm
$k_{F_z\delta z}$	0.508 N/μm
$K_{M_x\theta_x}$	$2.54 \cdot 10^3$ Nm/rad
$K_{\theta_y M_y}$	$1.35 \cdot 10^3$ Nm/rad

kinematic constraints to the bodies. A simplified representation of a system indicates number of degrees of freedom it possesses. For analysing in-plane motion, the planar mobility, M_3 is used. For a system consisting of n links and j joints the planar mobility is expressed as [60]

$$M_3 = 3(n - j - 1) + \sum_{i=1}^{j} f_i, \tag{3.25}$$

where f is the number of degrees of freedom provided by the i^{th} joint. The flexural stage can be modelled as two links, the moving frame and the structural frame, connected to each other via four hinges (leaf springs). Each of the hinges provides two degrees of freedom, that is the translation in the z-direction and the rotation about the y-axis. Hence the mobility, M_3 of the system is equal to -1. This value indicates that the system is over constrained. The three dimensional mobility of a system is

$$M_6 = 6(n - j - 1) + \sum_{i=1}^{j} f_i. \tag{3.26}$$

In this case, a leaf spring is to be treated as a hinge providing three degrees of freedom, translation along z, rotation about y, and twist about x. The M_6 mobility is then equal to -6. In this case the system is six times over constrained. The desired stage motion is the pure translation along the z-axis. For such motion, the stage should ideally posses mobility of 1, indicating one degree of freedom. Mobility should not be however associated with identifying a wrong design but rather as a design strategy confirmation. The over constrained design may be an issue, if the kinematic system is assembled, since the assembly may induce strain and stress in flexures. In case of the flexural system discussed, the structure is monolithic and produces a virtually strain-free mechanism. The achieved parallel guidance must be over constrained in order to attain its functionality, yet the amount of over constraint is kept to a minimum level. A slightly over constrained system assures lack of unpredictable mobilities and benefits from the 'elastic averaging' effect which enhances the guidance straightness [60].

3.4.5 Stage elastic deformation

3.4.5.1 Movable frame deformation

The following section covers the actuation induced elastic deformation of the movable stage frame. During actuation, the stage frame deforms in the following fashion. The horizontal

beams bend towards the frame centre, while the vertical beams deflect symmetrically outwards from the stage centre, as indicated in Figure 3.14(a). The deformation of the bottom horizontal beam is particularly important as explained in Section 3.4.2. There are two problems related to the bottom plate deformation. First, the inherent elastic deformation of the target electrode glued to the top face of the plate. Another issue is the vertical translation of the probe mounting spheres as a consequence of plate bending. The probe position is linearly translated and simultaneously rotated with respect to a non-deformed plate situation. These deformations were approximated by FEM analysis. A stage guided by the stiffest flexures allowed by manufacturing tolerances was modelled to represent the most critical and largest deformation scenario. The simulation investigated the elastic deformation due to a 6.1 N input force, which is required to displace the flexures by 10 μm. As mentioned in Section 3.4.2, the movable stage frame was designed for low mass and high stiffness. The influence of mass reduction on the stage elastic deformation was investigated. The FEM analysis of the stage without mass reduction cut-outs is shown in Figure 3.17(a). The nodal displacements along the middle line of the bottom face, 'd' of the stage movable frame were calculated with ANSYS software. The results are plotted in Figure 3.17(c) and show the nodal displacements across the beam length. A typical second order bending deflection of the beam created by the curve fit approximating the bending shape of the structure in Figure 3.17(c). The difference between the largest and the smallest nodal displacement is 30 nm. The relative difference between the mounting spheres position is 11 nm. The stage deformation with mass reduction was modelled and solved as well. The FEM analysis of the stage with mass reduction is shown in Figure 3.17(b). The calculated nodal displacement are shown in Figure 3.17(d). The approximated bending shape is much more complex and there are concave and convex regions visible in the approximated bending curve. This phenomenon can be explained by a non-uniform stiffness distribution along the beam length in the x-direction. There are local regions of low and high stiffness distinguishable in the geometry and corresponding material folding and bending in the bending curve. The simulated value of a difference between the lowest and the highest nodal displacement is 8.5 nm. The difference between the probe mount spheres displacement is 2.5 nm. This concludes the extensive and complex material deformation after mass reduction results in less stage deformation. Even though the structure without the mass reduction is stiffer, the different deflection curve of the beam results in a lower deformation. The elastic deformation analysis also includes the target electrode glued to the top face, 'c', of the bottom horizontal stage beam and its stiffening effect on the frame. The FEM analysis also yielded the following results. The difference between the maximum and the minimum nodal displacement of the face 'd' of the horizontal beam was 3 nm. The difference between nodal displacements at the 2 mm and at the 1.2 mm sphere mounts was 1 nm. The difference between the largest and the smallest nodal displacement at the top face of the target electrode is equal to 5 nm. The deformation of the plate was treated as a beam element, since its deflection is much more pronounced in the X-Z plane than in the Y-Z plane. Treating the plate as deflecting as a function of x-and y-position, the largest deflection along the y-direction was calculated with the FEM analysis and was 1 nm. All the elastic deformation effects mentioned above must be calibrated by means of a static calibration experiment, yet the FEM results indicated the scale of the

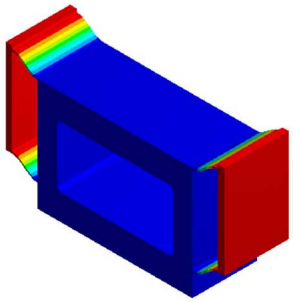

(a) FEA of the movable frame without mass reduction cut-outs (red = 0 μm, blue = - 10.3 μm).

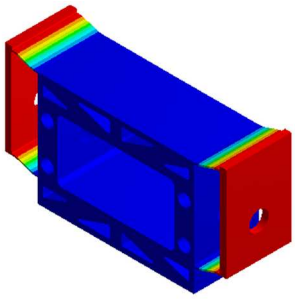

(b) FEA of the movable frame with mass reduction cut-outs (red = 0 μm, blue = - 10.3 μm).

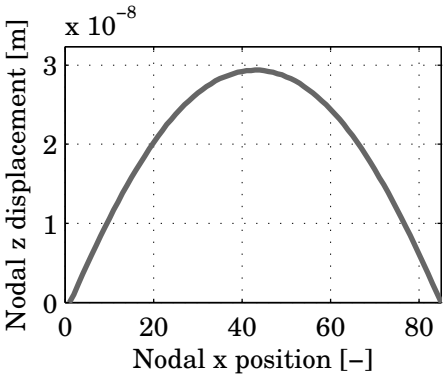

(c) Beam CD deformation shape - stage without mass reduction.

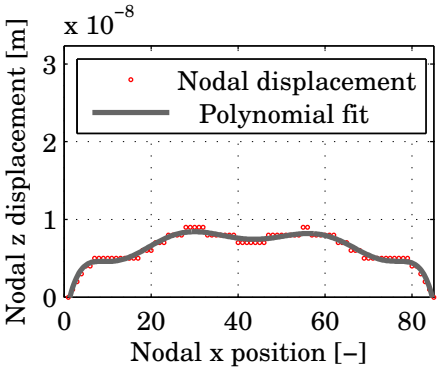

(d) Beam CD deformation shape - stage with mass reduction.

Figure 3.17: Deflection shaping of the CD beam.

anticipated deformation. Using proper design, the elastic deformation of the stage is held to a minimum. The shape and position of the stage frame triangular cut-outs were optimized with FEM software to reduce the effective elastic deformation while keeping the frame stiff enough for sufficiently heigh flexural eigenmodes. This is discussed more in Section 3.4.9.2. Table 3.3 summarizes the advantages of deflection shaping cut-outs and the stiffening effect of the target electrode. The effective deformations of both the probe and capacitance gauge electrode are reduced by over 70% by deflection shaping. The target electrode stiffness contribution reduces these deformations by another 50%. The dynamic mass reduction achieved with these cut-outs was 21%. Even though the triangular and circular cut-outs in the movable stage frame were introduced for two distinct purposes, measurement error reduction and dynamic mass reduction, their presence is more pronounced and important in the first one.

3.4.5.2 Structural frame deformation

The actuator exerts a force on the structural stage frame at face 'a'. The elastic deformation of the frame caused by this force was investigated while designing the scanner. The reactions caused by the actuator force input, F_{PZT}, are shown in Figure 3.18(a). There are two vertical force reactions, R_1 and R_2, and two reaction moments M_1 and M_2 at the points where the stage

Table 3.2: Deflection shaping summary.

Stage design	Electrode inherent deformation	Probe inherent displacement
No deflection shaping (no electrode)	30 nm	10 nm
Deflection shaping (no electrode)	8.5 nm	2.5 nm
Deflection shaping (with electrode)	3 nm	1 nm

is fixed to the external metrology frame. The reaction forces, F_3 and F_4, are compression forces by the metrology brackets, on the vertical structural frame beams, ensuring they do not bend towards each other. Essentially, these forces are creating counter moments for M_1 and M_2. The stage stiffness against M_1 and M_2 is determined by the bending stiffness of the vertical structural frame beams with considerable stiffening chamfers and the axial stiffness of the metrology brackets. The latter one is significantly high, contributing a negligible deformation of the structure due to the actuation force F_{PZT}. The FEM model was used to investigate the deformation of the structure in more detail and the results are presented in Figures 3.18(c) and 3.18(e). There is a local stress region in the centre of the stage where the actuation force is exerted on the top segment of the structural frame. Additionally, the middle section of the stage, which is rigidly attached to the metrology brackets, is not affected by the stress. However, the sections of the structural frame vertical beams, which are not rigidly attached to the metrology brackets, deform somewhat more due to the induced stress, as shown in Figure 3.18(e). In other words, part of the stage is locally deformed to accommodate for the locally induced stresses. This leads to the movement of the entire stage assembly upwards, which introduces a force measurement error due to the probe vertical displacement. This deformation can be reduced by spacing the bolting interfaces closer to each other which results in a smaller arm, $0.5D$, of the force F_{PZT} and, consequently, smaller reaction moments M_1 and M_2. This relation has been confirmed with the FEM analysis. The above mentioned spacing, D, is influencing the stage assembly dynamics, as explained in Section 3.4.9, and it is desired to keep it as large as possible. This conflict yielded a careful optimization of the bolted interface separation, D, so that both design objectives, a low structural frame deformation and a sufficiently high natural frequencies, are met. Other methods to reduce the structural frame deformation can be performed by transferring the actuation force to the global metrology frame, as shown in Figures 3.18(b) and 3.18(d). Practically this can be realized by an additional bolt touching the stage top face and directly transforming the actuator force to the microscope frame. FEM analysis shows the stress transfer reduces the stage deformation by a factor of 2. The dynamic force transmitted to the frame by the actuator is of special importance, since it can not be calibrated out from the measurement data. The reason for this is the frequency dependence of the actuation force. The maximum dynamic force of the actuator is equal 5.2 N. The stage deformation along the z-axis returned by FEM analysis was 1.1 nm. Additionally,

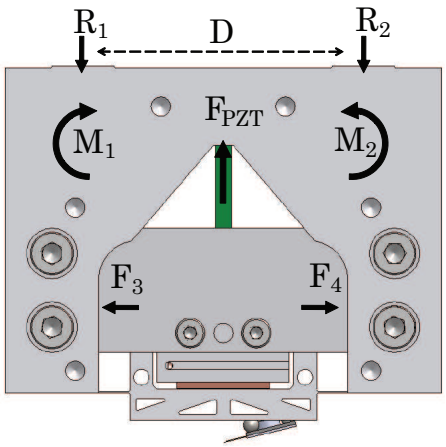

(a) Structural frame deformation - reaction forces in the stage assembly.

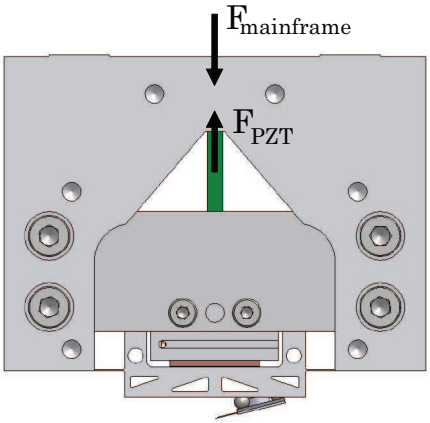

(b) Structural frame deformation - with an additional transferring bolt.

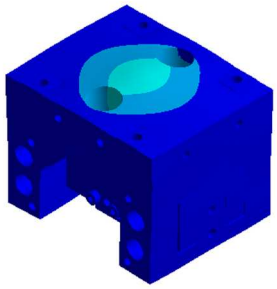

(c) FEA of the structural frame deformation (dark blue = 0.75 nm, light blue = 6.7 nm).

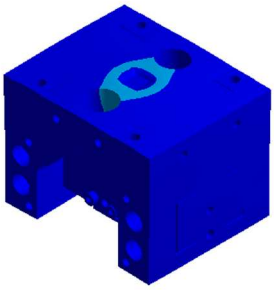

(d) FEA of the structural frame deformation with an additional transferring bolt (dark blue = 0.2 nm, light blue = 2.6 nm).

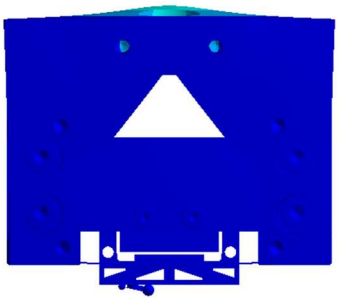

(e) FEA of the structural frame deformation - front view (dark blue = 0.75 nm, light blue = 6.7 nm).

Figure 3.18: Analysis of the structural frame deformation due to actuator force input.

the critical buckling load of the flexures was calculated and flexure buckling should not occur due to the forces transformed to the flexures axially through the frame. A low dynamic mass is advantageous in the context of structural frame deformation. Low actuated mass reduces the stage inertia force which in turn limits the dynamic actuation force exerted on the structural frame, thus reducing the elastic deformation of the frame.

3.4.6 Piezoelectric actuator

A piezoelectric stack was chosen as the actuator for the stage. Piezoelectric actuators present favourable advantages to be used in positioning stages [5]. Namely, they are commercially available in a wide range of sizes, attainable displacements, are cost effective, and occupy little volume. Moreover, a piezoelectric stacks provide high stiffness and the actuator achieves a very high response performance. The actuator used is the PSt 150/2x3/20 piezoelectric stack from Piezomechanik GmbH. This actuator has the highest stiffness in comparison with other commercial alternatives, while providing sufficient stroke for the scanner operation. The actuator provides a maximum nominal stroke, $\delta z_{pzt(max)}$, of 20 μm and a maximum blocking force of 300 N. The nominal stiffness of the actuator is 12 N/μm. The actuator must be preloaded with a force, $F_{preload}$, of 30 N, thus it can effectively actuate with a maximum fore equal to 270 N. This force must be sufficient to accommodate for a maximum elastic force arising from flexures, a maximum inertia force and a maximum damping force. Mathematically the maximum force generated by the actuator is

$$F_{max} > \delta z_{max} \left[2m_s \pi^2 f_b^2 + \left(K_{\delta_z F_z} + K_{pzt} \right) + \pi f_b c_s \right], \tag{3.27}$$

where m_s is the movable mass of the stage, δz_{max} is the stage travel range and c_s is the generalized stage damping coefficient. The damping present in the system is the internal Zener damping [5] of aluminium, air damping, and squeeze film damping which all have negligible effects (in the scale of forces considered), hence are not treated in Equation (3.27). The maximum actuating force approximated with Equation (3.27) is 120 N, which is less than 50% of the actuator blocking force. Operation with a fraction of the actuator blocking force or correspondingly with a fraction of maximum stroke yields a benefit of lower ohmic heat generation if one compares it with an alternative actuator performing at its full nominal displacemt. The stroke of a piezoelectric actuator is limited, when it acts against an elastic load, like a preload spring. The reduction of the nominal stroke, $\delta_{pzt(max)}$, is depending on the ratio of the stiffness of the actuator, k_{pzt}, and the stiffness of the preload, $k_{preload}$ by [61]

$$\delta_{pzt} = \delta_{pzt(max)} \frac{k_{pzt}}{k_{pzt} + k_{preload}}, \tag{3.28}$$

where δpzt is the reduced maximum stroke by the piezoelectric actuator. In the designed stage, the flexures are preloading the actuator and they are significantly more compliant than the actuator, hence the nominal stroke is reduced by approximately 4%. This is another advantage of applying low stiffness guidance flexures. It is important to ensure the actuator is preloaded by a minimum preload, $F_{preload}$, at all instances while operating. The preload is achieved by inserting the piezoelectric actuator into the gap 'a-b', see Figure 3.13, so the flexures deform in the z-direction and exert elastic reaction force on the actuator. This is accomplished by a clearence for the actuator being smaller than its length, L_{pzt}. The difference between the actuator length and the clearance for the actuator is equal to the displacement of the flexures necessary to insert the actuator into the stage. This displacement should provide at least a preload force, $F_{preload}$. Care must be taken to make ensure this is accomplished, since an insufficiently preloaded actuator may perform worse than originally specified or even become

damaged. The length of the piezoelectric stack, L_{pzt}, is defined by manufacturer with a 30 µm tolerance. The actuator was measured with a micrometer and its length is known up to 10 µm, which is the uncertainty of the micrometer measurement. Also the clearance gap, in the stage, L_{a-b}, is manufactured with a tolerance of 10 µm, see Appendix A. This means the flexures will be deflected by a value up to the sum of these tolerances, $\Delta\delta z_{preload}$ = 20 µm. In addition, the manufacturing of the flexures is possible within certain tolerances, see Appendix 1. These tolerances span the possible range of stage stiffness. The lowest possible stiffness of the flexures, $K_{\delta z F_z(min)}$ was determined via FEM simulation. The minimum travel range of the flexures to accommodate force $F_{preload}$ is determined by

$$\delta_{preload} = \frac{F_{preload}}{K_{\delta z F_z min}}. \tag{3.29}$$

The clearance for the actuator should force at least this displacement of the flexures. Thus, the manufacturing gap tolerances and the actuator length tolerances are included in the final formula for the clearance

$$L_{a-b} = L_{pzt} - \delta z_{preload} - \Delta\delta z_{preload}. \tag{3.30}$$

The actuator was inserted into the stage after deflecting the stage by the desired clearance. This was achieved by hanging a known mass on the movable frame. Another important aspect is an accurate placement of the actuator along the centre axis of the movable stage. An off-axis placed actuator produces a moment about the x-and y-axes when driving the flexures, which implies an out of plane stage displacement and a related measurement error. Central alignment of the piezoelectric stack minimizes the moment force arm, hence the undesired moments and their effects on the measurement are reduced. To archive this, a reference part, shown in Appendix A in draft number P90427b-100-0008a, was designed. This element determines the actuator position with respect to the movable frame faces within 50 µm. The design of the stage relies on the high stiffness of the piezoelectric actuator. Depending on whether the shunts of the actuator are open or closed, the stiffness of the actuator changes by [62, 63]

$$k_{short} = k_{open}(1 - k_{33}), \tag{3.31}$$

where k_{short}, k_{open} are the mechanical stiffness of the piezoelectric actuator with correspondingly closed and open leads and k_{33} is the electromechanical coupling factor. The electromechanical factor, k_{33}, is defined as [62]

$$k_{33} = \sqrt{\frac{{d_{33}}^2}{{s^E}_{33}{\epsilon^T}_{33}}}, \tag{3.32}$$

where d_{33} is the induced polarization in the direction along actuator length per unit stress applied in this direction, ${s^E}_{33}$ is the elastic compliance of the actuator for stress in the direction along its length and accompanying strain in this direction under constant electric field (short circuited leads) and ${\epsilon^T}_{33}$ is the permittivity for dielectric displacement and electric field in the direction along the actuator length under constant stress. From Equations (3.32) and (3.31) the potential stiffness reduction of the actuator with closed leads was calculated to be

53.7% of the stiffness measured with the open leads. This is a significant loss of additional electromechanical stiffness and a special driving should be applied. The actuator should be driven by a charge amplifier rather than a power voltage amplifier, to deliver the highest possible stiffness to the stage. A charge amplifier was not available for this research , thus a power amplifiers was chosen, which is discussed in the following section. The stage design is relying on the charge amplifier for optimal driving conditions, which should be implemented in the future.

3.4.7 Piezoelectric actuator amplifier

The piezoelectric actuator performance depends on both the actuator its driving power supply. The power supply should provide enough voltage to achieve the desired actuator stroke. Driving a piezoelectric actuator is similar to driving a large capacitor. Apart from the required voltage, a sufficient current level must be delivered. Another important aspect of the power supply is its cut-off frequency up to which a certain capacitive load can be driven. This characteristic is specified in the voltage attenuation curves plotted for different capacitive loads versus frequency of operation. The following section describes the calculations performed to ensure that the power supply ratings are sufficient to drive the flexural stage with the PSt150/2x3/20 piezoelectric actuator. The PSt 150/2x3/20 actuator has the following characteristics, which are important from the power supply point of view. The nominal capacitance, C_n is 340 nF, and the maximum voltage range, V_{min} to V_{max}, is - 30 V to + 150 V. The maximum stroke available for unipolar operation, $\delta z_{pzt(max)}$ is 20 μm, and corresponds to a voltage change from 0 V to V_{max} of 150V. The nominal capacitance, C_n, is specified by the actuator supplier with a tolerance of ± 15%. Furthermore, piezoelectric actuators are not ideal capacitors and the capacitance value is affected e.g. by the applied voltage or load conditions [64]. Therefore, it is a common practice to multiply the nominal capacitance by a safety factor of 1.5 when evaluating the current requirements for the power supply [64]. This modified capacitance value, C_m, is 510 nF for this research. Let us assume the piezoelectric actuator is to position the stage sinusoidally with an amplitude, A, of 5 μm at a frequency, f_b, of 2 kHz. The necessary actuator displacement is then equal to the half of the maximum stroke possible ($0.5 \cdot 20$ μm = 10 μm),V_{max} (+75 V). Hence, the power supply must provide a voltage from, U_{min} = 0 V to U_{max} = +75 V to generate the necessary actuator displacement. The actuator's equation of motion is

$$z(t) = 0.5A\,(1 - cos(2\pi f_b t)), \tag{3.33}$$

which corresponds to the voltage signal, $U(t)$, sent by the power supply to the actuator

$$U(t) = 0.5U_{max}(1 - cos(2\pi f t)). \tag{3.34}$$

For a capacitor, the following relation holds [64]

$$I(t) = C\frac{dU(t)}{dt}. \tag{3.35}$$

Using Equations (3.34) and (3.35), the current provided by the supply voltage is [64]

$$I(t) = U_{max}C\pi f sin(2\pi f t)). \tag{3.36}$$

The power supply must deliver the average current, I_a, defined by [64]

$$I_a = U_{max} C_m f, \tag{3.37}$$

which is equal to 76.5 mA, and the peak current, I_p, defined by [64]:

$$I_a = \pi U_{max} C_m f, \tag{3.38}$$

which is equal to 240 mA. The analogue power amplifier LE 150/025, shown in Figure 3.19(a), was selected to drive the piezoelectric actuator. This amplifier can provide a voltage from -

(a) Power amplifier used [64].

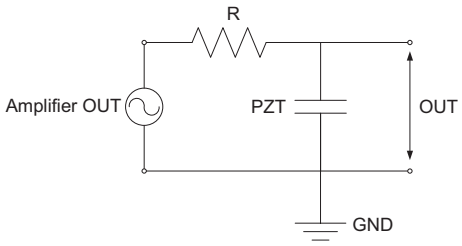

(b) Series resistor connection to the PZT in an RC network.

Figure 3.19: Power amplifier used and a series resistor connected to the piezoelectric actuator.

30 V to +150 V, an average current of 350 μA, and a peak current of 2000 μA. The variable voltage attenuation curve is specified for a 0.47 μF load and the cut-off frequency is 4 kHz. The maximum voltage attenuation down to a voltage level of +75 V occurs at approximately 8 kHz, which is four times higher than the maximum frequency of operation. The amplifier performance of the amplifier is clearly sufficient. A 20 V_{p-p}, 20 Hz sinusoidal voltage signal across the piezoelectric actuator connected to the LE 150/025 amplifier, which was acquired via an Agilent DSO3062A oscilloscope and an Agilent 3000 series data acquisition software, is presented in Figures 3.20(a), 3.21(a) and 3.22(a). Additionally, the Fast Fourier Transforms (FFT) of the recorded signals are shown in Figures 3.20(b) and 3.21(b). Figure 3.20(a) represents the case of the piezoelectric actuator being connected directly to the amplifier output. This has a considerable noise level in this signal which must be eliminated. The time scale of the measurement shown in Figure 3.20(a) is not covering properly the frequencies of the noise signal, hence the FFT of the signal is showing only a clear 20 Hz peak. A close up at the higher frequencies present in the voltage signal was achieved by changing the horizontal scale of the oscilloscope into the higher frequencies regime and the acquired signal is presented in Figure 3.21(a). The FFT analysis of this signal indicates the frequencies present at 14.6 kHz, 19 kHz, 26.8 kHz, 39 kHz, and 114 kHz. To overcome this problem, a resistor, R, was added in series with the piezoelectric actuator, as shown in Figure 3.19(b), forming a passive low-pass filter

$$\omega_{RC} = \frac{1}{RC_{pzt}}, \tag{3.39}$$

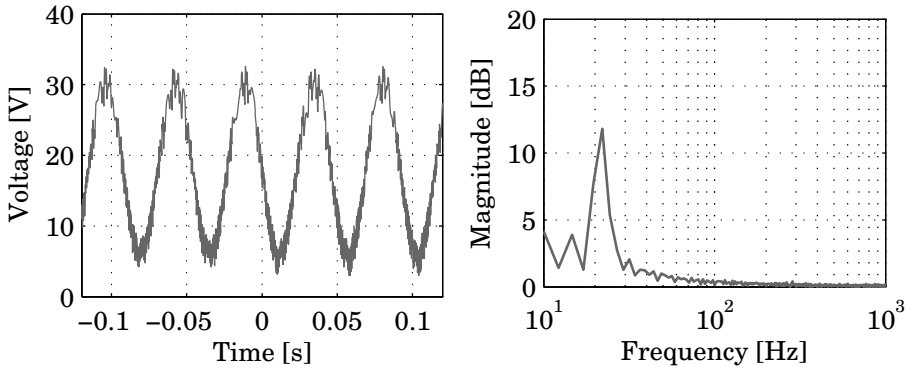

(a) Actuator voltage (20 ms/div). (b) FFT of the actuator voltage (20 ms/div).

Figure 3.20: Noise signal on the amplifier output and its FFT.

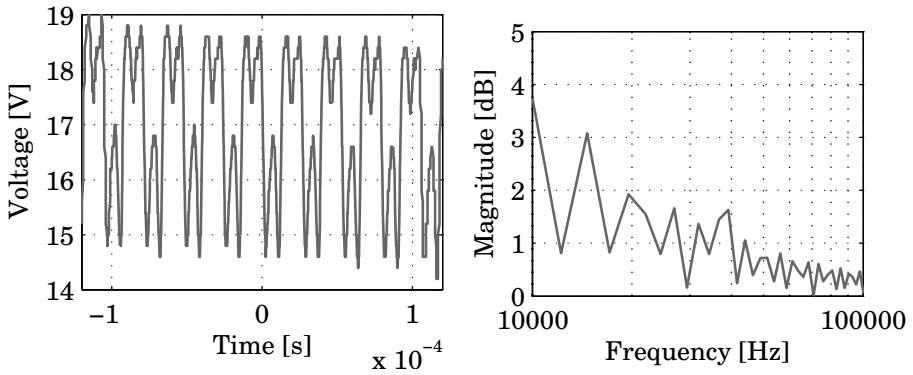

(a) Actuator voltage (50 μs/div). (b) FFT of the actuator voltage (50 μs/div).

Figure 3.21: Noise signal on the amplifier output and its FFT (close up).

where ω is the cut-off frequency, R is the resistance of the resistor, and C_{pzt} is the piezoelectric actuator capacitance. The series resistor, R, is limiting the current delivered by the amplifier and the RC network is attenuating the higher frequency components of the voltage signal. The different values of resistance, R, were used in order to eliminate the noise component of the signal and it appeared the noise reduction is not dependent on the cut-off frequency of the low pass filter, as expected. The conclusion is the noise signal visible in Figures 3.20(a) and 3.21(a) is resulting from an insufficient load across the amplifier output and the internal electronics have problems related to this phenomenon. A series resistor increases the load at the amplifier output and therefore limits the current supplied by the amplifier. Moreover, the above mentioned reasoning was confirmed by driving smaller capacitors, on the order of $0.5C_{pzt}$ and less, by the amplifier, where the amplifier output became unstable. Increasing the capacitance value of the driven capacitive load, by an additional parallel capacitor, or adding a series resistor to the capacitor stabilised the amplifier. Of these two solutions, the additional resistor is preferable, since the increasing of the capacitive load would limit the cut-off frequency of the amplifier and negatively affect the system performance. A 10 Ohm resistor, was used to limit the current output of the amplifier and stabilize the voltage signal across the piezoelectric ac-

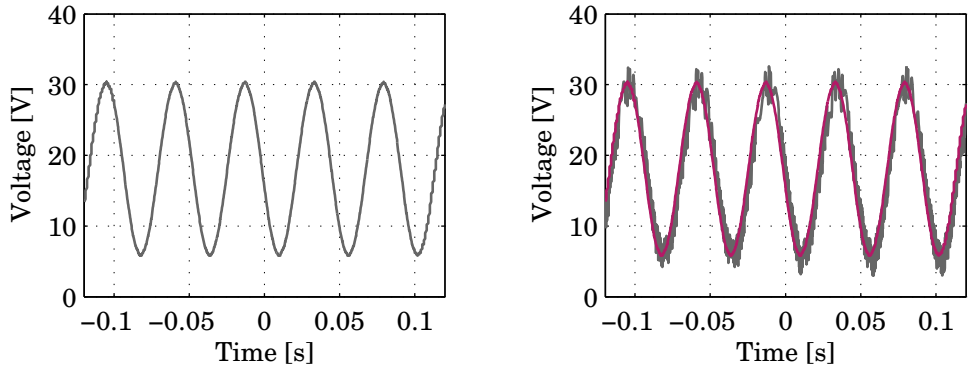

(a) Actuator voltage with a 10 Ohm series resistor (20 ms/div).

(b) Comparison of voltage signals across PZT for the cases with and without a series resistor.

Figure 3.22: Stabilized signal on the amplifier output.

tuator. The resulting voltage signal with the series resistor, R, is shown in Figure 3.22(a) and the high frequency noise in no longer present. A comparison of the voltage signals across the piezoelectric actuator with and without the additional series resistor, R, is shown in Figure 3.22(b).

3.4.8 Stress analysis

As outlined in Section 3.4.6, flexures theoretically deflect by $\delta z_{preload} + \Delta\delta z_{preload}$ when the actuator is inserted into the stage. However, the manufacturing tolerances of the actuator length, L_{pzt}, and the gap clearance, L_{a-b}, introduce an additional uncertainty, $\Delta\delta z_{preload}$, in the flexures deflection. Additionally, while operating, flexures displace by a maximum value equal to scanner travel range, δz_{max}. The maximum deflection of flexures is

$$\delta z_f(t) = \delta z_{preload} + 2\Delta\delta z_{preload} + 0.5\delta z_{max} + 0.5\delta z_{max} sin(\omega t), \tag{3.40}$$

which indicates a cyclic motion of flexures with a mean, non-zero offset deflection. In Equation (3.40) the mean deflection is

$$\delta z_{mean} = \delta z_{preload} + 2\Delta\delta z_{preload} + 0.5\delta z_{max}, \tag{3.41}$$

and the cyclic deflection amplitude is

$$\delta z_A = 0.5\delta z_{max}. \tag{3.42}$$

The deflection $\delta z_f(t)$, is related to a cyclic stress occurring in the flexures. The stress characteristic is comprised of a means stress, σ_{mean}, related to the mean deflection, δz_{mean}, and a cyclic stress of amplitude σ_A, related to the cyclic displacement, δz_A. The bending stress in flexures is approximated by

$$\sigma_b = \frac{3EH_f\delta z_f}{L_f^2}. \tag{3.43}$$

From Equation (3.43), the bending stress in the flexure depends on its, L_f, and thickness, H_f. The manufacturing tolerances of these dimensions were included in the stress approximation and FEM analysis, assuming the shortest and the thickest possible flexures. Thus, the maximum mean stress can be approximated by

$$\sigma_b = \frac{3E(H_f + \Delta H_f)\delta z_{mean}}{\left(L_f - \Delta L_f\right)^2}. \tag{3.44}$$

The value of the static bending stress, σ_{mean}, was calculated using Equation (3.44) and is equal to 396 MPa. In addition to the bending stress, there is an axial stress occurring in the flexures. It is from the axial elongation of the flexures necessary for parallel translation of the stage. The elongation of the leaf springs is approximated by [60]

$$\delta x = \frac{3(\delta z_f)^2}{5L_f}. \tag{3.45}$$

The corresponding tensile stress is expressed as

$$\sigma_t = \frac{3E(\delta z_f)^2}{5L_f^2}. \tag{3.46}$$

The maximum mean tensile stress was calculated with

$$\sigma_t = \frac{3E(\delta z_{mean})^2}{5\left(L_f - \Delta L_f\right)^2}. \tag{3.47}$$

This highest expected tensile stress is 44 MPa. The tensile and bending stresses act in the same direction, hence they can be added. The total mean flexure stress is 440 MPa. The analytical solution was supported with a FEM analysis of the von Misses stress which was 445 MPa. Additionally, the FEM analysis covered the additional fillets modelled with the largest radius, R_f, allowable by the manufacturing tolerances. Similarly as in the case of the stiffness calculation, the FEM results were used as the base for the design, since they cover a more comprehensive estimation. The cyclic stress amplitude, σ_A, was calculated as 17.3 MPa. The maximum stress in the flexures under static condition corresponding to the case of potentially largest deflection, $\delta z_{f(max)}$, is

$$\delta z_{f(max)} = \delta z_{preload} + 2\Delta\delta z_{preload} + \delta z_{max}, \tag{3.48}$$

which was 470 MPa. This value corresponds to 93% of the material material yield limit [65]. The FEM simulation result indicates the maximum van Misses stress is shown in Figure 3.23. As for the cycling stress analysis, the maximum allowable amplitude, σ_{all}, is predicted from the value of maximum stress, σ_0, corresponding to N cycles to failure for reverse compressive and tensile loading, using the Goodman [60] formula by

$$\sigma_{all} = \sigma_0\left(1 - \frac{\sigma_{mean}}{\sigma_u}\right), \tag{3.49}$$

where σ_u is the ultimate strength of material. The calculated σ_{all} for $N = 5 \cdot 10^8$ cycles was 51.3 MPa, thus the maximum cyclic stress amplitude, σ_A, amounts for 33% of an allowable stress

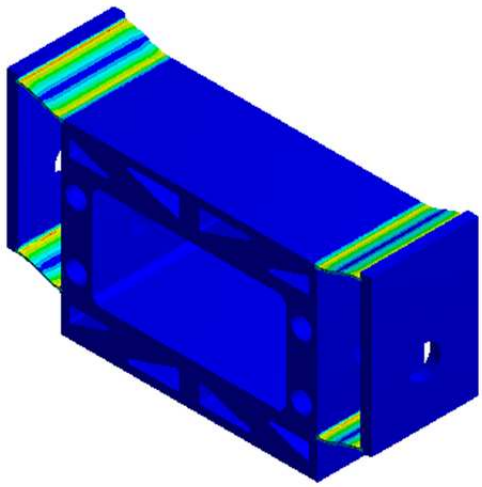

Figure 3.23: Von Misses stress simulation (dark blue = 0.0035 MPa, red = 468 MPa).

amplitude for N cycles, σ_{all}. The stress can be treated as static, prone to the very little cyclic stress with respect to the mean stress value. One should also consider the maximum static stress value predicted represents the scenario of all the manufacturing tolerances contributing to the highest possible stress value. The maximum stress value for the nominal model is equal to 325 MPa, which corresponds to 64% of material yield limit.

3.4.9 Dynamic analysis

The following Section covers the main aspects of the stage dynamics. As mentioned in Section 3.4.1, the controllable and observable eigenmode of the positioning stage, should occur at 6 kHz or higher. Another important issue is to keep all other eigenmodes higher than 6 kHz, preferably at the frequencies at least 500 Hz higher than the first flexural mode.

3.4.9.1 Analytical model

The natural frequency of the flexural mode is approximated by assuming the mass of the stage, together with the mass of the isolation glass, sensor target electrode, and AFM probe with its mount all, fully contribute to the kinetic energy of the eigenmode and are equal to m_s. However, the piezoelectric actuator and leaf springs are effectively not moving their entire mass in this mode and only a fraction of their mass is lumped into an effective mass, which participates in the mode. The effective mass of the piezoelectric actuator, $m_{pzt(eff)}$, in the case of an axial vibration is taken as [61]

$$m_{pzt(eff)} = 0.33 m_{pzt}. \tag{3.50}$$

The effective mass of the leaf springs, $m_{f(eff)}$, in case of a flexural mode (bending about the y-axis) is [60]

$$m_{f(eff)} = 0.743 m_f. \tag{3.51}$$

The flexural stage frequency, f_s, is approximated by

$$f_s = \frac{1}{2\pi}\sqrt{\frac{k_{pzt} + K_{F_z\delta z}}{m_s + m_{f(eff)} + m_{pzt(eff)}}}, \tag{3.52}$$

where k_{pzt} is the piezoelectric actuator axial stiffness. The frequency was calculated according to Equation (3.52), with k_s value determined via FEA, was 6.97 kHz. A 5% safety margin is assumed for the analytical approximation in Equation (3.52). In case of the least favorable model validity, the target frequency is predicted at 6.6 kHz, which satisfies the design objectives. As mentioned in the Section 3.4.6, the stiffness of the piezoelectric actuator driven by a voltage amplifier is reduced with respect to the stiffness measured with the open leads of the actuator. Thus hence the Equation (3.52) should be updated by a stiffness reduction factor, b_{red}

$$f_{s(red)} = \frac{1}{2\pi}\sqrt{\frac{b_{red}k_{pzt} + K_{F_z\delta z}}{m_s + m_{f(eff)} + m_{pzt(eff)}}}. \tag{3.53}$$

After including the reduced stiffness factor b_{red} of 53 %, calculated in Section 3.4.6, the first resonant frequency should occur at 5.13 kHz. This resonance is lower than initially designed for, yet it is possible to reach the higher first resonance, f_s, when driving the piezoelectric actuator with the charge amplifier. Additionally, the stiffness reduction factor, b_{red} is a coarse approximation of the stiffness reduction and represents the case of no electromechanical stiffness contribution from the piezoelectric actuator. It depends also on the driving signals and voltage amplitudes applied to the actuator. Due to the large uncertainty of an actual b_{red}, the stiffness reduction anticipated is between 0 and 53%, which corresponds to the first natural frequencies of the stage between 5.13 kHz and 6.8 kHz.

3.4.9.2 FEM modal analysis

Modal analysis of the scanner assembly was performed with FEM software and is presented in the following section. The assembly includes the scanner without the piezoelectric actuator, AFM probe, and magnetic mounting plate. The boundary condition of the modal solution is a fixed support of elements highlighted in Figure 3.24(b), which represent bolts fixing the stage. The first eigenmode, see Figures 3.24(c) and 3.24(d), is the flexural vibration of the stage flexures. The eigenshape is the guidance motion, which is controllable and observable. The frequency returned by the system for this mode is not including the coupled stiffness of the actuator, hence is much lower, than analytically predicted by Equation (3.52). However, the approximation from Equation (3.52) with the neglected masses uncovered by the FEM model and neglecting the stiffness contribution of the actuator, the result match FEM result within 3%. The second vibrational mode is presented in Figures 3.24(e) and 3.24(f) and is predicted at 7.82 kHz. The eigenshape is created by a rocking motion of the movable frame about the y-axis, which is accompanied by a flexural, in phase, vibration about the y-axis of the structural frame vertical beams. Leaf springs are folding into ‘s’ shapes about the y-axis due to the rocking motion of the stage. The frequency of the mode is influenced by the stiffness of the movable frame. It can be seen in Figure 3.24(e) that the stage frame beams deform. The distance between the flexures along the z-axis is enhancing the modal stiffness of the stage,

hence the flexures are spaced as far as possible from each other. The structural frame stiffness against flexural motion in the x-direction was enhanced by introducing large chamfers in the frame and adding more material along the x-direction in vertical beams of the stage. Lastly, the resonance frequency of the second mode is influenced by the x separation of mounting pads. On one hand, a larger spacing, generates a higher the resonance frequency of the mode. On the other hand, a smaller spacing between the pads reduces the elastic deformation, as explained in Section 3.4.5. The distance between the mounting pads is optimized for meeting both design objectives. The third mode is shown in Figures 3.24(g) and 3.24(h) and is predicted at 7.99 kHz. The mode shape is a combination of a torsional vibration of flexures about the x-axis and a flexural vibration of the structural frame about the x-direction. The frequency of vibration is affected by the structural frame stiffness in the y- direction, hence the structural frame was designed to significantly protrude out of the X-Z-plane. Such a material distribution provides a high moment of inertia about the x-axis of the structure. The clamps are spaced as far as possible along the y-direction in order to enhance the structural frame stiffness in the x-direction. On one hand, the structural frame material along the x-direction significantly increases the modal mass of the frame in the second eigenmode, without contributing to its modal stiffness. On the other hand, stiffening of the frame in the x-direction contributes to the modal mass of the third mode without significant contribution to its modal stiffness. This yielded a careful optimization of the structure to have both second and third mode occurring at sufficiently high frequencies. Similarly as in the second mode, the mounting connection separation along the y-axis is also increasing the eigenfrequency, hence the mounts are placed as far as possible from each other in the y-direction.

3.4.10 Stage cover

An aluminium cover was designed to protect the positioning stage from dust. A detailed view of the part is presented in Appendix A in draft number P90427b-100-0007b. The cover is bolted to the stage by M3 bolts. A 0.25 mm part of a movable stage frame protrudes from the cover, to allow the attachment of a reflective surface to the movable frame when the calibration, by means of a laser interferometer, is performed. There are two holes in the bottom face of the cover, through which electrical connections from the AFM probe run. The four contact pads on the top face of the structural stage frame protrude from the cover, so that the contact pads define the contact area with the microscope frame. The cover was designed for high resonance frequency. Figure 3.25(d) shows the simulated first resonance frequency obtained via FEM modal analysis. The holes used for the bolt connection to the stage are fixed. The first resonant mode of the cover is a vibration of its bottom side and occurs at approximately 9 kHz. Furthermore, a modal analysis of the stage assembly including assembled cover was performed. The FEM analysis showed the sliding fit between the stage structural frame and stage cover results in much higher eigenfrequencies of the assembly than with a loose fit between the two. In loose fit case, the stage-cover contact was modelled only in the close area of bolted connection. In case of a sliding fit, the stage assembly is stiffened by the cover in much larger extend, due to the larger contact between components faces, which results in the higher natural frequencies

of the assembly. The maximum possible clearance between the stage and the cover is 50 μm, see Appendix A, to achieve a sliding fit assembly. The results of the modal analysis of the stage assembly with cover attached returned an unchanged first resonance frequency, however the second and the third mode of vibration are similar to the second vibration mode with the cover removed, described in Section 3.4.9. The natural frequencies of these modes are subsequently equal to 8042 Hz and 8623 Hz. This can be explained by the stiffening effect of the cover.

Table 3.3: Summary of FEM modal analysis.

Mode	without cover	with cover
1	1.4 kHz	1.44 kHz
2	7.85 kHz	8.6 kHz
3	8 kHz	10.4 kHz

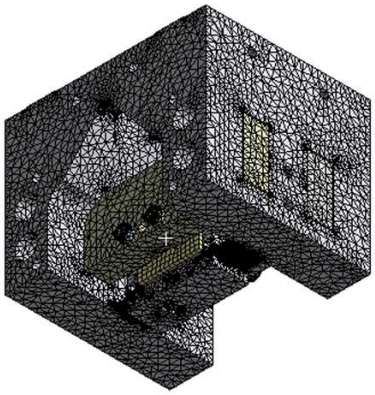

(a) Mesh of a model.

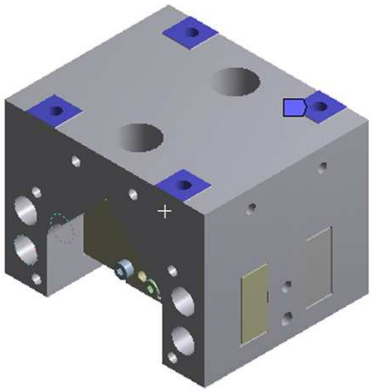

(b) Clamped surfaces.

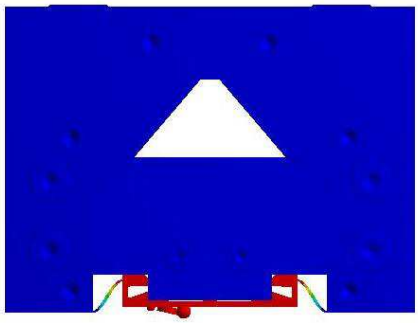

(c) The first eigenmode at 1.4 kHz.

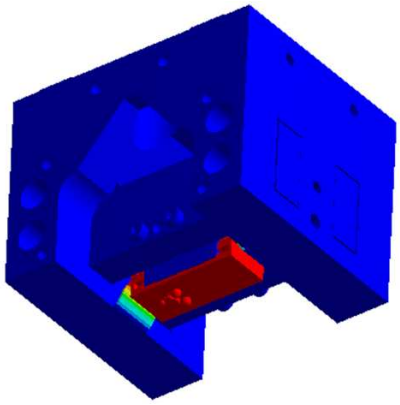

(d) The first eigenmode - isometric view.

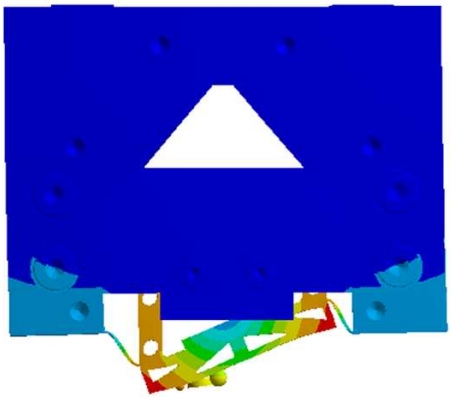

(e) The second eigenmode at 7.85 kHz.

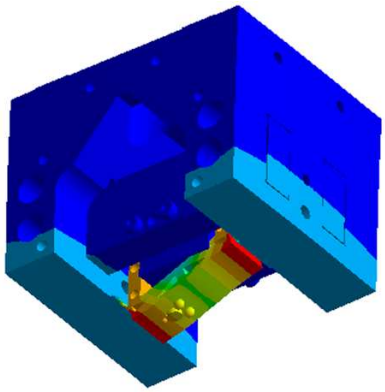

(f) The second eigenmode - isometric view.

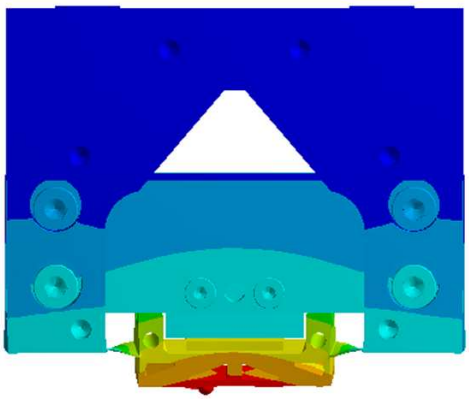

(g) The third eigenmode at 8 kHz.

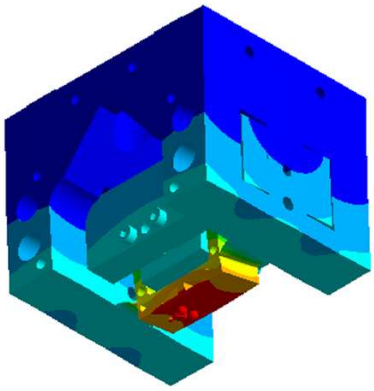

(h) The third eigenmode - isometric view.

Figure 3.24: Modal analysis of the structure.

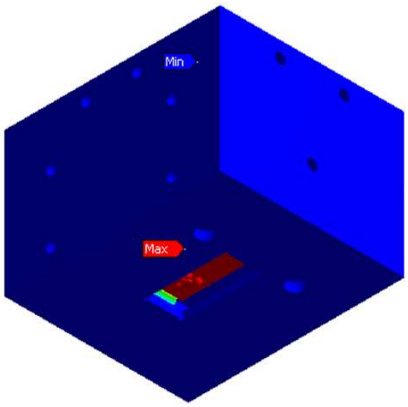

(a) The first eigenmode at 1.44 kHz.

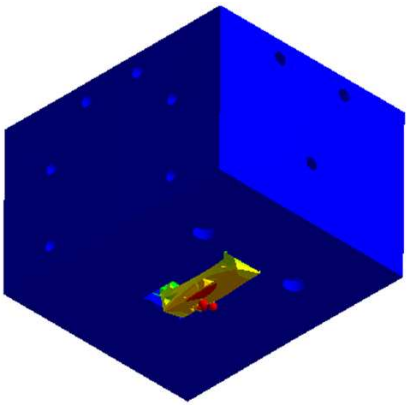

(b) The second eigenmode at 8.62 kHz.

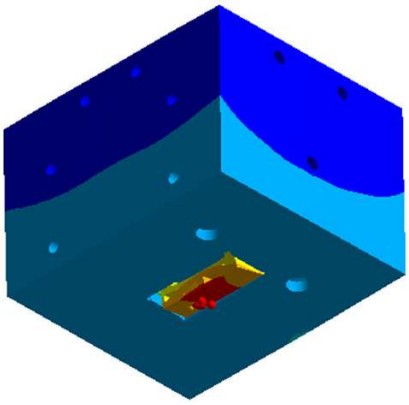

(c) The third eigenmode at 10.4 kHz.

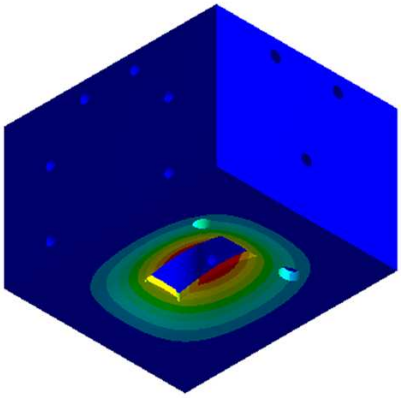

(d) The first eigenmode of the cover itself at 9 kHz.

Figure 3.25: Modal analysis of the structure with the cover on.

3.5 Capacitive sensor

3.5.1 Working principle

The following Section describes the capacitive sensor used for stage position feedback. The capacitive sensing system comprises a capacitive probe and commercial electronics. This measurement system provides a low cost, simple metrology tool which attains sub-nanometre resolution. Another advantage is the design freedom of the capacitive probe, which does not impose any limitation on the positioning stage design and vice versa. The measurement system detects the capacitance change between the stationary sensing electrode and the target electrode attached to the movable stage. The capacitance of a system of two electrodes of area A_c, spaced by a gap h, in air is expressed by

$$C = \frac{\epsilon A_c}{h}, \tag{3.54}$$

where ϵ is the electric permittivity of the medium between the electrodes. Capacitance is inversely proportional to the electrodes spacing, h, hence the capacitance change indicates a relative displacement, provided that area of overlap between electrodes, A, remains unchanged. The sensitivity of a capacitive measurement is

$$S_c = \frac{-\epsilon A_c}{h^2}, \tag{3.55}$$

which shows a quadratic dependence of the measurement sensitivity, S_c. The noise of the capacitive sensor can be expressed by [66]

$$E_c = \frac{4d_0}{V_s}\sqrt{f_b\left[{V_n}^2 + \frac{4kBT}{3C_0 f_c} + \left(\frac{2I_n}{3C_0 f_c}\right)^2 + {O_n}^2\right]}, \tag{3.56}$$

where kB is the Boltzmann constant, T is a temperature in Kelvins, f_c is the carrier frequency in Hertz, I_n is the current noise, V_n is the voltage noise, C_0 is the sensor capacitance at the nominal offset gap, V_s is the supply voltage, O_n is the oscilloscope noise. From Equation (3.56) the sensor noise level is inversely proportional to the electrodes capacitance. To reduce the sensor noise, the sensor electrodes should have large area, A, and low offset gap, d.

3.5.2 Sensor design

3.5.2.1 Capacitive probe

The capacitive probe assembly comprises of an aluminium mount element, copper electrode guard connected to electrical ground, and a copper sensing electrode, as shown in Figure 3.26(b). The detailed drawings of the parts are presented in Appendix A in drafts number P90427b-100-0004a, P90427b-100-0006b, and P90427b-100-0005a, respectively. These elements are separated by glass pieces and glue layers, assuring the electrical insulation of the parts from each other and their relative alignment. The electrode guard is to focus the electric field from the sensor electrode onto the target electrode area. The electrically grounded target electrode is glued to the movable stage, as shown in Figure 3.2, via a 0.15 mm thick glass plate which electrically isolates the electrode from the bulk material of the stage, reducing

the ground loop and noise. To increase the accuracy of the capacitive measurement, the area of the target electrode is 35% larger than the sensing electrode [67]. The aluminum mount element posseses two horizontal pockets at each side, see Figures 3.26(a) and 3.27, to allow for the probe electrode and guard electrode wires running out from the sensor assembly. They run along these pockets, which are filled with glue for stability. If a large force is applied to the sensor cable, the layer of glue will take the force and in the worst case scenario, the cable will brake outside of the pocket, yet not inside of the sensor assembly, which would require a tedious dissasembly, re-soldering, and re-assembly of the entire sensor.

3.5.2.2 Sensor mount

The capacitive sensor is integrated in the positioning stage as indicated in Figure 3.2 and 3.27. The capacitive probe is bolted in between two sensor mount brackets by four M2 screws, as shown in Figure 3.1 and 3.27. The M2 bolts run through clearance holes in the middle section of the brackets and are fixed into threaded holes in the sensor assembly mount element. The detailed drawings of the metrology brackets are included in Appendix A in drafts number P90427b-100-0002b and P90427b-100-0003b. The brackets are also bolted to the structural frame by four M3 bolts, forming a metrology frame. One of the brackets has four M3 clearance holes, while the other has four M3 holes threaded. The M3 bolts run through the clearance holes of the first bracket, clearance holes in the structural stage frame, and finally, the threaded holes in the second bracket, as shown in Figure 3.1. The assembly of the brackets in the stage is accomplished by a preload force they exert on the stage structural frame, which yields a friction force providing connection. The clearance holes in the structural stage frame are designed to accommodate for precise adjustment of the sensing gap. The adjustment gap is determined with a filler gauge of a well defined thickness, which is inserted between the target electrode and a sensing electrode in order to provide a distance reference. When the desired sensing gap is achieved, the metrology mounting brackets are bolted to the structural frame. The hand adjustment with the filler gage allows for adjusting of the nominal gap, h_0, with an error of 10 μm which is more precise than the stack of achievable manufacturing tolerances of all elements influencing the gap. The nominal gap h_0 is equal to 50 μm. The sensor noise level was estimated using Equation (3.56) while designing the nominal gap h_0. The sensing gap $h_0' = h_0 + \Delta h_0$ was assumed in order to estimate the highest possible noise level, which is equal to 0.164 nm. When assembling the sensor and the metrology brackets into the stage, it may occur that the clearance between the brackets is much larger than the size of the sensor assembly which would result in a reduced contact interface between the metrology frame components. Applying a layer of glue would improve the contact interface between the sensor assembly and the holding metrology brackets, however this brings up a potential problem with disassembling of the metrology frame due to the glue layer present between the parts and no virtual access to this interface. Therefore, an additional M2 threaded hole in the centre of each of the metrology brackets is provided and can be used to twist M2 bolts into the metrology bracket and hence push on the sensor assembly while pulling the metrology brackets away from the sensor, so the glue layer can be broken and the parts separate. The metrology frame is rigidly

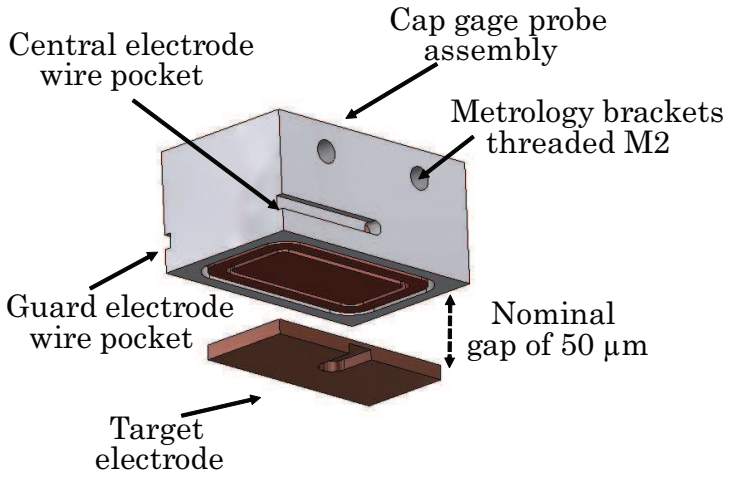

(a) Capacitive sensor probe and target electrode.

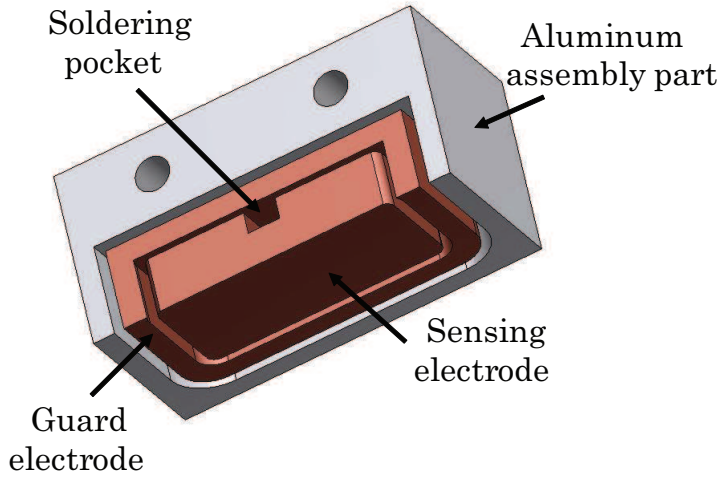

(b) Capacitive probe assembly - sectional view.

Figure 3.26: Capacitive sensor.

connected to the structural force frame. The static forces transmitted from the piezoelectric actuator into the force frame are small (5 N). These forces cause negligible deformation of the

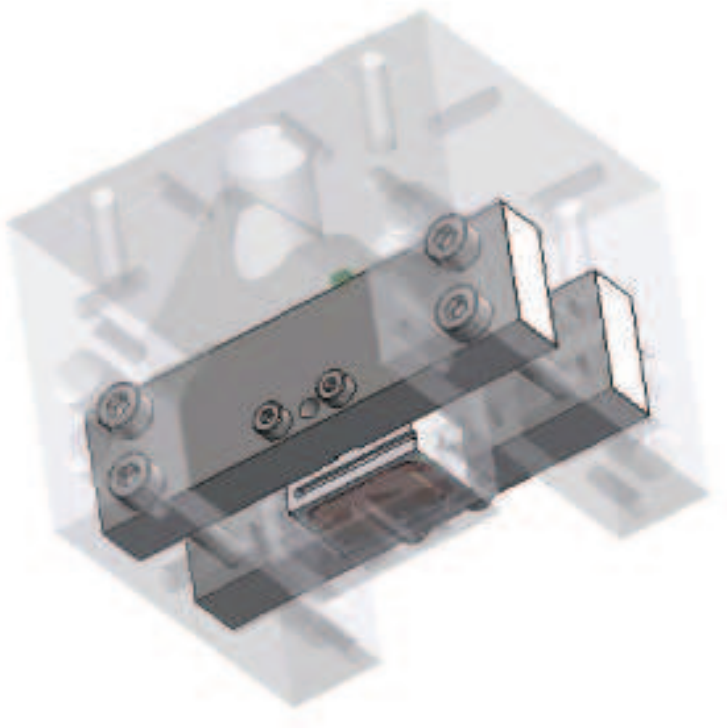

Figure 3.27: Metrology frame.

force frame and do not influence the metrology frame. In addition, the static frame deformation may be corrected by a static stage calibration. The piezoelectric actuator must additionally provide forces necessary to achieve certain acceleration profiles of the stage. These forces are frequency dependent and can not be calibrated out from the measurement. The maximum dynamic force, F_{dmax}, (5.2 N) exerted on the structural frame results in a reaction moment of the structural frame which is transferred onto metrology frame brackets. The deformation of the brackets due to their bending was analytically approximated and is negligible. Lastly, a stiff connection between the metrology frame and the structural frame of the stage provides a high stiffness against squeeze film damping forces, described later.

3.5.2.3 Sensor electronics

The demodulation circuit for the capacitive sensor used in the setup is shown in Figure 3.28 and is formed by the commercial modules from Sens Tech [1]. The following passage describes the demodulation principle and its realisation in the positioning system described in this research.

The capacitive sensing demodulation circuit is based on a transformer bridge capacitive readout circuit, shown in Figure 3.28(a). It comprises a variable capacitance, C_v, formed by the sensor probe and the target electrode, and the reference capacitor, C_{ref}, of a capacitance value closely matched to the nominal capacitance, C_v. The reference capacitor, C_{ref}, is realised by a fine adjusted ultra precision variable capacitor with a 0.02 pF resolution. An AC voltage, generated by the internal oscillator, is fed to the capacitors C_v and C_{ref} via a transformer, so that the voltage across C_v is 180° out of phase with respect to the voltage across C_{ref}. The

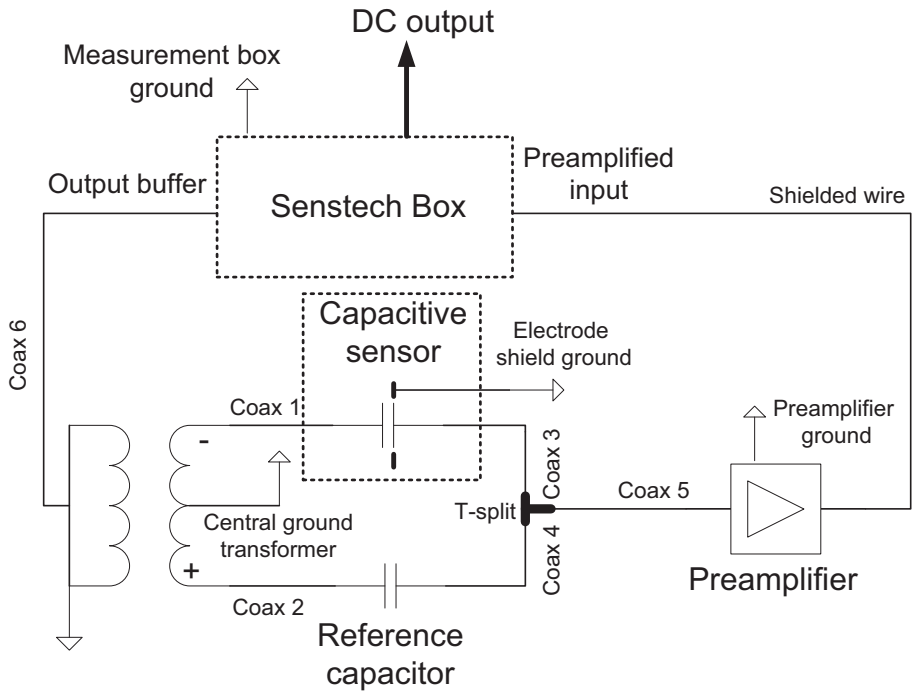

(a) Layout of the capacitance measurement setup connection to the sensor.

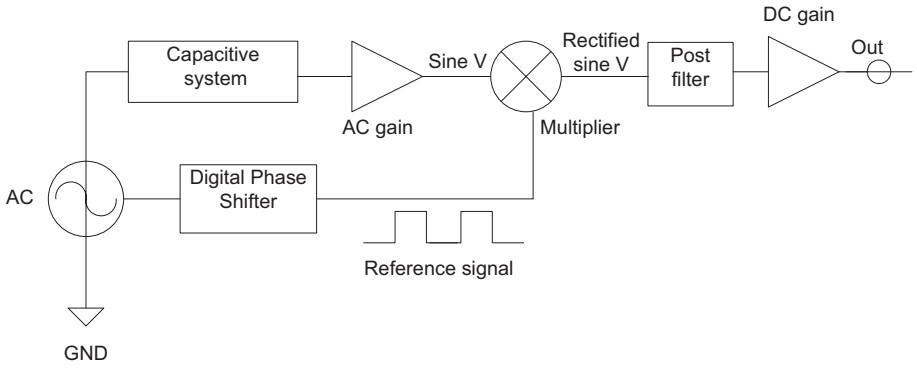

(b) Schematic of capacitance meter [1].

Figure 3.28: Capacitive sensor demodulation electronics.

voltage outputs at C_v and C_{ref} are tied together at a T-BNC split and transferred to a pre-amplifier. If the capacitances C_v and C_{ref} are equal, their output voltage amplitudes are equal and the output of the bridge is null, which means that the reference capacitor, C_v, balances the bridge. If C_v varies, the phase of the sinusoidal voltage across C_v varies accordingly, hence the tied bridge output signal changes its peak to peak amplitude, as the voltages across C_v and C_{ref} are summed. The measure of the variable capacitance change is reflected by a change in the amplitude of the bridge output signal. This signal is further amplified and passed to the synchronous detector, depicted schematically in Figure 3.28(b). The amplitude modulated signal from the bridge output and the pre-amplifier is multiplied by a square wave reference signal, with -1 and 1 peak values, which is derived from the same oscillator as the sine wave. The multiplier output is a rectified sine wave which, after low pass filtering, is transformed into a DC sensor output [1]. The digital phase shifter module, see Figure 3.28(b), can be used

to adjust the reference signal phase, so that the maximum DC component output is obtained [1]. The largest DC output is achieved when the amplitude modulated voltage signal is 0° or 180° with respect to the reference signal. When these signals are 90° or 270° out of phase the ideal output is zero [1]. There are several important remarks on how the capacitance measurement setup was implemented in practice. As one can see in Figure 3.28(a), there is a number of elements, that need to be connected to the electrical ground. Since the transformer primary winding is internally connected to the transformer central ground, all the ground connections were connected to the transformer central ground instead of at the capacitance meter central ground. In this way, the grounding loops are eliminated. Moreover, the complete stage assembly was connected to the central transformer ground, which improved the signal to noise ratio of the sensor. In addition, the coaxial cable pairs: 'coax 1', 'coax 2' and 'coax4', 'coax5', see Figure 3.28(a), were chosen as short as possible and of equal lengths. The capacitance measurement system was successfully implemented into the positioning stage. The noise floor of the sensor was measured and corresponds to the 0.7 nm error. The picture of demodulation setup connected to the stage is shown in Figure 3.29.

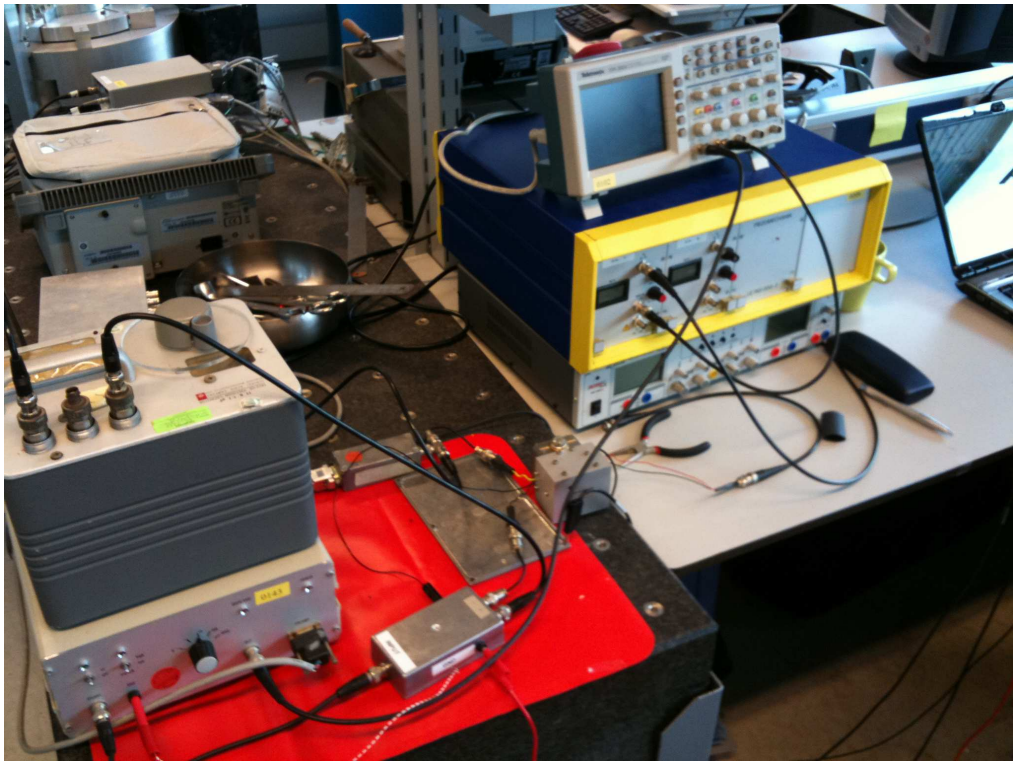

Figure 3.29: Capacitive sensor demodulation electronics setup.

3.5.3 Squeeze film damping

There is a damping force acting on the movable, closely spaced electrodes of the sensor, caused by a squeeze film damping effect. The damping forces deform the sensor electrodes and introduce a measurement error. The following Section describes the squeeze film air damping phenomenon and its importance in context of the capacitive sensor used. Squeeze film air

damping effect can be explained on an example of a pair of identical rectangular parallel plates of dimensions a and b. The plates are overlapping each other and are separated by a thin air layer of thickness, h. The plates are moving relative to each other along the direction perpendicular to their faces, so that the air gap, h varies harmonically about the nominal value, h_0, with an amplitude, δ_h, and radial frequency, ω. As the plates approach each other, the gap is decreased and the damping pressure builds between them [68]. This pressure has two components of different physical origins. The first pressure component, p_{d_v}, causes the viscous flow of medium, when the air is squeezed out of the plate area [68]. The second pressure component, p_{d_e}, causes the compression of the air trapped in between the plates [68]. The pressure yields the resistance force, which opposes the plates movement. The local pressure $p(x,y,t)$ within the gap between two plates is characterized by Reynold's equation by [69]

$$\nabla\left(\frac{h^3}{12\mu}p^{\frac{1}{\eta}}\nabla p\right)=\frac{\partial}{\partial t}\left(hp^{\frac{1}{\eta}}\right), \tag{3.57}$$

where μ is the fluid viscosity. In case of two thermally conductive plates, an isothermal process is assumed and η in Equation (3.57) is 1. For a small perturbation, δp, of local (atmospheric) pressure, P_a, ($p=P_a+\delta p$) and a small perturbation, δh, of the nominal gap spacing, ($h=h_0+\delta h$), Equation (3.57) can be linearised into [69]

$$\nabla^2-\alpha^2\frac{\partial\left(\frac{\delta p}{P_a}\right)}{\partial t}=\alpha^2\rho\frac{\partial\left(\frac{\delta h}{h_0}\right)}{\partial t}, \tag{3.58}$$

where

$$\alpha^2=\frac{12\mu}{\eta h_0^2 P_a}, \tag{3.59}$$

and α is a constant. Solving Equation (3.58) yields the pressure profile. Integrating this result over the plate area gives the damping force, F_d which, analogous to the pressure causing it, comprises a viscous, F_{d_v}, and an elastic, F_{d_e}, force component

$$F_d=F_{d_v}+F_{d_e}. \tag{3.60}$$

Darling [69] describes a solution to Equation (3.58) for rectangular rigid plates, having the aspect ratio $\beta=a/b$, harmonically oscillating about a nominal air gap, h_0, with an amplitude, δh, and radial frequency, ω. The method described there utilizes Green's function approach and treats different venting conditions along the rectangle edges. For the case of four edges vented, the acoustic pressure, p, is assumed to vanish ($p=0$). The resulting viscous and elastic force components are [69]

$$F_{d4_v}(t)=Re\left[\sum_{m,n=odd}\frac{64}{\pi^4m^2n^2}\frac{-j\sigma\eta}{j\sigma+m^2\pi^2+\beta^2n^2\pi^2}\frac{\delta h}{h_0}abP_ae^{j\omega t}\right], \tag{3.61}$$

$$F_{d4_e}(t)=Im\left[\sum_{m,n=odd}\frac{64}{\pi^4m^2n^2}\frac{-j\sigma\eta}{j\sigma+m^2\pi^2+\beta^2n^2\pi^2}\frac{\delta h}{h_0}abP_ae^{j\omega t}\right], \tag{3.62}$$

where k_{mn} are the eigenvalues of the two-dimensional scalar Helmholtz equation [69]

$$k_{mn}^2 = \frac{m^2\pi^2}{a^2} + \frac{n^2\pi^2}{b^2}, \tag{3.63}$$

and σ is the squeeze number [69]

$$\sigma = \frac{12\mu a^2\omega}{\eta h_0^2 P_a}. \tag{3.64}$$

In the case of two opposite closed edges along the length b, the boundary condition of $\frac{\partial p}{\partial t} = 0$ leads to the solution of one dimensional problem, where pressure varies only along one direction parallel to edge b. Resulting expressions for damping forces, $F_{d_v}(t)$ and $F_{d_e}(t)$, are [69]

$$F_{2d_v}(t) = Re\left[\sum_{n=odd} \frac{8}{\pi^2 n^2} \frac{-j\omega\eta\frac{\delta h}{h_0}}{j\omega + \frac{k_n^2}{\alpha^2}} e^{j\omega t}\right], \tag{3.65}$$

$$F_{d2_e}(t) = Im\left[\sum_{n=odd} \frac{8}{\pi^2 n^2} \frac{-j\omega\eta\frac{\delta h}{h_0}}{j\omega + \frac{k_n^2}{\alpha^2}} e^{j\omega t}\right], \tag{3.66}$$

where

$$k_n = \frac{n^2\pi^2}{b^2}. \tag{3.67}$$

The squeeze film air damping forces can be seen as additional damping and stiffness contributions in the the dynamic system. The stiffness introduced by the squeeze film air damping is expressed by [68]

$$k_d = \frac{F_{d_e}}{\delta h}. \tag{3.68}$$

The damping factor introduced by the squeeze film air damping phenomenon is defined as follows [68]

$$c_d = \frac{F_{d_{visc}}}{\delta h \omega}. \tag{3.69}$$

It has been shown, that these additional stiffness and damping components may significantly change the system dynamic behavior [68]. Squeeze film air damping is very often characterized by means of the dimensionless squeeze number, σ, described in Equation (3.64). The squeeze number of the plate determines the character of the damping forces. The so called critical squeeze number, σ_{cr} is the value of the squeeze number when the damping viscous force, F_{d_v} and F_{d_e}, are equal. For squeeze numbers much lower than σ_{cr}, the squeeze film air damping is predominantly caused by viscous force, whereas for squeeze numbers much higher than σ_{cr} the squeeze film air damping is caused by elastic forces [68]. Figure 3.30 shows the variation of the damping forces normalized with respect to the plate area and atmospheric pressure, as a function of squeeze number for different venting conditions. The phenomenon of squeeze film air damping was investigated when designing the capacitive sensor. Since the nominal

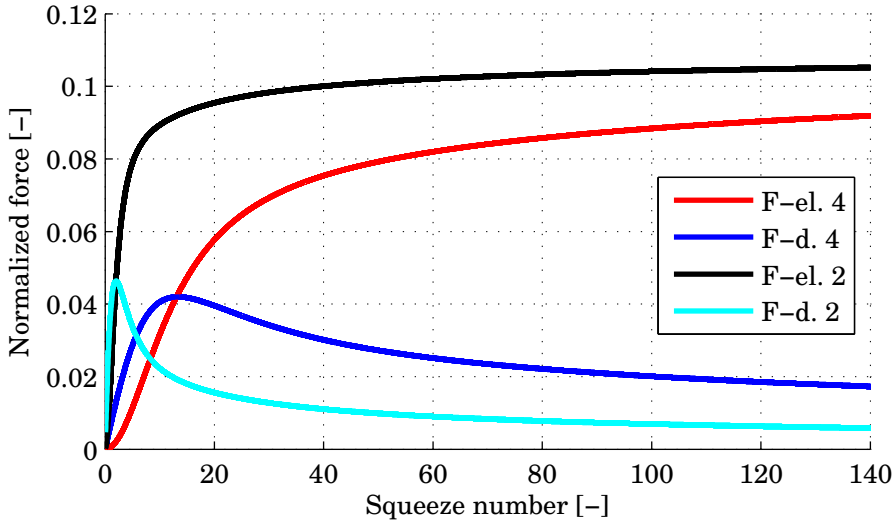

Figure 3.30: Normalized damping forces for different venting conditions versus the squeeze number.

gap between the electrodes, h_0, is approximately 55 μm and the position signals measured by the capacitor are at frequencies up to 2 kHz, the damping forces arise between the electrode plates and cause their elastic deformation, which in turn introduces a measurement error of the capacitive gage. The longer edges of electrodes are vented. However the shorter edges are blocked by the faces of the movable stage frame. This is the motivation to calculate the damping forces for both four vented edges and two vented edges conditions. The investigated plate is 14.8 mm by 6.6 mm, the amplitude of oscillation is 5 μm and the oscillation radial frequency is 1.2566 $\cdot 10^4$ rad/s. The nominal gap between plates, including the adjustment tolerance, is assumed between 50 μm and 60 μm due to a relatively large uncertainty in the sensing gap adjustment. Plates are made of copper and hence are assumed thermally conductive, which approximates the solution of air pressure to an isothermal condition and consequently, η is 1. The models used are developed for the two plated of the same dimensions. In this research, the probe electrode assembly is of considerably larger cross section (17 mm and 11 mm) than the target electrode. It is difficult to model the scenario of different plate areas, hence the calculations which follow include two idealized cases. First one assumes two plates of target electrode. The second assumes the plates to be the size of the probe electrode assembly. It is therefore assumed that the relevant model lies within the bounds specified by these two scenarios. Using Equation (3.64), the squeeze number of the system was calculated and is equal to 0.1132. Table 3.4 list the results of the squeeze film damping analysis. The table shows calculations for two and four vented edges boundary conditions. Each result is given in an interval spanned by the cases of different areas of plates assumed. It follows from the results that the calculated values are much larger for the 2 vented edges case with large plates area assumed. The thin squeeze film damping was also modelled and solved in FEM software. The simulated total damping force values, damping and stiffness coefficients for two different venting conditions agreed within 2% with the analitical solution presented earlier in this section. Figures 3.31(a) and 3.31(b) present the pressure distribution obtained via the finite element

Table 3.4: Summary of the squeeze film damping.

Characteristic	Unit	2 edges vented	4 edges vented
Dimensional damping constant	[Ns/m]	0.63 - 3.2	0.45 - 1.9
Dimensional stiffness	[N/m]	290 - 387	103 - 162
Maximal damping force	[N]	0.0297 - 0.1486	0.0214 - 0.0903
Maximal elastic force	[N]	0.0009 - 0.0121	0.0005 - 0.0050
Maximal dimensional force	[N]	0.0306 - 0.1607	0 0.022 - 0.0953
Maximal sensor deformation	[nm]	0.05 - 0.4	0.07 - 0.2

simulation. The model assumes a rigid connection between sensor mounting brackets and the

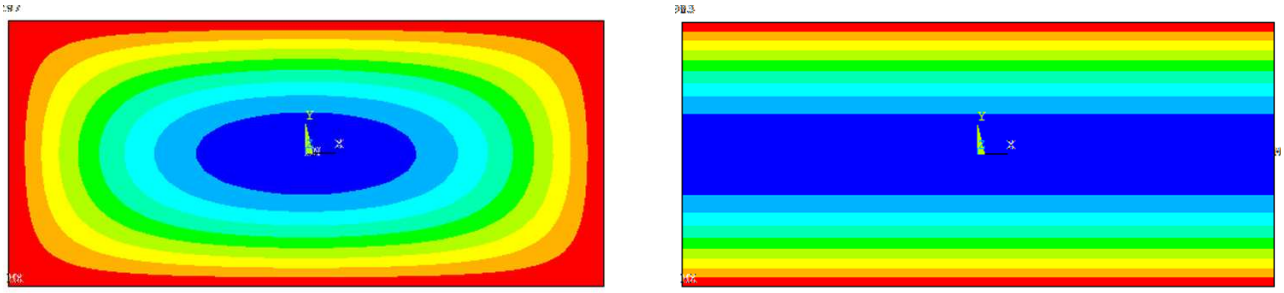

(a) Four edges vented (dark blue = maximal pressure, red = zero pressure).

(b) Two edges vented (dark blue = maximal pressure, red = zero pressure).

Figure 3.31: Pressure distribution for different boundary conditions.

stage. The deformation resulting from damping forces consists of electrode bending and the sensor mount brackets torsion. The stiffness of the metrology system against a squeeze damping force, $K_{metrology}$, can be expressed as the ratio of maximum electrode deformation and the squeeze damping force. It was assumed that the effective displacement of the electrode is equal to the half of the maximal deformation of the electrode plate. The calculated stiffness is thus twice the value calculated with FEM, which is $4.26 \cdot 10^8$ N/m. This stiffness value indicates potential deformation of the sensor due to a certain damping force. The maximum deformation of the sensor due to the damping force corresponds to the model of 2 vented edges with the large plate areas assumed and is 0.4 nm. It is important that the damping frequency forces are frequency dependent, which eliminates the possibility of calibrating their effects on the measurement system. Moreover, the objectives of low capacitive sensor noise and low level of squeeze damping force are conflicting. The sensor dimensions and offset gap were designed for an optimized value of acceptable damping force and noise level. The MATLAB optimization toolbox was used to find an optimized design.

3.5.4 Sensor calibration

The capacitive sensor gives a voltage output depending on the target displacement. This voltage is difficult to be transformed into the actual displacement because the limited knowledge

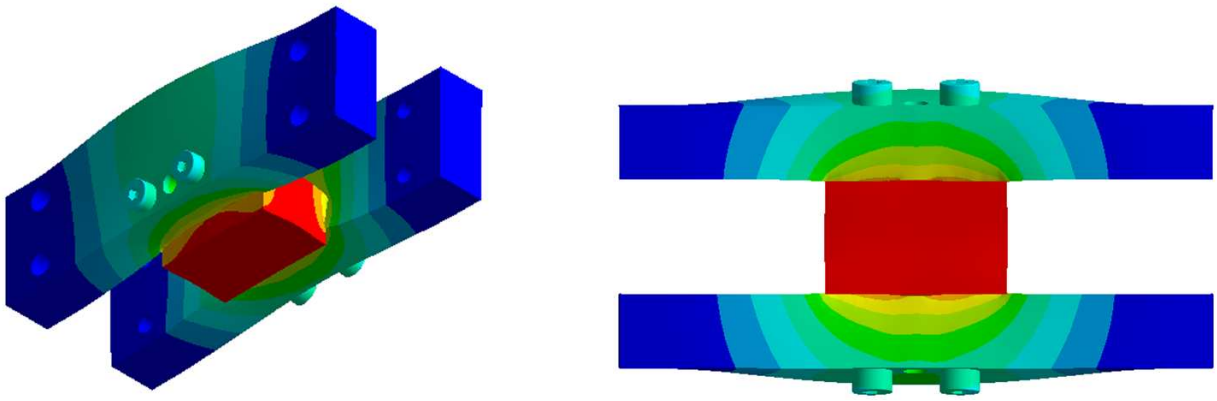

(a) Isometric view (dark blue = 0 nm, red = 0.03 nm). (b) Bottom view (dark blue = 0 nm, red = 0.03 nm).

Figure 3.32: Metrology structure stiffness FEM simulation.

of the capacitive probe parameters and the demodulation circuit gains. This was the motivation to calibrate the sensor by an external reference instrument. This has been performed by a laser interferometer, capable of measuring displacements with the resolution better than 0.2 nm and the uncertainty below 1 nm for this setup. The experimental setup is shown in Figure 3.33. A thin silicon reflective wafer was glued to the stage bottom face ‘d‘ as visible in Figure 3.33. This was necessary to obtain a high quality laser beam coming back to the interferometer. An open loop sawtooth signal of 0.1 Hz frequency was generated and sent via dSPACE to the piezoelectric amplifier and the laser interferometer was measuring the resulting stage displacement. The readings of the capacitive sensor and the laser interferometer are plotted versus each other in Figure 3.34. It shows an approximately 5 μm motion amplitude. The anticipated sensor output non-linearity is visible. A second order polynomial fit was determined to express the stage displacement, δz, in nm as the function of sensor voltage, V_c, in V. The polynomial with the truncated offset term (1776.5) is

$$\delta z = 27.3{V_c}^2 + 1433V_c. \tag{3.70}$$

The polynomial fit is also plotted in Figure 3.34. The non-linearity of the second order polynomial fit is 0.83%. Additionally, the voltage signal sent to the actuator is plotted in Figure 3.35. A linear fit was developed and is shown in the figure. The hysteresis and non-linearity present in the actuator is clearly seen in the figure. This phenomenon has been reported and studied extensively in literature [70]. They can be reduced for instance by the closed loop feedback operation or application of a charge amplifier rather than a voltage amplifier. The considerable hysteresis and non-linearity can be mitigated by applying an integrator in the feedback controller, described later.

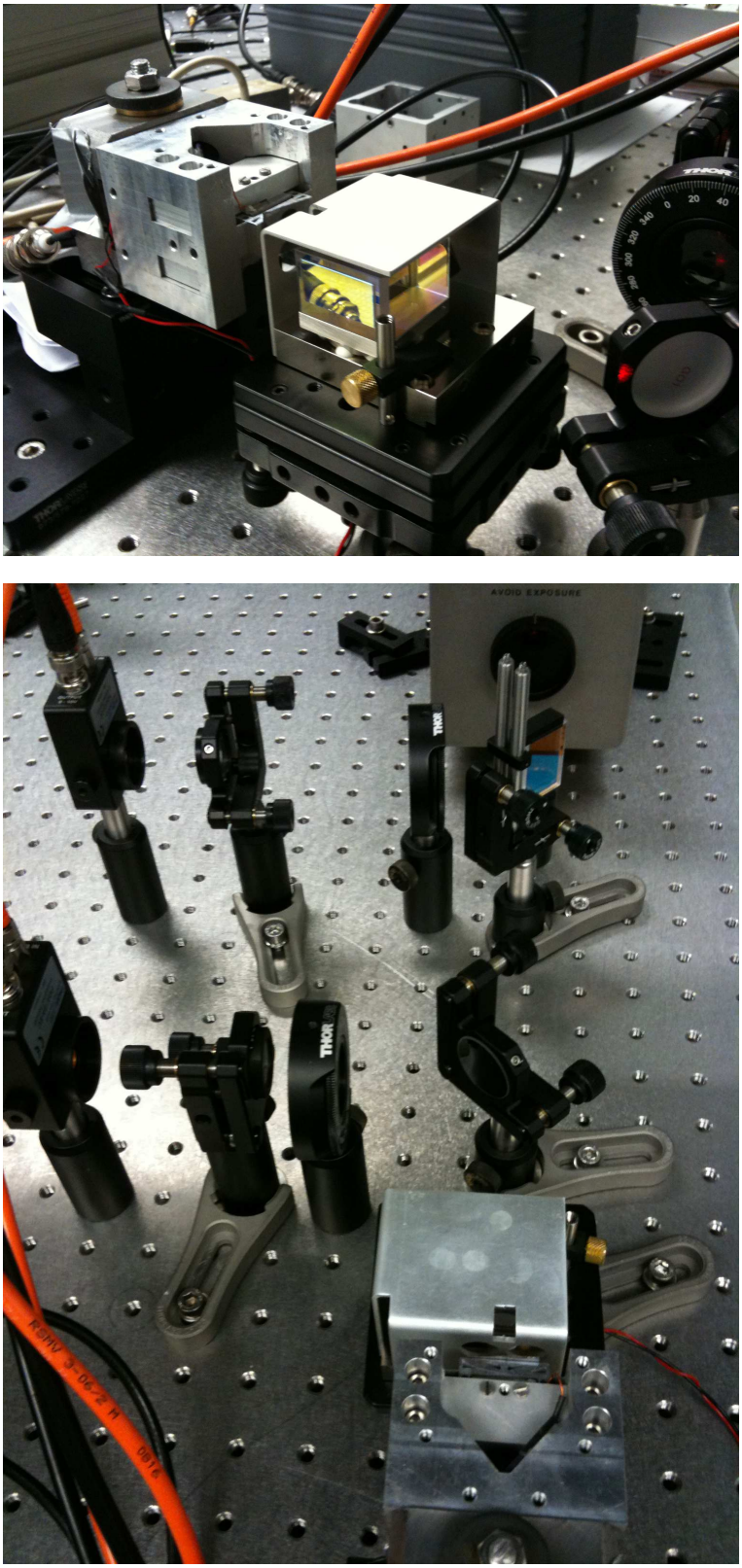

Figure 3.33: Calibration setup.

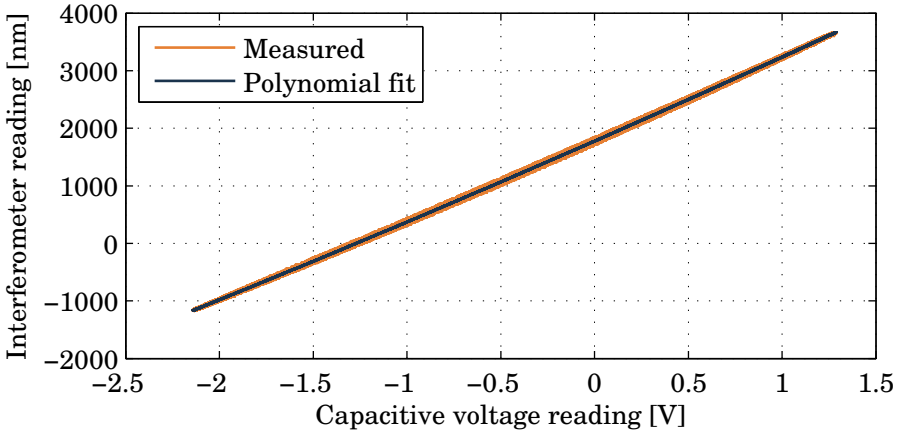

Figure 3.34: Capacitive sensor voltage versus interferometer measured displacement.

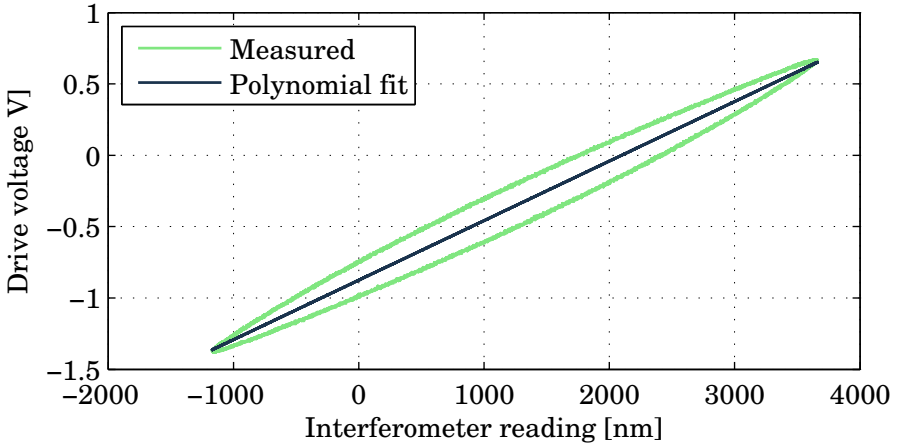

Figure 3.35: Applied voltage versus interferometer measured stage displacement.

Chapter 4

System identification and feedback controller design

The scanner dynamics needs to be identified to validate the design steps and provide the transfer functions for the feedback controller design. The scanner frequency response to the piezoelectric actuator input was experimentally measured using two different techniques. First, a laser vibrometer was used. Second, the scanner capacitive position feedback sensor was used.

4.1 Laser vibrometer experiment

A laser vibrometer was used to identify the stage frequency response at different points of stage face 'd', which yielded an information on the excited mode shapes. The reflectivity of the stage face was high enough to obtain a necessary intensity of the reflected signal, thus no additional reflective surface was used. This presents a significant advantage against an accelerometer based measurement, which introduces an additional mass to the identified system. The laser vibrometer experimental setup is shown in Figure 4.1. The scanner was rigidly attached to the T-table as shown in Figure 4.1(a). The piezoelectric actuator was stimulated by the white noise signal, provided by the SIGLAB generator, see Figure 4.1(b), and amplified by the voltage amplifier. The vibrometer laser beam was focused on the different locations of the stage bottom face 'd', see Figure 4.1(a), and both the stage displacement and velocity were measured. The experiment was performed for 9 points symmetrically distributed on the stage face 'd'. The locations of these points are described in Table 4.1. Using the nomenclature listed in Table 4.1, the measurement point shown in Figure 4.1(a) has an index 8 (bottom centre). The measurement input noise signals and displacement/velocity output signals were fed back to the SIGLAB box, see Figure 4.1(b). Based on the input output relation, the frequency responses were generated by the VNA MATLAB toolbox. The measurement data was sampled at 25.6 kHz, which limited the measurement frequency range to 10 kHz obey the Nyquist sampling criterion. Additionally, the SIGLAB excitation signal and the acquired signal were linked to each other, which synchronised the input and output channels. This means the signal generation and acquisition start and terminate at the same time instant. The input and output coherence was checked to determine the minimal excitation voltage level required for the

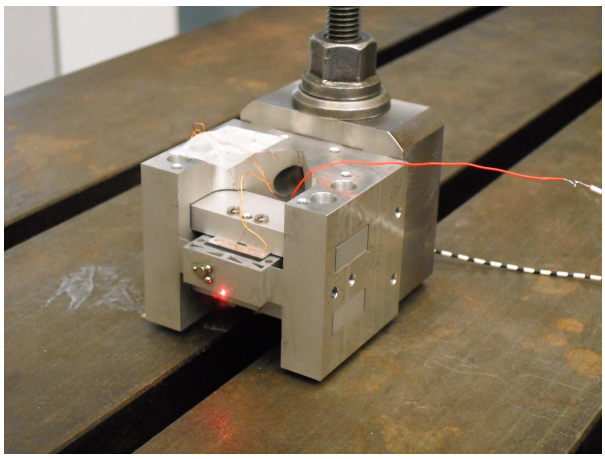

(a) Laser beam focused at the stage bottom face.

(b) Laser vibrometer.

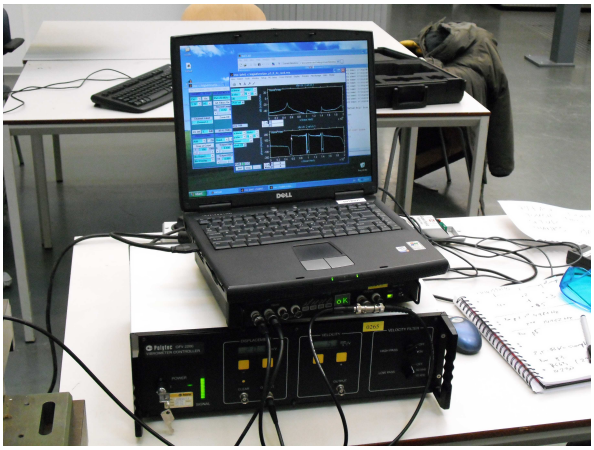

(c) 'Siglab' signal generator and vibrometer signal acquisition box.

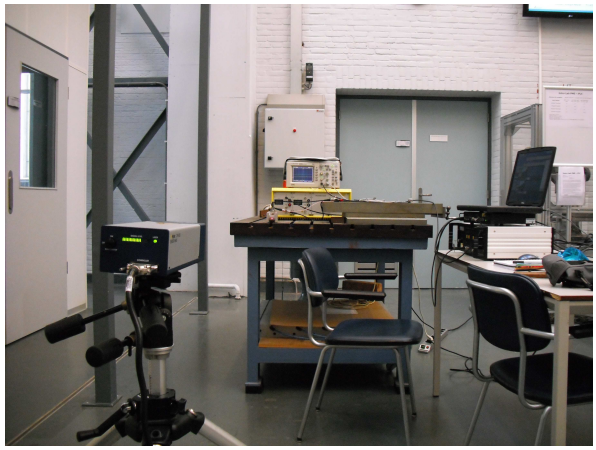

(d) Experimental setup.

Figure 4.1: Frequency response experiment using the laser vibrometer and 'Siglab' signal generator.

experiment. Special care was taken to excite the piezoelectric actuator on the lowest possible voltage level, which was a safety measure to avoid mechanical damage of the stage when excit-

Table 4.1: Laser vibrometer measurement points.

Point number	Location
1	top left
2	top centre
3	top right
4	centre left
5	stage centre
6	centre right
7	bottom left
8	bottom centre
9	bottom right

ing its natural frequencies. The SIGLAB generator was not providing a sufficiently good signal below 1 V level output, thus the amplifier gain was decreased from 15 to approximately 3. The measurements were taken over the frequency range from 1 Hz to 10 kHz and the results were averaged 200 times. The measurements were taken for both the stage assembly with the protective cover on and off. The frequency resolution of the measurement was 3.125 Hz. Figures 4.2 and 4.3 show the Bode plot of the transfer functions obtained at all 9 measurement points for the displacement and velocity output, respectively. The protective cover was assembled on the stage. The plots in Figures 4.2 and 4.3 are placed so that their relative positions in the figure correspond to the measurement points on the stage face 'd'. This means that, for instance, the central Bode plot in the figures corresponds to the measurement taken at the stage central point (5). The velocity output is related to the displacement output by the differentia-

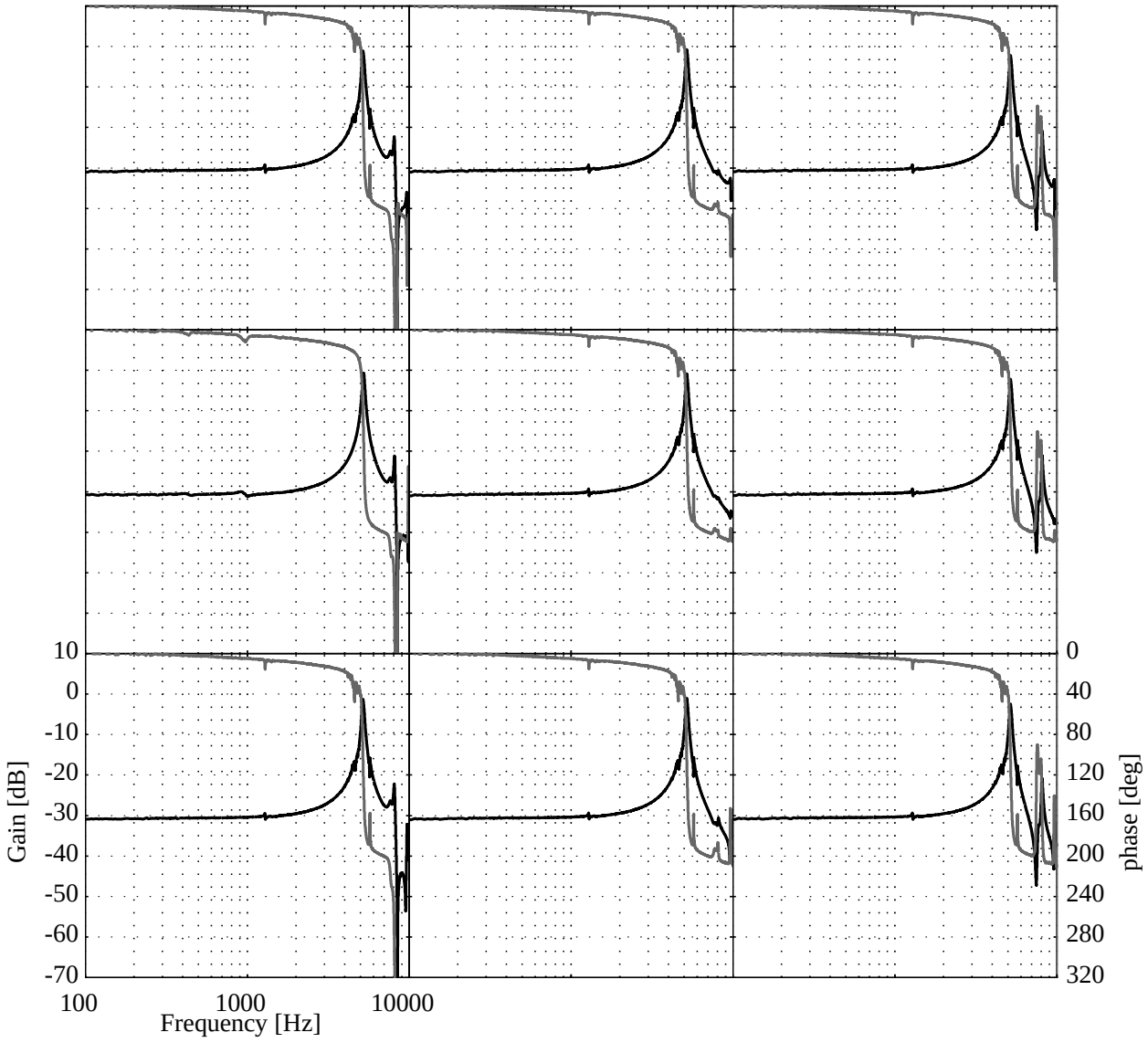

Figure 4.2: Displacement output plots with the cover attached. Black plot - amplitude plot. Grey plot - phase plot.

tion. This is visible in Figure 4.3, by an extra -10 dB/decade contribution in the amplitude plot and an extra 90° contribution in the phase plot relatively to Figure 4.2. The first natural fre-

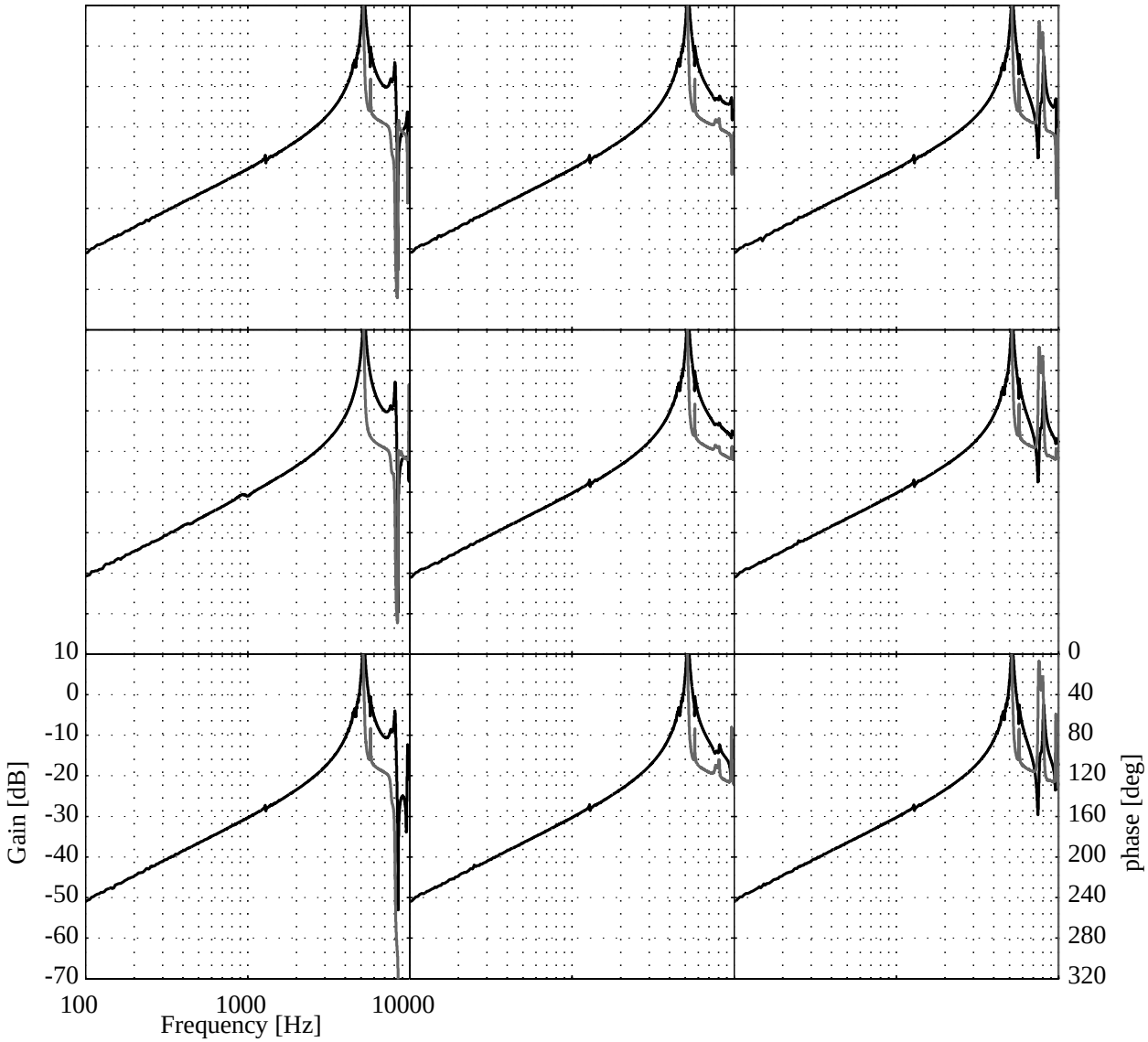

Figure 4.3: Velocity output plots with the cover attached. Black plot - amplitude plot. Grey plot - phase plot.

quency is at approximately 5.15 kHz. All 9 points show the 5.15 kHz frequency peak and this is indicating the stage rigid body mode accomplished by the leaf springs bending deformation. This eigenshape corresponds to the first eigenmode modelled in Section 3.4.9. The measured natural frequency matches the frequency predicted by Equation (3.53) (5.13 kHz) within 0.5%. This implies that the additional electromechanical stiffness of the piezoactuator is negligible for the present driving conditions. Additionally, the decrease in the actuator stiffness can be explained by the low voltage applied to the piezo and a reduced amplifier gain (10% of the nominal value). The second resonance peak is visible at approximately 8 kHz. It is observable at all measurement points except for these placed at the vertical line passing through the stage centre (points 2, 5 and 8). This motion is unobservable at these points. Additionally, a closely spaced pole zero pair at 8 kHz is indicating an out of plane, rocking motion. These two arguments imply that the mode shape excited at this frequency is the second mode described in Section 3.4.9, which is the stage rocking motion about the y-axis. The measured resonance

frequency is higher than the one predicted in Section 3.4.9 for the stage cover off (7.85 kHz). However, the modal analysis with the cover on predicted this mode shape at frequencies higher than 10 kHz. There is also a small resonant peak at 9.675 Hz. This is the third mode calculated by the FEM analysis for the cover off. The predicted mode shape was a stage rotation about the x-axis together with the torsional flexures vibrations. The measured frequency of the peak is much higher than predicted by the FEM model (8 kHz). However, the FEM model did not include the stiffening effect of the actuator for such motion, which could significantly increase the resonance frequency, similary to the increase of the first resonance frequency.

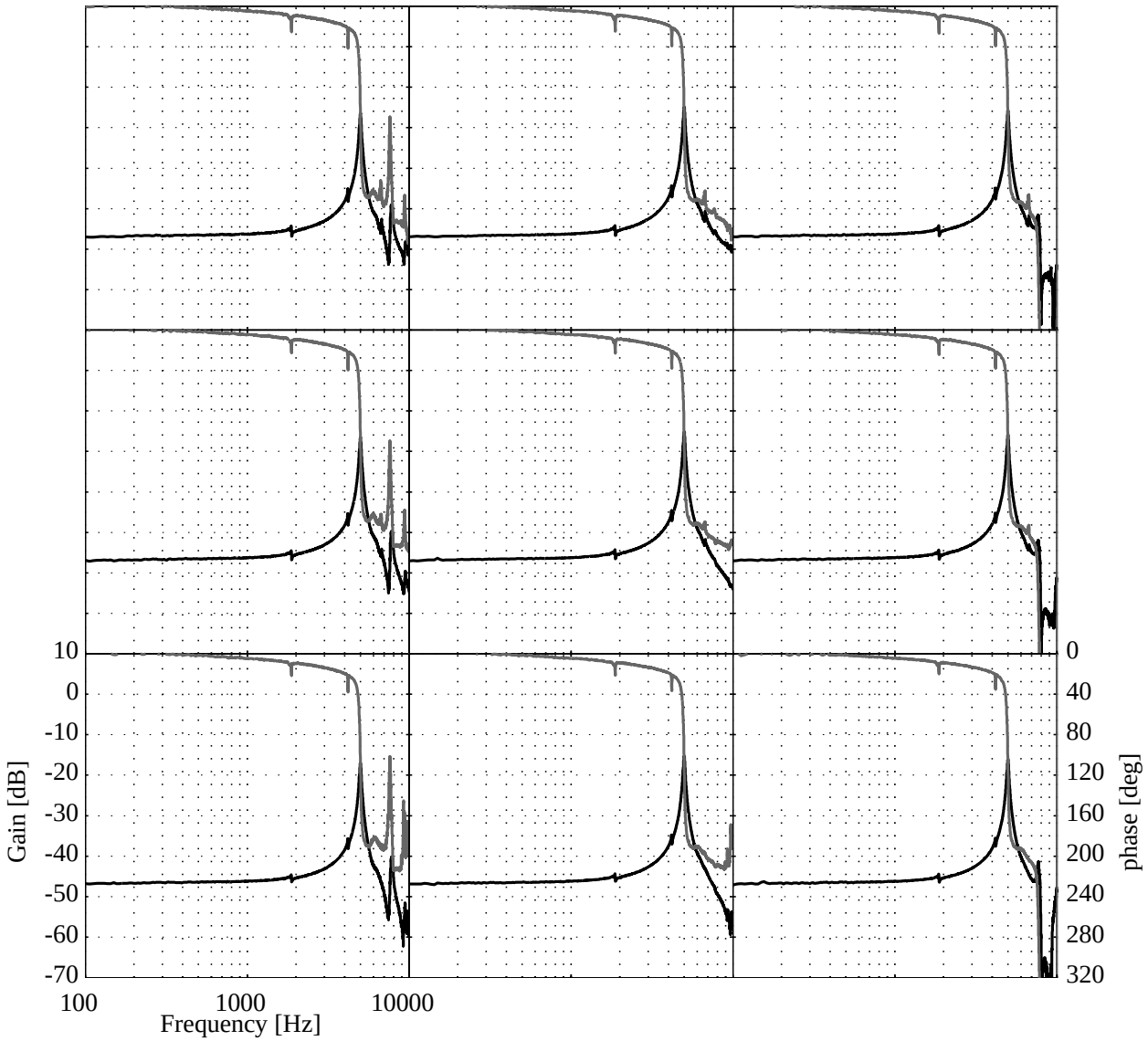

Figure 4.4: Displacement output plots without cover attached. Black plot - amplitude plot. Grey plot - phase plot.

Figure 4.4 shows the Bode plots of transfer functions obtained from the displacement output with stage cover off for all 9 measurement points. The resonances have mode shapes similar to the previous case. The first resonance frequency occurs at 5 kHz. The second resonance peak is at 7.7 kHz and matches the predicted frequency (8.85 kHz) within 2%. The third mode occures at 9.678 Hz, which is very close to the case of cover attached. Additionally, Figure 4.5

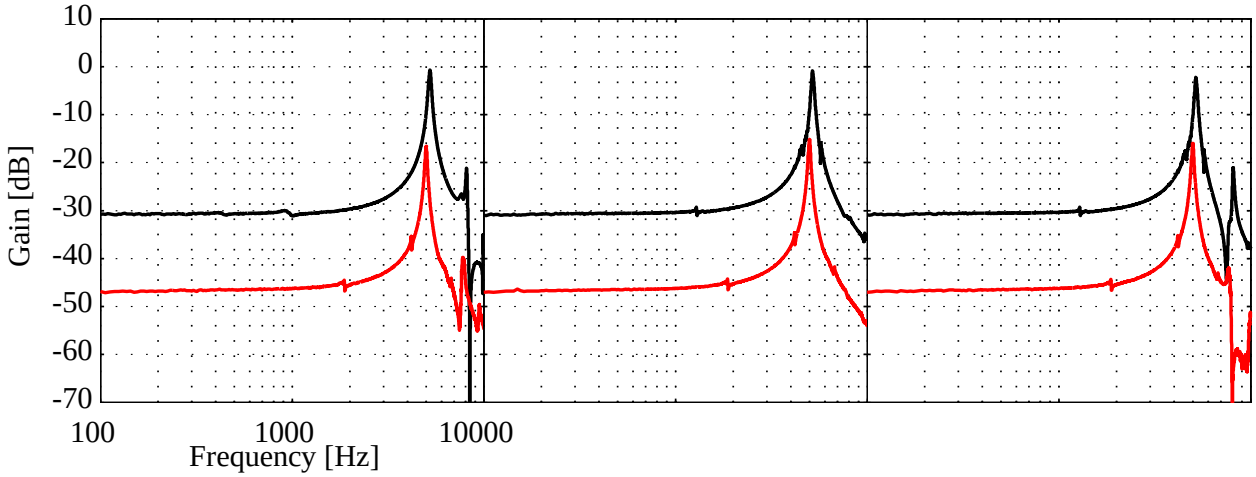

Figure 4.5: Comparison of amplitude plots for the cover attached and no cover case. Grey plot - cover attached. Red plot - no cover.

presents a comparison between the measurement results taken with the cover on and off for three different measurement points. The resonant frequencies are higher for the case with the protective cover attached. Table 4.2 shows the comparison of the two experiments.

Table 4.2: Comparison of natural frequencies with the protective cover on and off.

Resonance	Cover on [kHz]	Cover off [kHz]	FEM no cover [kHz]
1	5.18	5	5.13-6.8
2	8.1	7.7	7.85
3	9.675	9.678	8

It is clear the cover has a stiffening effect for the second resonance, where there was 5% resonance frequency increase. Similar for the first resonance where the frequency increased by 3.5%. However, there is no natural frequency increase for the third resonance visible in the frequency responce. The eigenmodes predicted by the FEM analysis showed the change in the resonant mode shapes, however the freqeuncy response experiment did not show this. In conclusion, the protective cover has a stiffening effect on the stage. Nevertheless, it is not so pronounced as modelled by FEM simulations, which were an idealised representation of sliding fit between the stage and the cover.

Figure 4.6 shows the measurements taken at three different points (point 2, point 4, and point 5), with the cover on, to compare another two cases. First, the four M4 bolts attaching the stage assembly to the T-table mechanical interface block (see Figure 4.1(a)) were bolted tight. The other experiment was performed with the M4 screws loose. The results showed that with the loose screws some of the small peaks in the area of the 5 kHz main resonant peak disappeared. This indicates, that these peaks are most probably related to the vibration of the mechanical interface between the stage and the T-table. The vibration of the cover and the block were also measured, however, no clear response could be registered due to the low excitation signal, which was not to excite these bulky structures sufficiently high for the

vibrometer sensitivity. The important conclusion from the laser vibrometer experiment is that

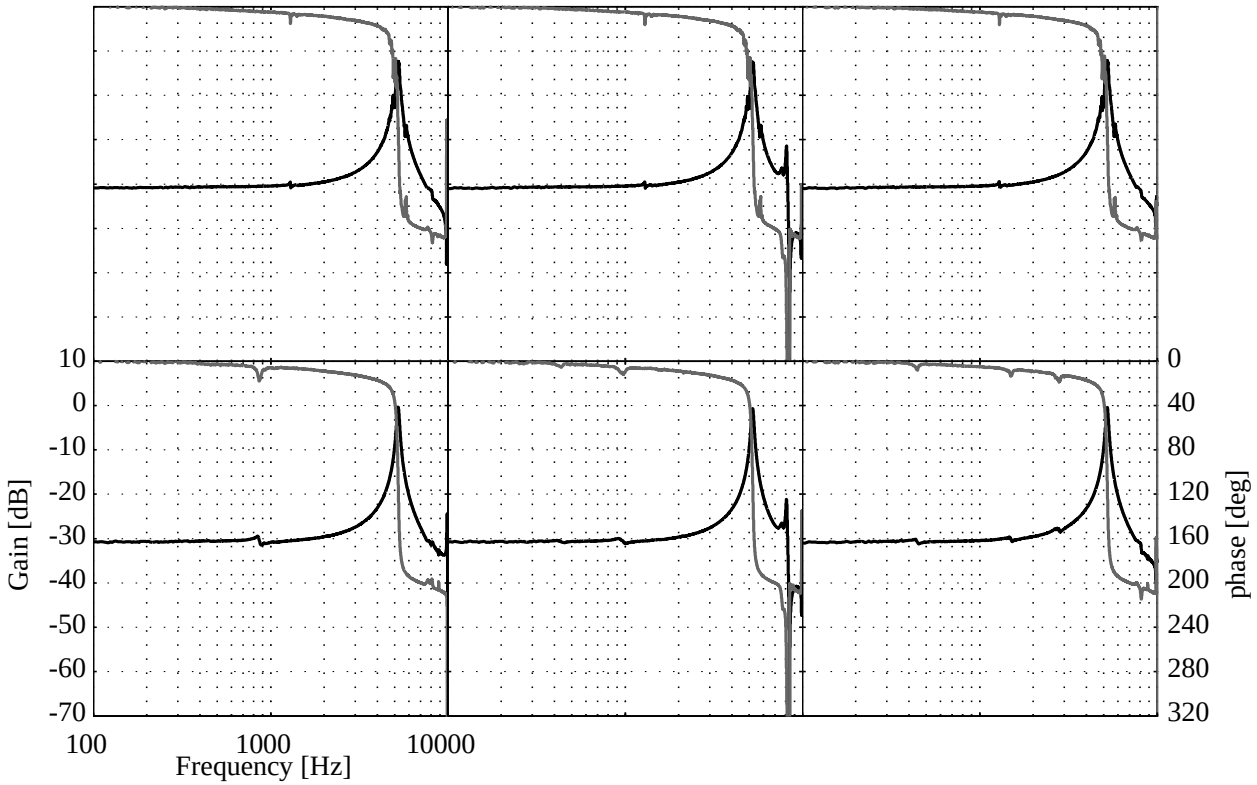

Figure 4.6: Influence of M4 bolts tightening. Plotted: point 2 tight, point 4 tight, point 5 tight, point 2 loose, point 4 loose, point 5 loose. Black plot - amplitude plot. Grey plot - phase plot.

the protective cover does not vibrate and can be used in the scanner operation. The following discussion treats the measurement data based on experiments with the cover on. The Bode plot of the stage centre point (point 5) represents a typical mass, spring, damper system transfer function. Based on the transfer functions obtained from the displacement measurement at this point, the dynamics of the scanner was identified. The damping ratio, ξ, was calculated as

$$\xi = \frac{M_{DC}}{2 \cdot 10^{G_{res}/20}}, \tag{4.1}$$

where M_{DC} is the DC gain of the transfer function and M_{res} is the resonant peak value of the Bode magnitude plot. The calculated value is 0.014. Since the dynamic mass of the stage is well known, one can estimate the stiffness of the stage following from the experiment as

$$k_m = m_{dyn}{\omega_{LV}}^2, \tag{4.2}$$

where ω_{LV} is the measured natural frequency in rad/s and m_{dyn} is the total stage dynamic mass in its first resonant mode (6.6 g). The calculated value of stiffness is 6.57 N/μm and corresponds to 53% of the expected stiffness (12.5 N/μm). From the above, the damping constant, c_d, was determined and is 5.5 Ns/m. This value is larger than the maximal squeeze film damping constant predicted in Section 3.5.3 which was 3.2 Ns/m and corresponds to 55% of the measured value. The predicted and mesured damping values are in the same order of magnitude. Additionally, are other sources of damping visible in the measurement, of which

the most significant is probably the interface between the glued piezo stacks. Using the values of m_{dyn}, k_m and ξ the transfer function of the mass, spring, damper system approximation was determined and is compared with the measurement data in Figure 4.7. The model suits well the measurement data. There is also a measurement system time delay visible in the phase plot, however it is not important for this experiment. The analysis of the stage dynam-

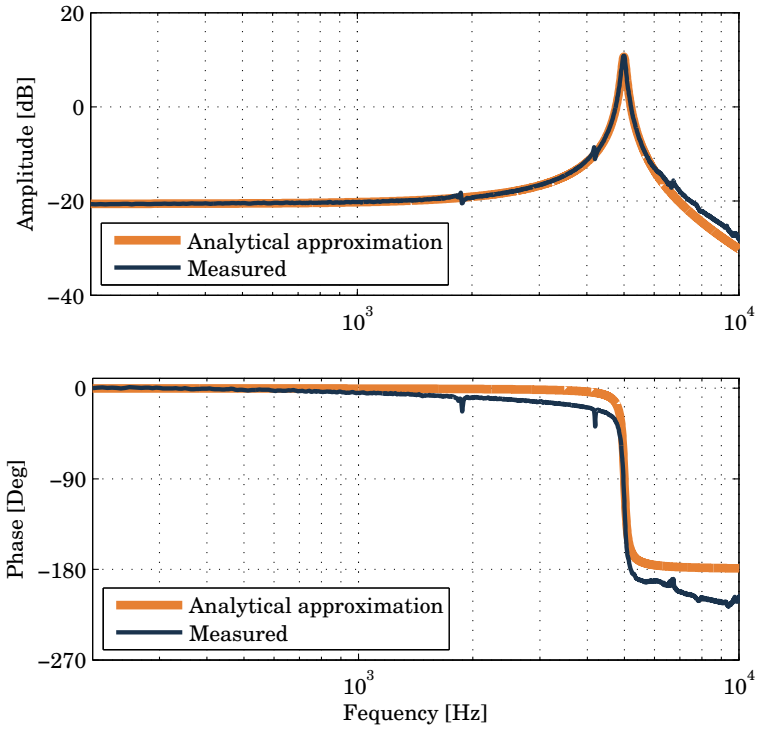

Figure 4.7: Approximation of the frequency response data by a mass, spring, damper system without phase delay.

ics with the laser vibrometer allowed identifying the main eigenmodes visible in the frequency response. The results provided a valuable knowledge on the designed system, because some of the measured resonances are not observable by the capacitive feedback sensor. The measurements showed, that the structural FEM analysis of the microscope were precise within 2% for the second resonance mode, which is not affected by the piezo stiffness and its considerable uncertainty. Moreover, it confirmed the correct design for a high second resonance mode of the structure. Lastly, the results confirmed to certain extend the stiffening properties of the sliding fit protective cover.

4.2 Multisine and sine sweep feed

Another frequency response experiment was performed by using the capacitive position feedback sensor as the stage response measurement. Two different signals were generated by the dSPACE system and sent to the stage via the voltage amplifier, a multisine signal and a sine sweep signal. The capacitive sensor output was read in the dSPACE system and the input/output data sets yielded the transfer functions. First, the multisine signal experiment

is discussed. A MATLAB custom toolbox [71] was used in this analysis. The multisine signal containing frequencies from 200 Hz to 16 kHz of 250 mV peak to peak value was sent to the stage, with the amplifier gain setting of 15. It is shown in Figure 4.8(a) and the transition between the minimum (200 Hz) and maximum (16 kHz) frequencies is visible. The output signal read by the capacitive sensor is presented in Figure 4.8(c), and the amplification of the output sweep changing in time is clearly visible. The measurement was ran for 1000 signal periods which, after averaging, improved the quality of the resulting transfer functions. The coherence of the input and output signals is presented in Figures 4.8(b) and 4.8(d), respectively. The input coherence is 1 over the whole measurement frequency range. The output spectrum drops down at discrete frequencies of approximately 5 kHz, 9 kHz, 11 kHz and 14 kHz. This coherence drop implies practically, that the output signal is not following the input signal at these particular frequency points. These frequencies are potentially the system zeros. Additionally,

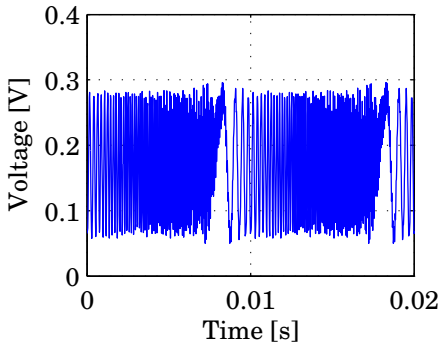

(a) Multisine voltage input signal sent by dSPACE.

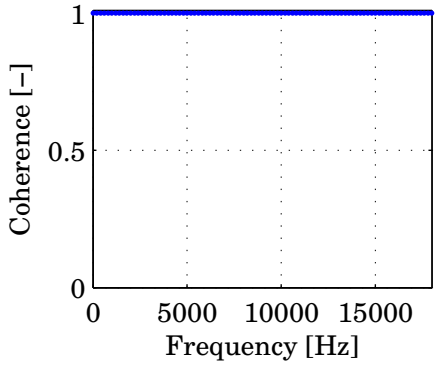

(b) Input coherence.

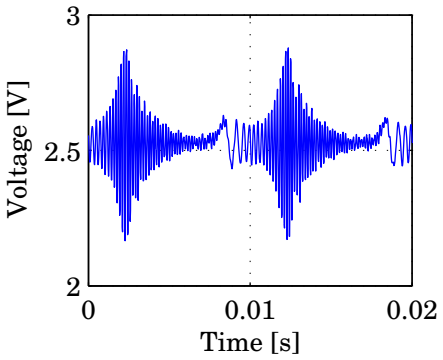

(c) Capacitive sensor voltage signal.

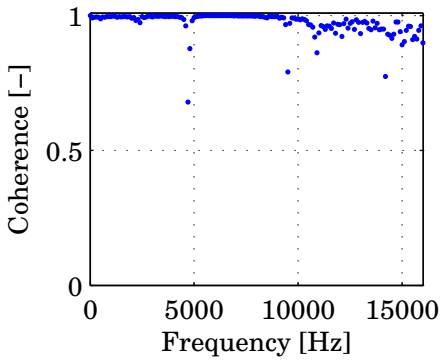

(d) Output coherence.

Figure 4.8: Time signals and their coherence.

the frequency spectra of the input and output signals are presented in Figure 4.9. The input spectrum is homogeneous throughout the measurement range, while the output frequency spectrum shows a peak value at approximately 6 kHz, which is the measured resonance frequency of the system. It is visible in the Bode plot of the transfer function obtained, shown in Figure 4.10. Another experiment was performed by sweeping a sine voltage between 200 Hz and 16 kHz of 250 mV peak to peak amplitude and reading the capacitive system position

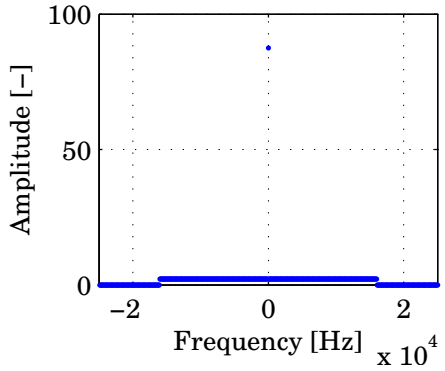

(a) Amplitude of input frequency spectrum.

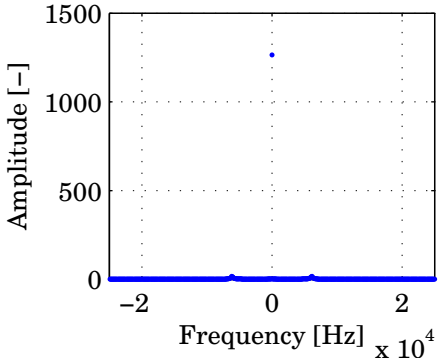

(b) Amplitude of output frequency spectrum.

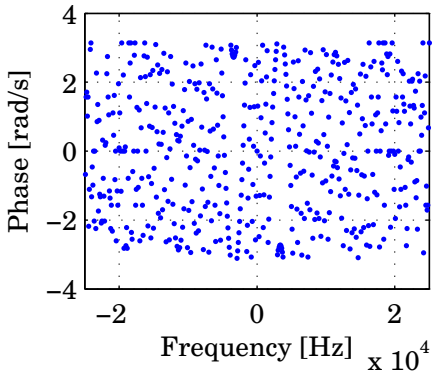

(c) Phase of input frequency spectrum.

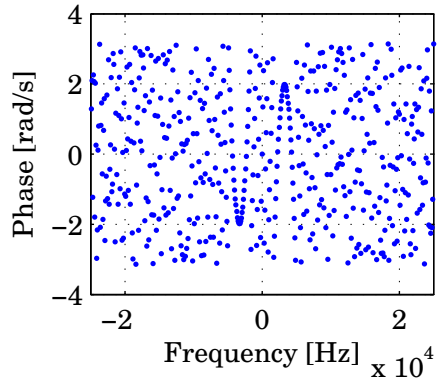

(d) Phase of output frequency spectrum.

Figure 4.9: Input and output frequency spectra.

feedback. The data was sampled at 100 kHz frequency. This method relies on the system excitation by the sine wave of the specified discrete frequency, which increases after a specified number of periods. The MATLAB code used [72] for signal generation adjusts the swept frequencies to ensure an integer number of sine waves taken, which improves the measurement accuracy [72]. The resulting transfer function is a set of averaged input output relations for each measured frequency. This type of excitation requires a considerable amount of time to run the experiment. The frequencies at which the response was measured were given in a vector of frequencies increasing logarithmically to limit the experiment time. The resulting transfer function is shown in Figure 4.10. Clearly, the results obtained by the sine sweep and the multisine input are close to each other. However, the sine sweep transfer function was based on more frequency data points and is considered to be slightly more accurate. Thus, the transfer function obtained via a sine sweep was chosen for the further discussion and modelling. Similar as before, the Bode plot from the sine sweep experiment was used to estimate the dynamic system parameters. The resonance frequency of the stage is 6.17 kHz, which is 1 kHz higher than the one obtained via laser vibrometer experiment. The stage stiffness based on this value, evaluated with Equation (4.2), is 9.9 N/μm. The estimated damping ratio, ξ, calculated using Equation (4.1) is 0.0128. The evaluated parameters lead to a mass, spring, damper system approximation shown in Figure 4.11. The figure compares this model with the measured response data and with the previously developed approximation based on the laser vibrometer

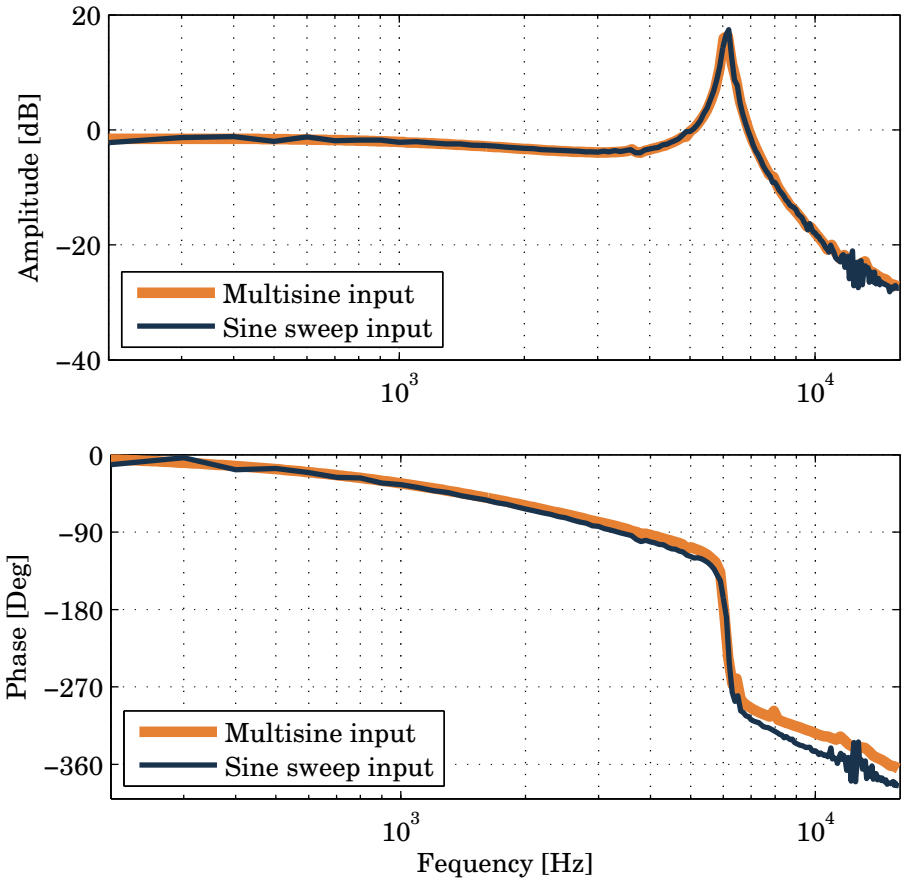

Figure 4.10: Bode plots obtained from the sine sweep and multisine inputs.

experiment. The difference between the first resonance frequencies must be caused by the variation of the actuator stiffness, since the stage mass was unchanged and is easily predictable. On the contrary, the actuator stiffness is depending on the driving conditions and the voltage levels as described in Sections 3.4.6 and 3.4.7. During the laser vibrometer experiment, the piezoelectric actuator was driven by a constant, low amplitude white noise signal. As explained above, there is most probably no additional electromechanical stiffness present for such driving condition. The dynamic stimulation signals, used in the identification by capacitive sensor, were harmonically exciting the piezoelectric actuator and there was a variable voltage built in it, even though the piezoelectric actuator has closed leads. Also the amplifier gain was higher for the latter experiment, which might influence the electromechanical piezo stiffness. From Figure 4.11 follows that the transfer function obtained via the sine sweep differs from the one fit to the one based on the laser vibrometer experiment. The magnitude plot is slightly more concave in the vicinity of the main resonant peak. Moreover, the system presents a significant time delay, approximated as

$$\theta = \frac{\omega_{90} - \omega_m}{\omega_m}, \tag{4.3}$$

where ω_{90} is the anticipated frequency of the mass-spring system at -90° phase crossing without a time delay and ω_m is the measured frequency at -90° phase. The estimated time delay, θ,

is 66 µs and was included in the model by the first order Padé approximation [73]

$$e^{-\theta s} = \frac{\frac{-\theta}{2}s + 1}{\frac{\theta}{2}s + 1}. \tag{4.4}$$

The derived models neglecting and including time delay approximation are shown in Figure

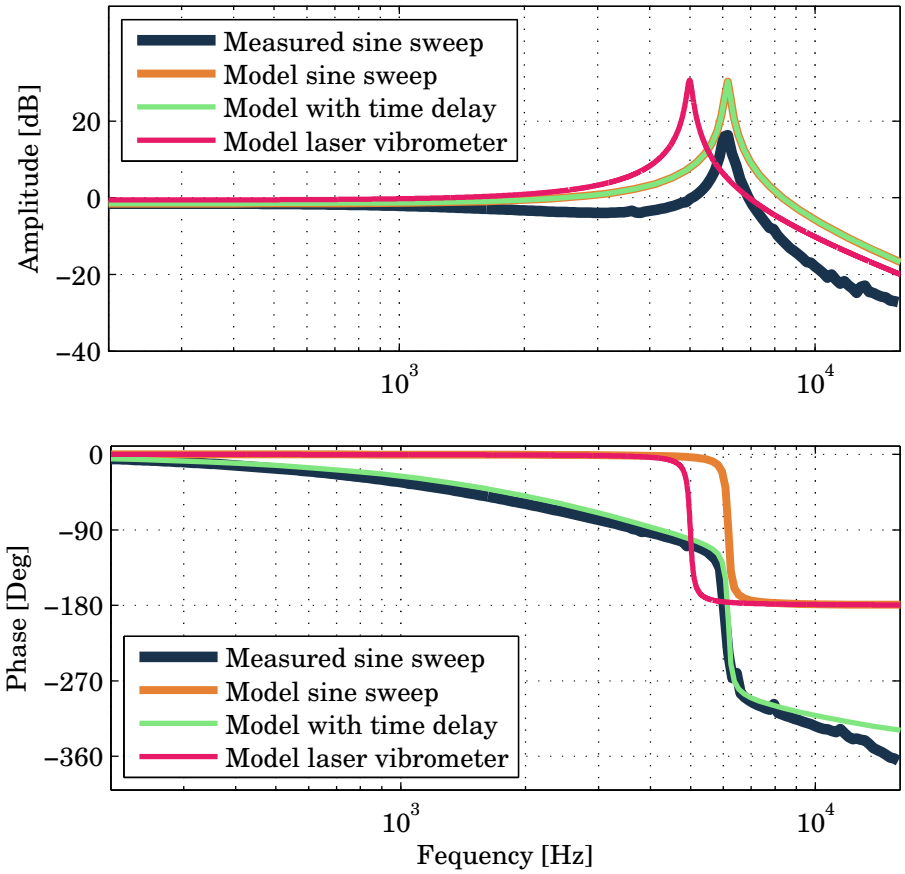

Figure 4.11: Comparison of laser vibrometer results with sine sweep results and their analytical approximations.

4.11. The phase plot of the developed model including time delay reasonably represents the measurement data. Nevertheless, the slight difference in the amplitude of the identified system was the motivation for using more complex models.

4.3 Model fit using MATLAB system identification toolbox

The MATLAB system identification toolbox was used to determine the system dynamic model. The ARX(p,z,td) function was used and it calculated different transfer functions, depending on the requested model order, which included the specified number of poles (p), zeros (z) and time delays (td). The models reasonably matching the measurement data were of significantly high orders. The retrieved models' Bode plots are summarized in Figures 4.12 and 4.13. The ARX fits presented in Figure 4.12 were obtained from the complete sets of measurement frequency

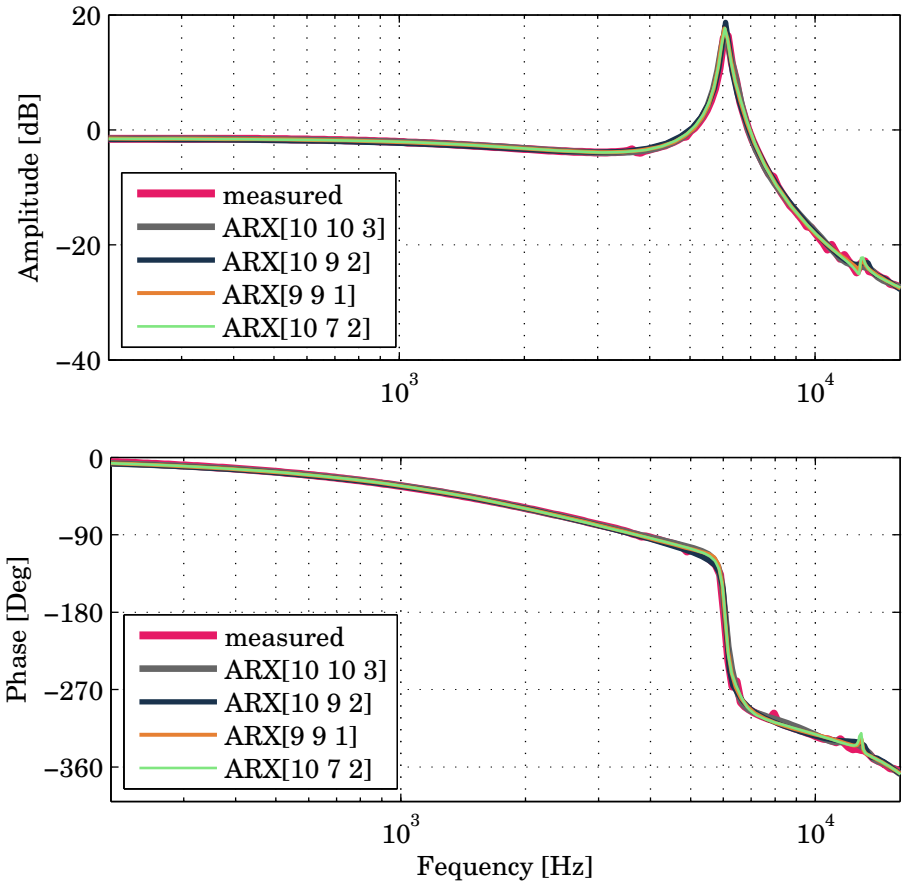

Figure 4.12: Comparison of different ARX model fits based on entire frequency data.

data, 200 Hz to 16 kHz. Models shown in Figure 4.13 are based on the truncated frequency range, 500 Hz - 10 kHz, to enhance the model at the resonant peak region. However, the truncated data models did not comprehensively represent the higher frequency roll-off regions. The ARX[10,10,3] model was found as the most suitable for the system transfer function and is plotted in Figure 4.14 together with the measurement based transfer function. The discrete transfer function of the model is

$$G = \frac{-0.01z^9 + 0.1z^8 - 0.4z^7 + 0.9z^6 - 1.4z^5 + 1.4z^4 - 1z^3 + 0.5z^2 - 0.13z + 0.02}{z^{12} - 7.8z^{11} + 28z^{10} - 63z^9 + 96z^8 - 104z^7 + 81z^6 - 44z^5 + 17z^4 - 4z^3 + 0.4z^2}, \tag{4.5}$$

at 100 kHz sampling. This model was used to design and tune the feedback controller for the scanner closed loop operation described in the next section. To summarize, it has been shown that the capacitive sensor does not observe the second and third resonances visible in the laser vibrometer experiment. The unobservability and uncontrollability of these modes may not necessarily be an issue for the controller stability, however, when approaching the higher resonance regions in may degradate the AFM measurement performance if the modes excite the stage. Yet, for the bandwidth of 2 kHz the higher resonances of the system should not impose limitations. The scanner dynamics based on the capacitive sensor position feedback is slightly different from the anticipated mass, spring, damper system characteristic. Thus, a more accurate model was developed for system modelling in the context of a feedback controller design.

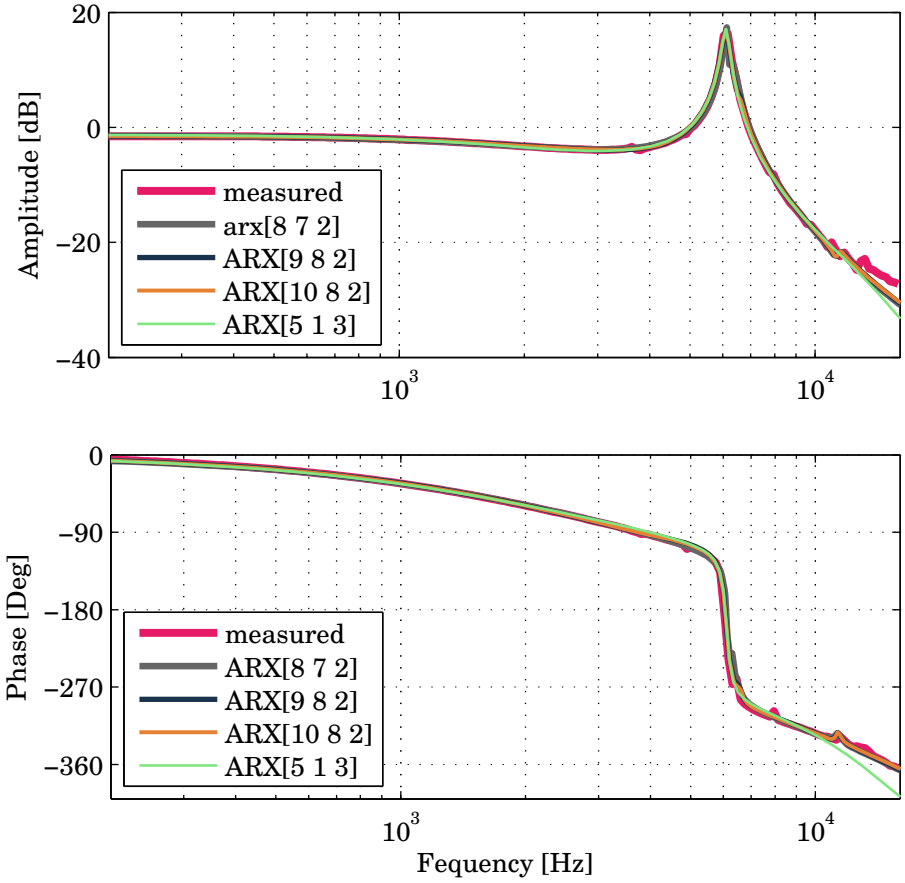

Figure 4.13: Comparison of different ARX model fits based on limited frequency data.

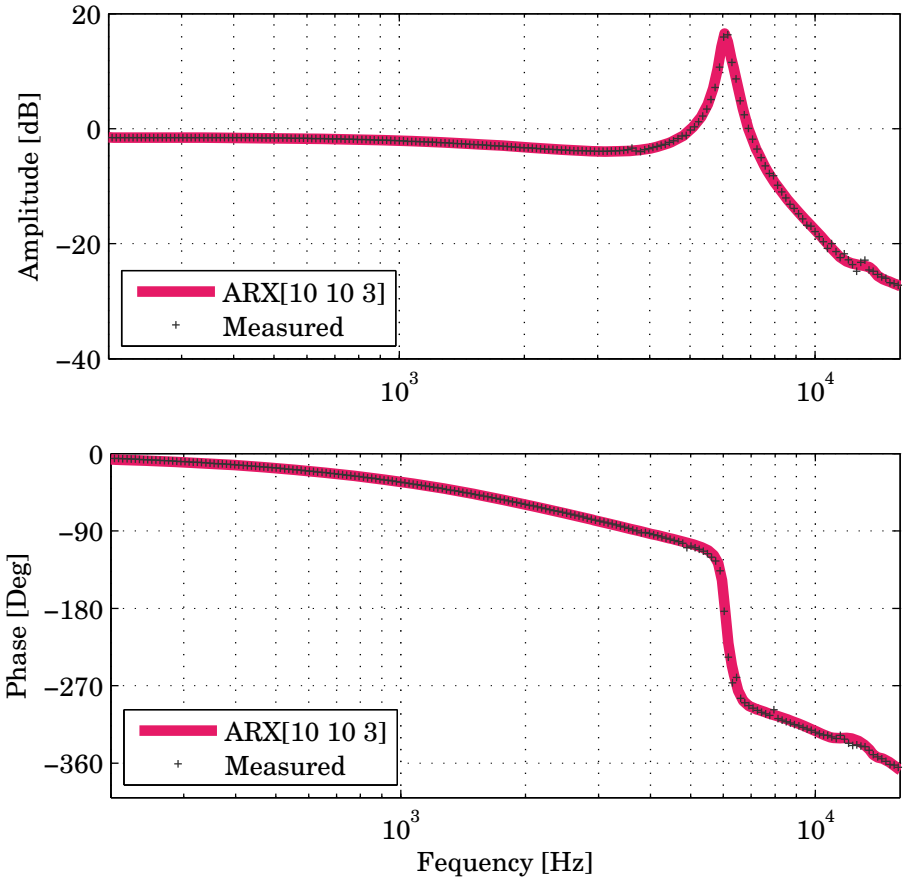

Figure 4.14: Bode plots of the measured transfer function and the ARX model chosen.

4.4 Feedback controller design

The following section describes the design of a feedback controller for the closed loop stage operation. First, the modelling of the controller is presented. Second, the controller implementation and tuning in the positioning stage are discussed. The investigated system has a limited low frequency gain due to the dominant high stiffness at the low frequencies. Applying the integrator minimizes the steady state error and increases the loop gain at lower frequencies for enhanced disturbance rejection. The designed controller is a proportional-integral (PI) controller

$$PI(s) = K\frac{s/\omega_i + 1}{s/\omega_i}, \tag{4.6}$$

with K equal to 1 and ω_i equal to 1257 rad/s. The corner frequency of the PI controller was tuned to place it as far as possible to the right, so the higher gain at low frequency is achieved without interfering with the gain in the cross over region. In addition, a notch filter was designed to attenuate the system main resonant peak. The obtained notch filter has the continuous form of

$$N(s) = \frac{{\omega_n}^2 s^{-2} + 2\beta_1 {\omega_n}^{-1} + 1}{{\omega_n}^2 s^{-2} + 2\beta_2 {\omega_n}^{-1} + 1}, \tag{4.7}$$

where β_1 is 0.1 and β_2 is 20. The ω value was adjusted so the notch filter had a notch centre at 6.1 kHz after the zero order hold discretization. The digital controller obtained via the zero order hold transformation is

$$C_d(z) = \frac{0.7z^3 - 1.897z^2 + 1.811z - 0.6016}{z^3 - 1.939z^2 + 1.019z - 0.07979}, \tag{4.8}$$

and is sampled at 100 kHz. Additionally, the digital controller Bode plot is shown in Figure 4.15. Figure 4.16 presents the open loop gain Bode plot used for the frequency tuning. The gain margin of 4 dB, phase margin of 48° and the closed loop bandwidth of 2.57 kHz follow from the figure. The proposed controller is quite aggressive, however by decreasing the gain, stability margins can be easily improved. For instance, changing the gain for 0.9 results in the gain margin of 5 dB, phase margin of 58° and the bandwidth of 2 kHz, which would still meet the design requirements. The fine adjustment was, however, performed by on-line tuning. Figure 4.17 shows the simulated closed loop Bode plot, which is the complimentary sensitivity of the system. The achieved bandwidth of approximately 2.5 kHz can be read from the plot. The complimentary sensitivity gives the measure of the scanner tracking performance, which is the given displacement input. For the AFM scanner, the tracking performance is given by the frequency modulated probe signal, maintained on the constant level. In addition to the tracking performance, AFM scanner must present sufficient disturbance rejection capabilities. In control engineering terms, the AFM topography measurement relies on rejecting the disturbance input originating from the topography inputs. In this research, such a disturbance is the change in the A-probe resonance frequency, which must be reduced to zero. The measure of the disturbance rejection is the sensitivity function, shown in Figure 4.18. Even though the design requirements specify the desired tracking bandwidth as a requirement rather than the sensitivity function bandwidth, these two values are closely related [74]. Finally, the step response of the close loop system was evaluated and is shown in Figure 4.19. There is also the system

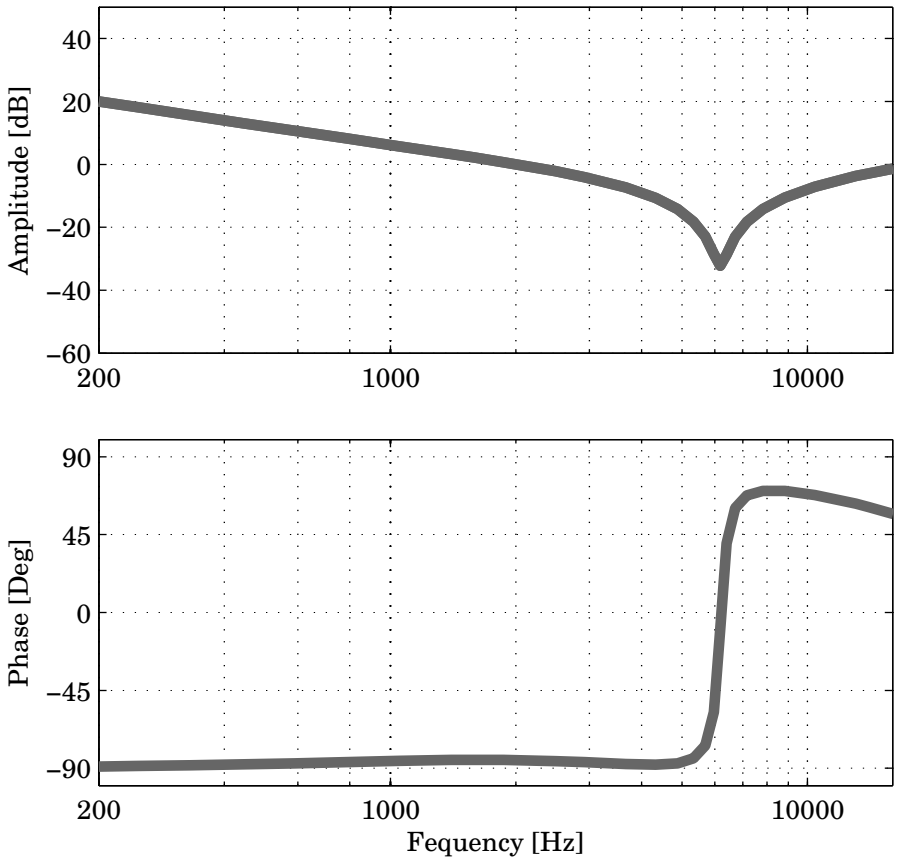

Figure 4.15: Designed digital controller Bode plot.

open loop step response plotted in order to illustrate the feedback action in the response. It is clear that the steady state error visible in the open loop response is minimized by the controller integrator. Moreover, the stage is settling much faster on the given displacement level.

The designed digital controller was implemented via the SIMULINK/dSPACE interface. The controller was loaded from the MATLAB workspace into the SIMULINK block. The actuator output was limited via the termination block in SIMULINK, which is a safety measure against instabilities while tuning. Controller described by Equation 4.8 was on-line tuned via stepwise increasing of the proportional gain from 0.01 to 1. The closed loop responses to the 7 μm and 13 μm steps are shown in Figures 4.20 and 4.21, correspondingly. The plots show the input responses to a inputs together with the actuation signals. Experiments showed the non-linearity of the piezoelectric actuator in the stage responses. The system gains were increasing for the increasing step values, which yielded the limited controller gains for the larger displacement ranges. This is originating from the system stiffness increasing with the larger actuator voltage applied. When increasing the controller gains for the larger amplitudes of motion, the measured signal contained more of the 6 kHz ripple in the response than at the lower motion amplitudes. The step response in Figure 4.21 proves that the stage can displace by the 10 μm distance in a controllable fashion. Moreover, the actuator signal shows, that the step of 13 μm with approximately 10% overshoot uses only 70% of the maximum input voltage, thus the actuator saturation does not limit the stage performance. Additionally, the stage inverse response

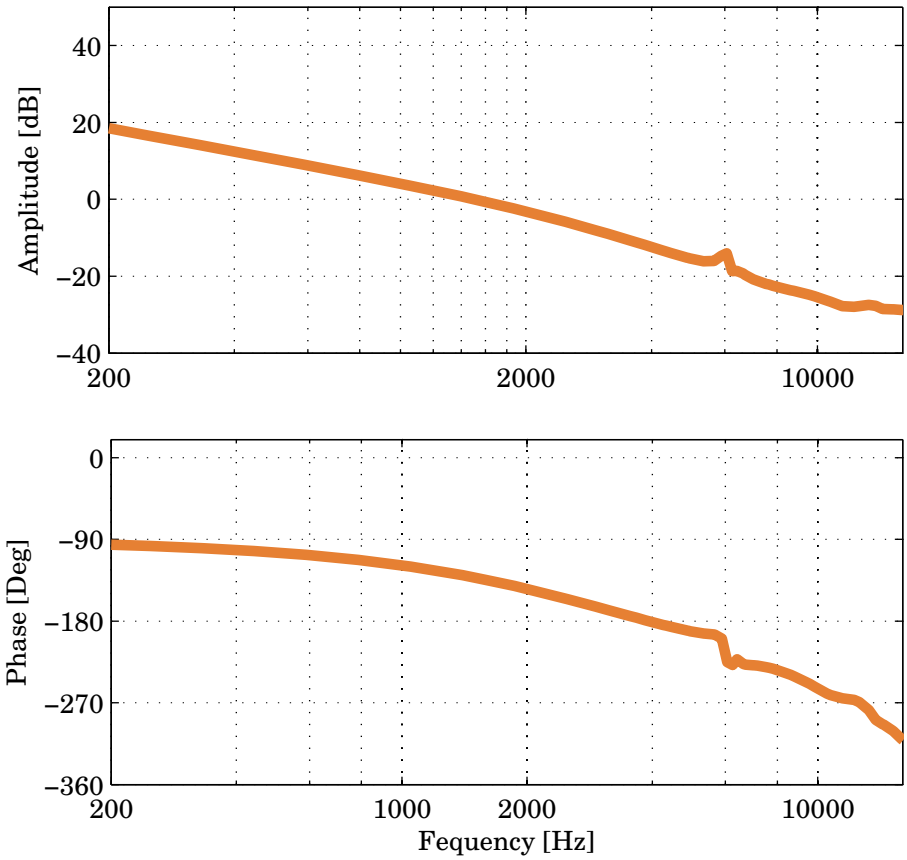

Figure 4.16: Open loop Bode plot.

is visible in the step responses. This means that the stage moves slightly in the opposite direction at the very start of the step. Such behaviour is tipical for the overconstrained systems and the generic non-phase minimum systems. A closed loop frequency response was evaluated with the multisine signal [71], similar as the open loop system identification described in Section 4.2. The multisine transfer functions obtained from the multisine peak to peak amplitudes of 350 nm, 7 μm, and 10.1 μm are shown in Figures 4.22, 4.23, and 4.24, respectively. It was observed, that the driving amplitude considerably affects the stage dynamics. For the 350 nm motion amplitude with the controller of gain 1, the frequency response did not show any noticeable signal ripple. On the contrary, for the higher voltage amplitudes, there were oscillations present in the bandwidth crossover region and the controller gain was decreased. In other words, it is more difficult for feedback to control the motion of higher amplitudes. The variation of the system's stiffness with the motion amplitude implies the selection of the robust controller settings. The controller should have the gain, which is high enough to achieve the desired bandwidth at lower amplitudes. Yet, it should have a sufficiently limited gain for stability and vibration in the higher motion amplitudes. The value of 0.7 was chosen as the reasonable compromise between these two objectives. The bandwidth at lower amplitudes is still over the 2kHz level for this gain. As for the stability of the 10 μm peak to peak motion, the phase margin was evaluated from the complimentary sensitivity as

$$PM = 2asin\left(\frac{1}{2M_r}\right), \tag{4.9}$$

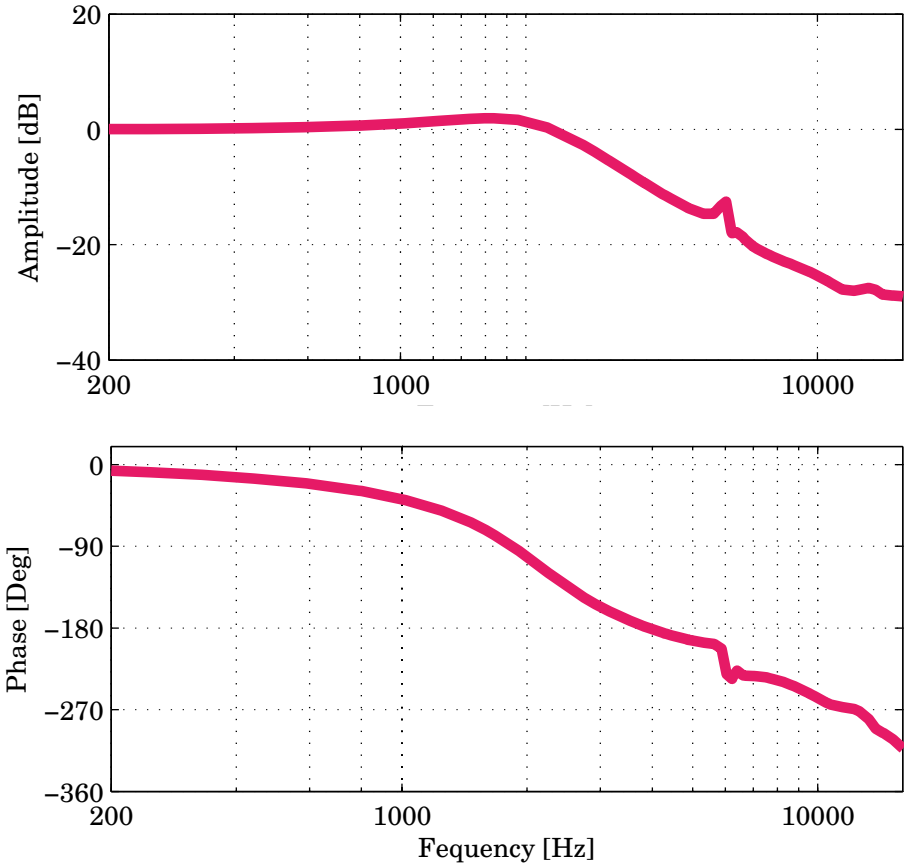

Figure 4.17: Closed loop Bode plot.

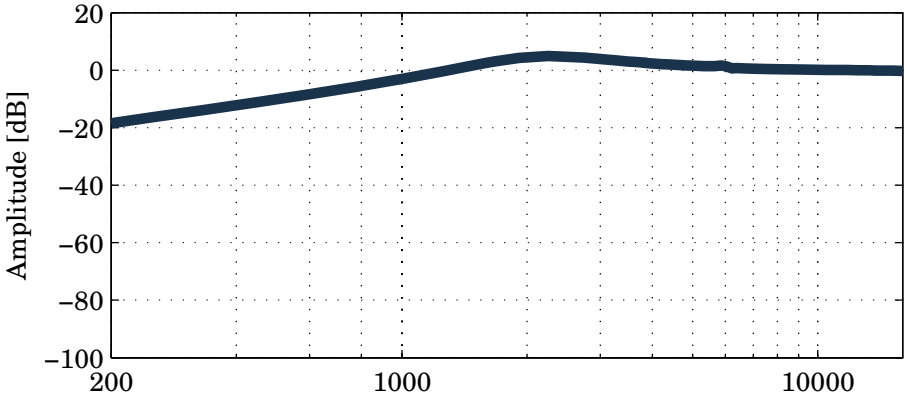

Figure 4.18: Sensitivity function Bode plot.

where M_r is the maximal closed loop amplification (1.1458). The calculated phase margin is 51°, which is an acceptable value.

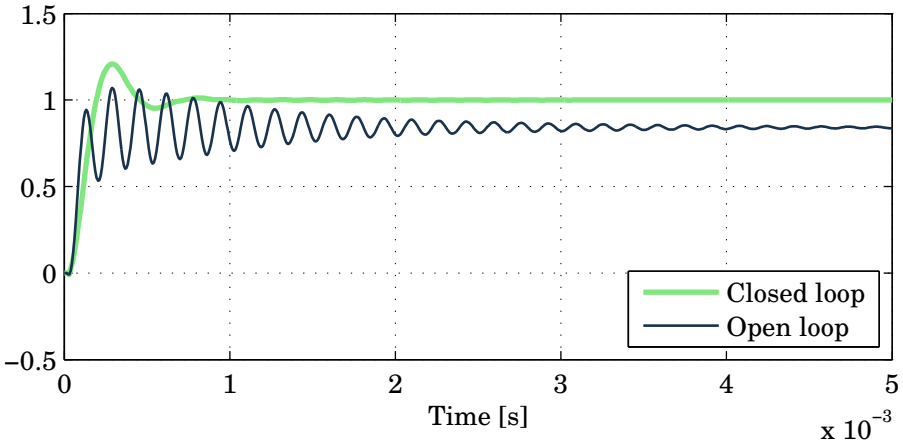

Figure 4.19: Open and closed loop step responces.

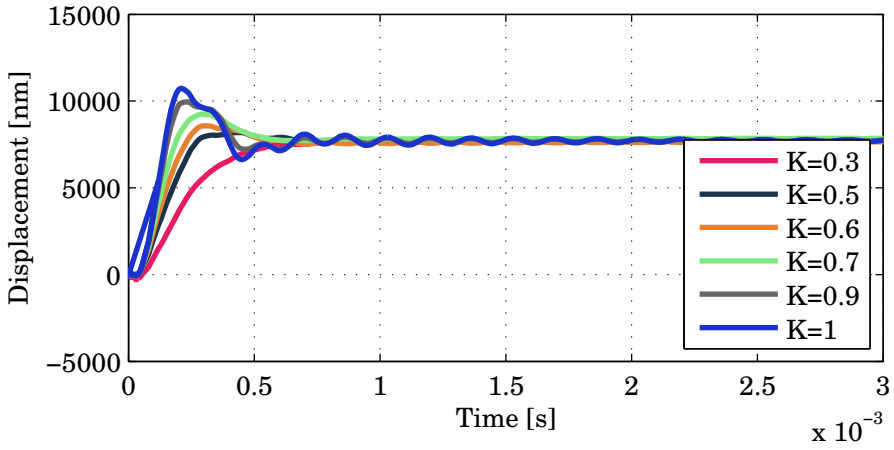

(a) Stage displacement.

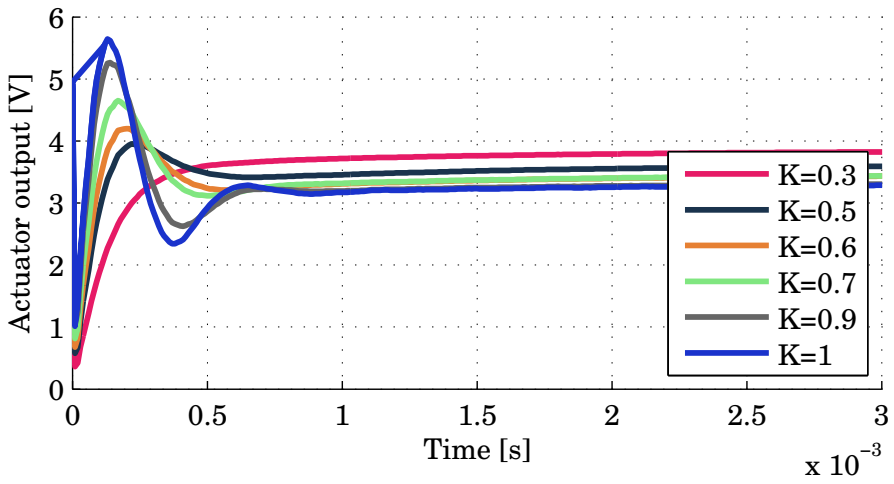

(b) Actuator signal.

Figure 4.20: Scanner's response to a 7 μm step.

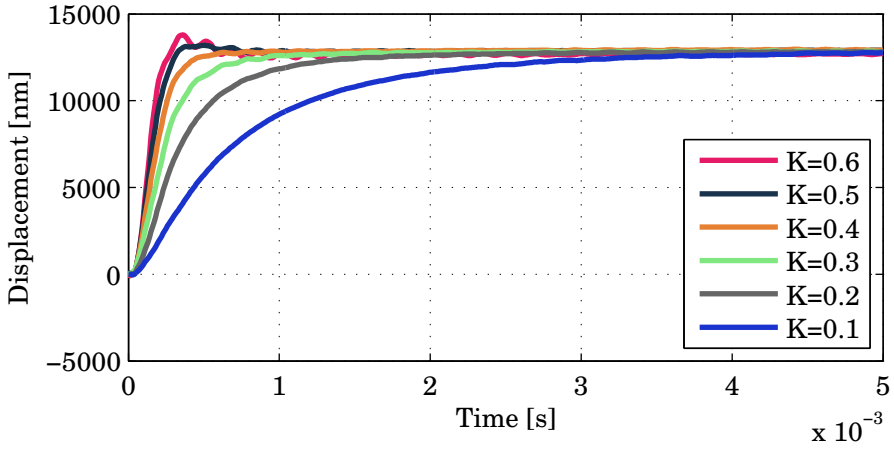

(a) Stage displacement.

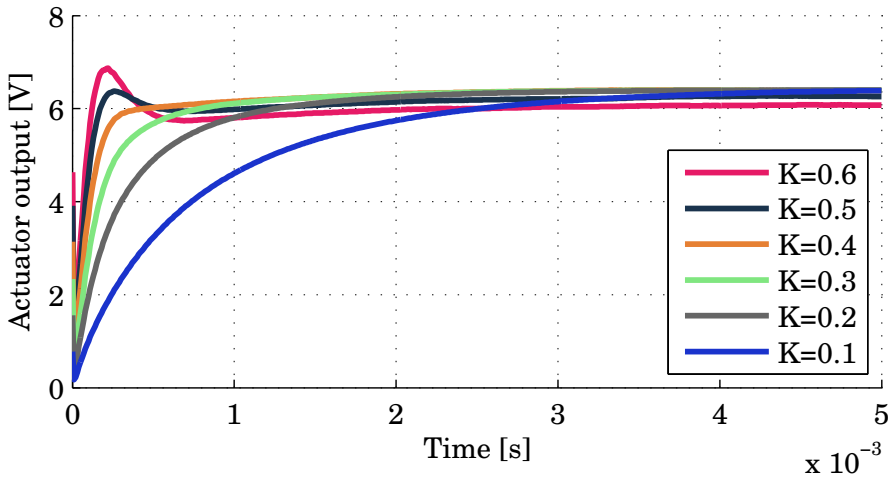

(b) Actuator signal.

Figure 4.21: Scanner's response to a 13 μm step.

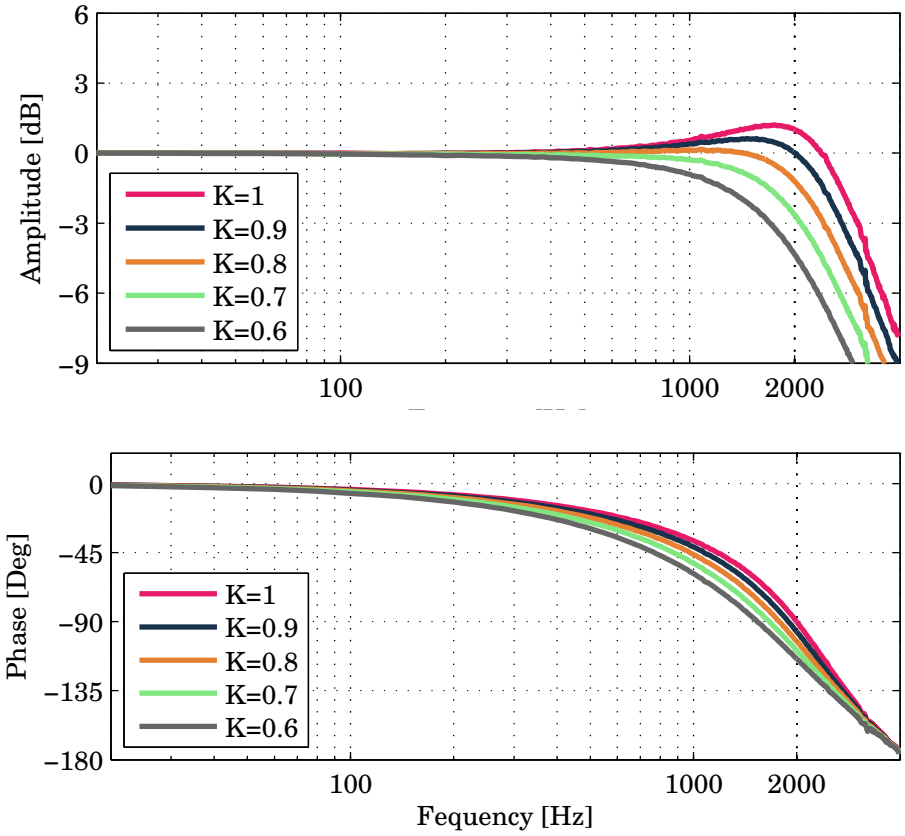

Figure 4.22: Closed loop frequency response for 350 nm peak to peak sine input.

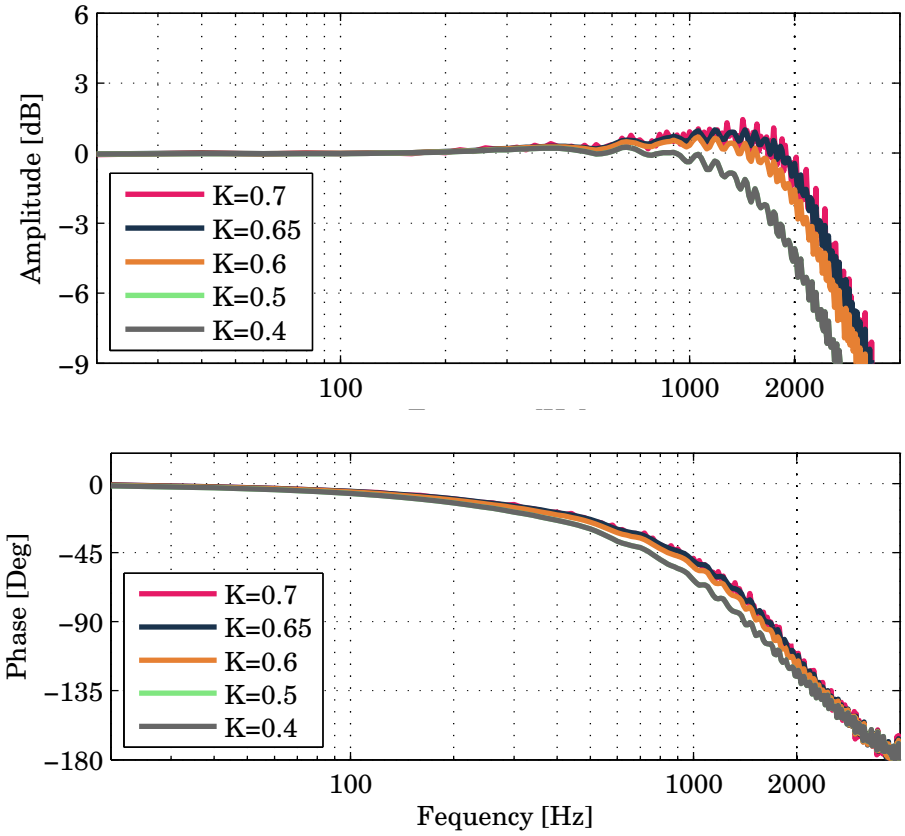

Figure 4.23: Closed loop frequency response for 7μm peak to peak sine input.

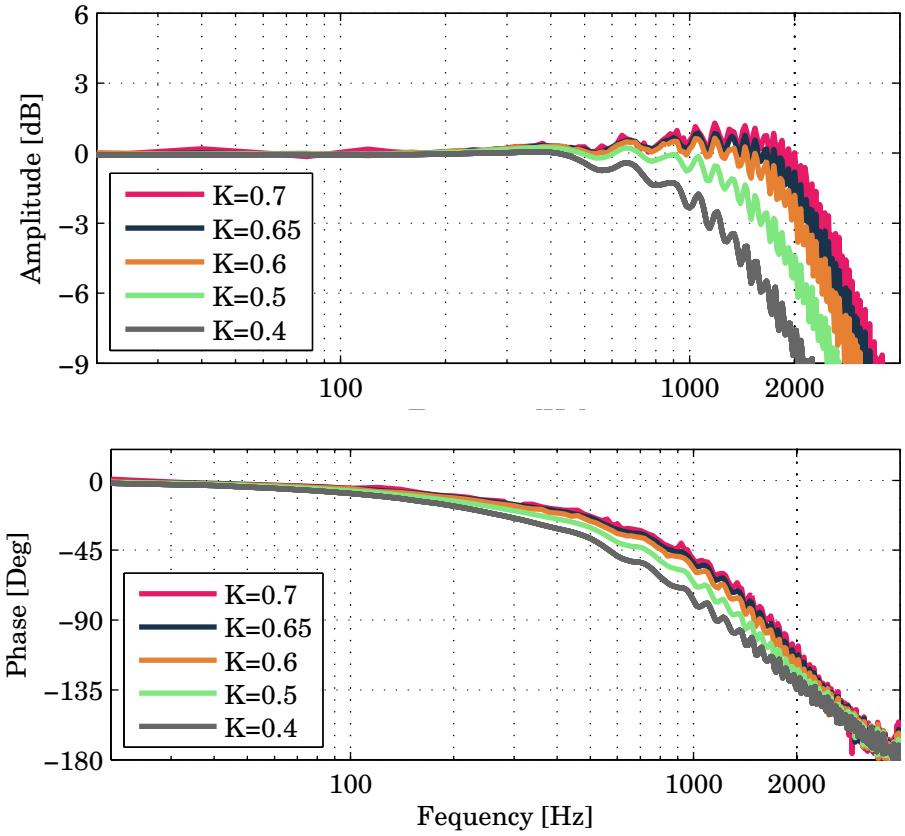

Figure 4.24: Closed loop frequency response for 10.1 μm peak to peak sine input.

4.5 Closed loop resolution

One of the system requirements was the resolution level below 0.1 nm. The dSPACE data acquisition system used has 16 bits resolution on input and output channels used. In practice it is difficult to make use of all 16 bits, and a 14 bits is assumed as the dSPACE system capability. If the stage travel range is δ_{max}, and the data acquisition has n bits, the achievable resolution is

$$r = \frac{\delta_{max}}{2^n}. \tag{4.10}$$

This implies, that if the scanner travels 13 µm, the theoretically maximum attainable resolution is 0.7935 nm. However, this value can be improved. The minimum sampling frequency is limited by the Nyquist criterion and should be at least $N_{Nyquist}$ = 2.5 times higher than the system bandwidth. Typical a higher minimum sampling frequency of N_{min}=4.5 times the bandwidth is assumed. If the data is sampled N_{max} times faster than the required minimal value, N_{min}, one obtains more data points and these data can be averaged, so the final resolution is improved by $\sqrt{N_{max}}$. In case of the 13µm stage travel at 2kHz bandwidth and sampled at 100 kHz, the achievable resolution is 0.2509 nm which is 3.1623 times improved due to oversampling. Nevertheless to achieve a required resolution better than 0.1 nm, the stage travel would need to be reduced to 5 µm. This is an idealized and theoretical case, which does not include the noise level additionally limiting the resolution. The noise and resolution achievable by the stage in closed loop operation were determined experimentally. The measured square wave signals of different stage motion amplitudes are shown in Figures 4.25 and 4.26. Figure 4.26 shows a 3.8 µm square wave motion at 1 Hz frequency. The motion amplitude was grad-

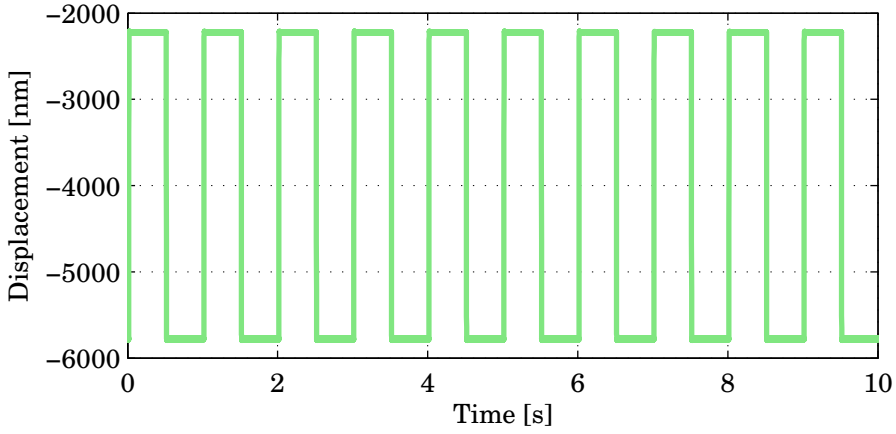

Figure 4.25: 3µm square wave stage motion.

ually decreased to determine the minimal amplitude which is distinguishable from the noise signal. This is illustrated by Figure 4.26. It is clear that the amplitudes of less than 25 nm (blue line) are buried in noise. The blue line represents the critical scenario, where the noise bands of the signal are not overlapping each other, hence the square wave can be recognized. A six pole Butterworth low pass filter of 2.3 kHz cut-off was applied at the sensor output outside the feedback loop to demonstrate the noise reduction of the sensor output. Figure 4.27 shows

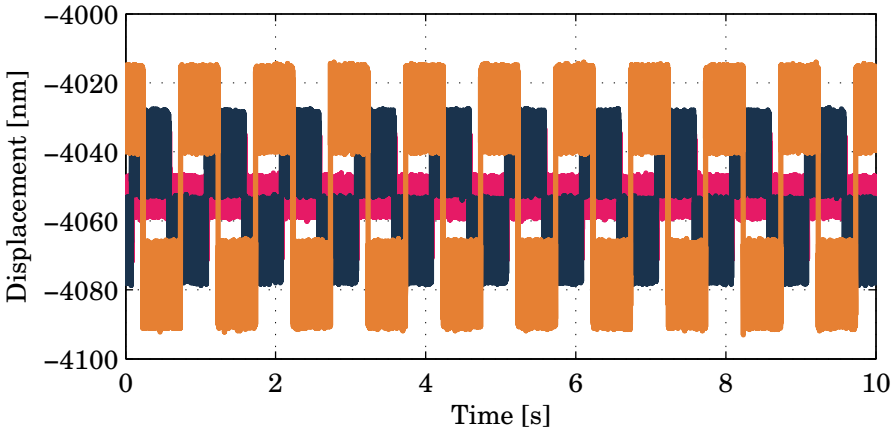

Figure 4.26: Square wave stage motion of different amplitudes.

three square wave signals of different amplitudes sent to the stage. The plots were offset from each other for illustrative purposes. It is clear that the stage can make distinguishable steps of 2.86 nm, which improved the resolution over 8 times. The noise level is equal 0.7 nm. The filter will filter the higher frequency data, however it was intended to show the improvement in the sensor signal quality. The noise can be also removed by the averaging. Averaging over 10 data points should reduce the noise level by the factor of 3.3.

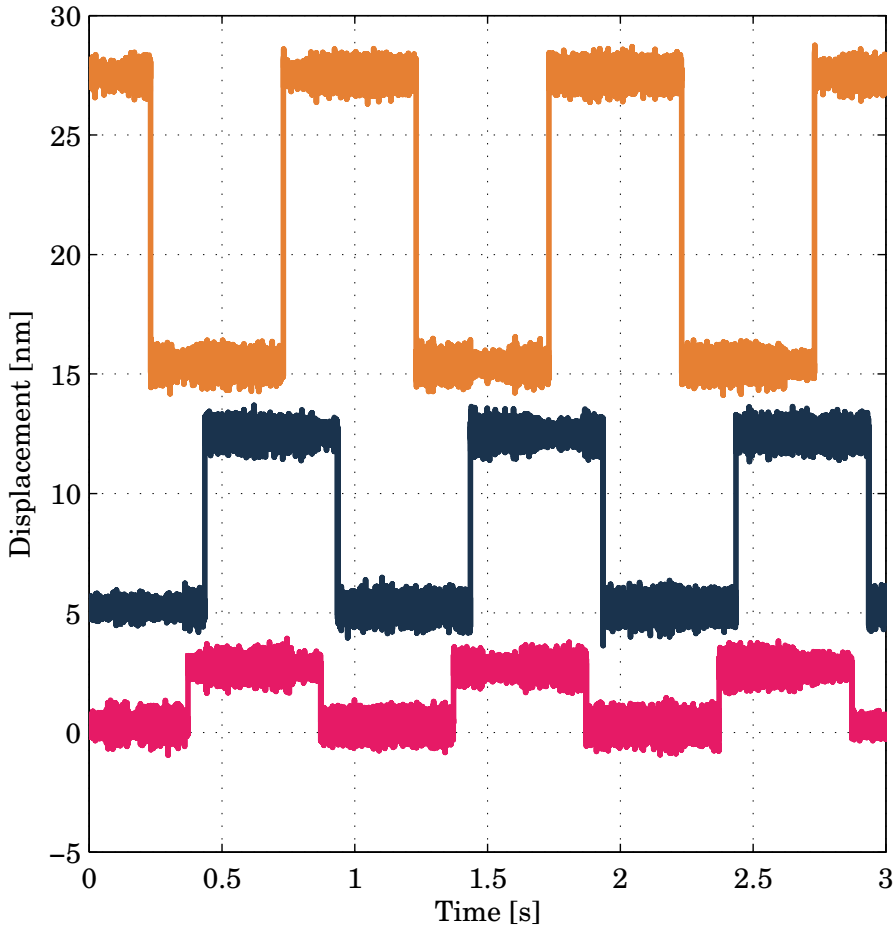

Figure 4.27: Square wave stage motion of different amplitudes with filtering applied.

Chapter 5

Measurement uncertainty calculation

5.1 Introduction

The concept of measurement uncertainty is related and originates from the incomplete knowledge of the quantity measured. The concept has been developed into a standardized and transferable characteristic of the measurement, as is extensively covered by the internationally recognized standards [75, 76]. There are different definitions of the measurement uncertainty, for instance: *"a parameter, associated with the result of a measurement, that characterizes the dispersion of the values that could reasonably be attributed to the measurand"* [76]. Uncertainty formulated for a specific measurement may have many components. These components can be evaluated, for instance, from the statistical distribution of the experimental data, assumed probability distributions, level of experience etc. However they are typically defined and based on the probability distribution [76]. It is important that the measurement uncertainty also includes the uncertainties of correction factors, the uncertainties of the measurement standards, and all the other factors limiting one's knowledge on the measurand [76]. The uncertainty analysis described in this work are based on the 'Guide to the expression of uncertainty in measurement' (GUM) [77, 76] and largely encompass the measurement uncertainty due to stage thermal expansion of the stage and the Abbé and cosine errors. These examples illustrate the concept in more detailed view, whereas the remaining measurement uncertainty components are treated less analytically. The formulation of the uncertainty and its final value is expressed at 1σ with 68.3% confidence interval of the normal probability distribution.

5.2 Thermal expansion

The positioning scanner has the thermal expansion due to temperature variations, ΔT, of its environment. The thermal expansion of an element having length, L, and a coefficient of thermal expansion (CTE), α, which is subjected to the temperature change, ΔT, is expressed as

$$\Delta L_{CTE} = \Delta T \alpha L. \tag{5.1}$$

The scanner thermal expansion directly induces a measurement error. The thermal expansion was investigated in this context. Since the stage is symmetric in the X-Y and Y-Z planes,

the thermal expansion in these planes is negligible and the analysis cover only the thermal expansion in the z-direction, which is the sensitive direction of motion. The scanner thermal expansion in the z-direction has two origins. First, the probe displaces. Second, the sensing gap of the capacitive gauge changes. The stage thermal expansion can be included in the measurement data if the current temperature is measured and registered. If the stage deformation due to the registered temperature change, ΔT, can be predicted, the measurement error introduced by thermal expansion can be compensated in the measurement output. The thermal expansion deformation can be determined up to the level of its uncertainty. The AFM scanner is designed to operate in a temperature controlled environment, which has a global temperature control, ΔT, better than 0.05°C. The temperature can be measured by a temperature sensor with an uncertainty, uT, of 0.001 °C. The uncertainty, uE_{CTE}, of the thermal expansion, ΔL_{CTE}, described by Equation (5.1), is

$$uE_{CTE} = \sqrt{\left(\frac{\partial E_{CTE}}{\partial \Delta T} uT\right)^2 + \left(\frac{\partial E_{CTE}}{\partial L_z} uL_z\right)^2 + \left(\frac{\partial E_{CTE}}{\partial \alpha} u\alpha\right)^2}, \tag{5.2}$$

which after differentiation yields:

$$u(T\alpha L_z) = \sqrt{(\alpha L_z uT)^2 + (\alpha \Delta T u L_z)^2 + (L_z \Delta T u\alpha)^2}. \tag{5.3}$$

The thermal deformation of the probe is caused by a thermal deformation of the stage and resulting displacement of face ‘d’ where the probe is mounted, thermal deformation of the mounting spheres, and thermal deformation of the ceramic plate of the A-probe. The thermal deformation of the stage is depicted in Figure 5.1. The vertical arrows indicate the segments of the material subjected to the thermal deformation, which affects the probe displacement. The signs of the arrows show in which direction the expansion occurs, assuming the temperature in increasing. For simplicity, the positive displacement direction, z, is pointing downwards, as shown in Figure 5.1 and the considered temperature change, ΔT, is an increase of the steady state temperature. The top, face ‘a’ of the stage, is treated as a rigid base which is a thermal datum. The segment L_1, which is the distance between face ‘a’ and the bottom flexure, expands downwards from the base in the positive z-direction by

$$\Delta L_1 = \alpha \Delta T L_1, \tag{5.4}$$

where α is the aluminium CTE and ΔT is the temperature change. This displacement causes a downward translation of the movable frame stage by the same amount ΔL_1, since the segment L_1 is rigidly attached to the movable stage frame via leaf springs. The thermal deformation of the aluminium segment, L_2, and piezoelectric actuator segment, L_3 is

$$\Delta L_2 + \Delta L_3 = \Delta T(\alpha L_2 + \alpha_{pzt} L_3), \tag{5.5}$$

where α_{pzt} is the piezoelectric actuator CTE. Since, $L_1 > L_2 + L_3$ and $\alpha_{pzt} < \alpha$, it is assumed $|\Delta L_1| > |\Delta L_2 + \Delta L_3|$. Consequently, the thermal expansion creates a gap between the bottom face of the piezoelectric actuator segment and the movable stage frame, equal to $\Delta L_1 - (\Delta L_2 + \Delta L_3)$. The flexures are preloaded and they move upwards by the distance equal to the change

in gap. This situation is valid assuming the preload displacement, discussed in Section 3.4.6, is larger than the gap $\Delta L_1 - (\Delta L_2 + \Delta L_3)$. Additionally, the aluminium segment, L_4, expands downwards from the piezoelectric actuator bottom face by

$$\Delta L_4 = \alpha \Delta T L_4. \tag{5.6}$$

Finally, one can describe the displacement of the stage bottom face 'd' as follows

$$\Delta L_2 + \Delta L_3 + \Delta L_4 = \Delta T \left[\alpha (L_2 + L_4) + \alpha_{pzt} L_3 \right]. \tag{5.7}$$

The thermal expansion induced displacement of the AFM probe is additionally related to the

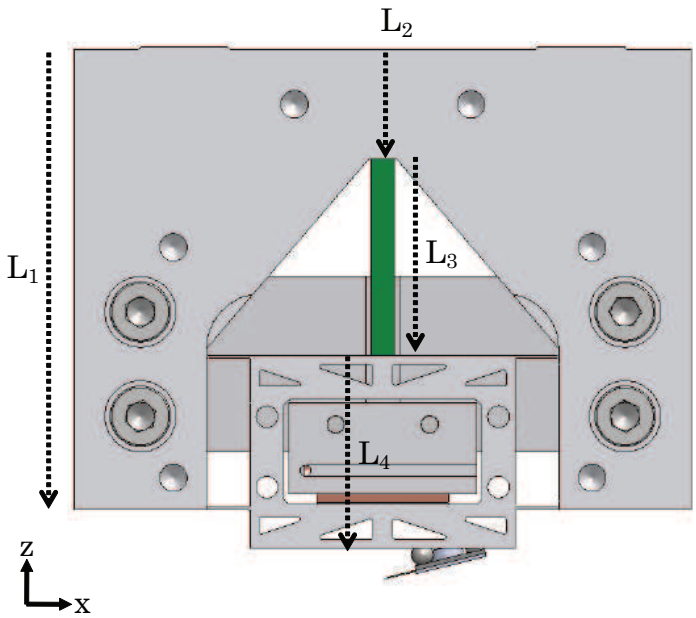

Figure 5.1: Thermal expansion of the flexural stage affecting the probe displacement.

thermal deformation of the mounting spheres forming the probe mount and the expansion of the AFM probe ceramic plate. Thermal expansion of the spheres increases their radii which changes the contact points between the spheres and the probe plate. In addition, the expanding spheres move the ceramic plate downwards and because the spheres are of different sizes, the probe plate inherits a rotational displacement affecting the probe position. The thermal expansion increases the diameters of circular holes on which the positioning spheres rest. This deformation may change the contact line between the mounting spheres and the circular cut-outs edges. It is however depending on the pulling force of the glue and its thermal expansion. Further, the thickness of the AFM probe plate increases due to thermal expansion, which is moving the probe downwards. In addition, the rectangular cut-outs in the ceramic plate expand, which is contributing to the change of contact points between the AFM probe plate and the mounting spheres. The maximum net probe displacement due to the mounting elements thermal expansion was evaluated and is approximately 1.5 nm. The error of this value was estimated as less than 0.15 nm. As explained above, the thermal expansion of the probe mount elements is quite complex. At the same time, its influence on the probe displacement is much

smaller than the thermal deformation of the other segments of the scanner. Thus it is not included in the net thermal expansion error nor in the formulation of its uncertainty. The thermal expansion induced displacement of the AFM probe is then equal to the displacement of the bottom stage face 'd' by

$$E_{probe} = \Delta T \left[\alpha(L_2 + L_4) + \alpha_{pzt} L_3\right], \tag{5.8}$$

which can be rewritten in a simplified form:

$$E_{probe} = \Delta T \left[\alpha(L_{p(al)}) + \alpha_{pzt} L_3\right]. \tag{5.9}$$

The value of E_{probe} due to a temperature change, ΔT (0.05°C), was calculated using Equation (5.8) and is equal to 68 nm. The uncertainty of Equation (5.8) can be expressed as:

$$\begin{aligned} uE_{probe} = & \sqrt{\left(\frac{\partial E_{probe}}{\partial \Delta T} uT\right)^2 + \left(\frac{\partial E_{probe}}{\partial L_{p(al)}} uL_{p(al)}\right)^2 + \left(\frac{\partial E_{probe}}{\partial L_3} uL_3\right)^2} \\ & \overline{+ \left(\frac{\partial E_{probe}}{\partial \alpha} u\alpha\right)^2 + \left(\frac{\partial E_{probe}}{\partial \alpha_{pzt}} u\alpha_{pzt}\right)^2}, \end{aligned} \tag{5.10}$$

where uL_3 and $uL_{p(al)}$ are length uncertainties of segments L_3 and $L_{p(al)}$, respectively and $u\alpha_{pzt}$ is the uncertainty of piezoelectric actuator thermal expansion coefficient. The evaluated expression for Equation (5.10) has the expanded form

$$\begin{aligned} uE_{probe} = & \sqrt{\left(\alpha L_{p(al)} uT\right)^2 + \left(\alpha_{pzt} L_3 uT\right)^2 + (TL_5 u\alpha)^2 + \left(TL_3 u\alpha_{pzt}\right)^2} \\ & \overline{+ (T\alpha)^2 \left(uL_{p(al)}^2 + uL_3^2\right)}. \end{aligned} \tag{5.11}$$

The calculated value of this uncertainty is equal to 0.73 nm. The summary of the main contributions of uE_{probe} is presented in Table 5.1. This comparison indicates the two main contributing elements are $\left(\alpha L_{p(al)} uT\right)^2$ and $(TL_5 u\alpha)^2$. The displacement of the face 'c' of the movable

Table 5.1: Summary of uE_{probe}.

Component	Variance [nm^2]	Standard deviation [nm]
$\left(\alpha L_{p(al)} uT\right)^2$	0.42	0.65
$\left(\alpha_{pzt} L_3 uT\right)^2$	0.0013	0.036
$(TL_5 u\alpha)^2$	0.104	0.32
$\left(TL_3 u\alpha_{pzt}\right)^2$	0.0324	0.018
$\left(T\alpha u L_{p(al)}\right)^2$	0.034	0.059
$(T\alpha u L_3)^2$	0.034	0.059

stage frame, depicted in Figure 5.2, can be expressed by

$$\Delta L_2 + \Delta L_3 + \Delta L_5 = \Delta T(\alpha(L_2 + L_5) + \alpha_{pzt} L_3), \tag{5.12}$$

where L_5 is the length of the aluminium segment between face 'b' and 'c' of the stage movable frame. From the face 'b' of the stage, the glass piece segment, L_7, and copper segment L_8 expand upwards by

$$\Delta L_7 + \Delta L_8 = -\Delta T(\alpha_{gl} L_7 + \alpha_{cop} L_8). \tag{5.13}$$

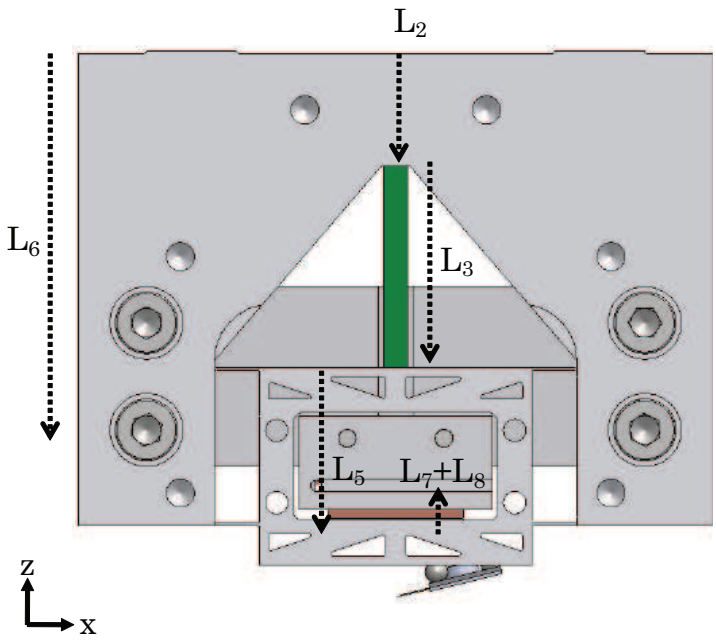

Figure 5.2: Stage thermal expansion affecting the sensing gap length.

Hence, one can express the displacement of the target sensor electrode top face, which creates the sensing gap

$$E_{gap(t)} = \Delta L_2 + \Delta L_3 + \Delta L_5 + \Delta L_7 + \Delta L_8, \tag{5.14}$$

which can be written as

$$E_{gap(t)} = \Delta T \left[\alpha(L_2 + L_5) + \alpha_{pzt} L_3 - \alpha_{gl} L_7 - \alpha_{cop} L_8 \right]. \tag{5.15}$$

This displacement occurs in the downward direction with the increasing temperature and the evaluated displacement $E_{gap(t)}$ is 28 nm. Further, the displacement of the sensing electrode face, which also affects the gap length is evaluated. The aluminium segment, L_6, described in Figures 5.2 and 5.3 is representing the segment of the stage frame starting from the base, passing through the sensor mounting bracket and finally ending up at the aluminium sensor assembly part. Even though there are three parts which create the length L_6, it is treated as a single segment, since the three parts are made of the same material. The thermal expansion of segment, L_6 is

$$\Delta L_6 = \alpha \Delta T L_6. \tag{5.16}$$

The other elements of capacitive sensor assembly, are shown in Figure 5.3. There are two glass insulation layers, designated as segments L_9 and L_{10}, which expand downwards by

$$\Delta L_9 + \Delta L_{10} = \alpha_{gl} \Delta T (L_9 + L_{10}). \tag{5.17}$$

The copper elements of the assembly, the electrode guard and the sensing electrode represented by segments L_{11} and L_{12} respectively, expand downwards by

$$\Delta L_{11} + \Delta L_{12} = \alpha_{cop} \Delta T (L_{11} + L_{12}). \tag{5.18}$$

Combining Equations (5.16), (5.16), (5.18) the net displacement of the target sensing electrode face gap is

$$E_{gap(s)} = \Delta L_6 + \Delta L_9 + \Delta L_{10} + \Delta L_{11} + \Delta L_{12}, \tag{5.19}$$

which can be rewritten as

$$E_{gap(s)} = \Delta T \left[\alpha L_6 + \alpha_{gl}(L_9 + L_{10}) + \alpha_{cop}(L_{11} + L_{12}) \right]. \tag{5.20}$$

The overall displacement of the sensing electrode occurs in downwards direction with the increasing temperature and is 45 nm, which is larger than the thermal displacement of the target electrode, $E_{gap(s)}$. This implies, that for the increasing temperature, the sensing gap will become smaller by the difference between $E_{gap(s)}$ and $E_{gap(t)}$, which corresponds to the stage being moved upwards. It has been shown, that the increasing temperature yields a thermal expansion of the stage and hence the probe downwards. Thus the thermally induced gap change error should be added to the error E_{probe}. The change of the gap length is equal to the difference between displacement of the target electrode face, $E_{gap(t)}$ and the displacement of the sensing electrode face $E_{gap(s)}$, by

$$E_{gap} = E_{gap(t)} - E_{gap(s)}, \tag{5.21}$$

which, after further evaluation, is

$$\begin{aligned} E_{gap} \quad = \quad & \Delta T[\alpha(L_2 + L_5 - L_6) + \alpha_{pzt} L_3 - \alpha_{gl}(L_7 + L_9 + L_{10}) \\ & - \alpha_{cop}(L_8 + L_{11} + L_{12})], \end{aligned} \tag{5.22}$$

and may be rewritten in a simplified form

$$E_{gap} = \Delta T \left[\alpha L_{g(al)} + \alpha_{pzt} L_3 - \alpha_{gl} L_{g(gl)} - \alpha_{cop} L_{g(cop)} \right], \tag{5.23}$$

The value of the gap change due to the temperature change is 16.8 nm. The uncertainty of Equation (5.23) is expressed as follows

$$\begin{aligned} uE_{gap}^2 \quad = \quad & \frac{uT^2 \Big[\left(\alpha L_{g(al)}\right)^2 + \left(\alpha_{pzt} L_3\right)^2 + (\alpha_{g(gl)} L_{g(gl)})^2 + (\alpha_c L_{g(c)})^2 \Big]}{+\Delta T^2 \Big[\left(\alpha u L_{g(a)}\right)^2 + \left(\alpha_{pzt} u L_3\right)^2 + \left(\alpha_{gl} u L_{g(gl)}\right)^2 + \left(\alpha_c u L_{g(c)}\right)^2} \\ & + \left(L_{g(al)} u \alpha\right)^2 + \left(L_3 u \alpha_{pzt}\right)^2 + \left(L_{g(gl)} u \alpha_{gl}\right)^2 + \left(L_{g(c)} u \alpha_c\right)^2 \Big]. \end{aligned} \tag{5.24}$$

(5.25)

The calculated value of this uncertainty is 0.35 nm. The detailed summary of the contributions of uE_{gap} is shown in Table 5.2. The major contributors of the net value of this uncertainty are the terms $\left(uT\alpha L_{g(al)}\right)^2$, $\left(\Delta T^2 \alpha u L_{g(a)}\right)^2$ and $\left(\Delta T^2 L_{g(al)} u \alpha\right)^2$. This expressions contain the terms of the aluminium thermal expansion, α and L_{al}, which has a high CTE.

The thermal expansion induced measurement uncertainties can be treated separately. It is assumed that they are not correlated in order to represent the most critical case scenario. The estimated measurement uncertainty due to the thermal expansion is

$$U_{CTE} = \sqrt{uE_{gap}^2 + uE_{probe}^2}, \tag{5.26}$$

and is equal to 0.81 nm.

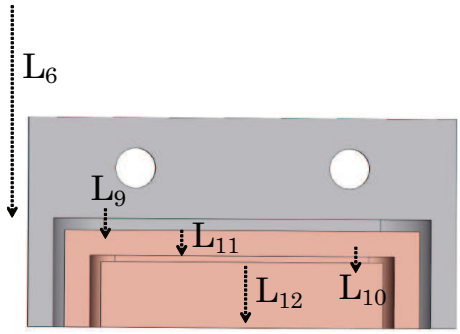

Figure 5.3: Thermal expansion of the capacitive sensor probe - section view of the assembly.

Table 5.2: Summary of uE_{gap}.

Component	Variance [nm^2]	Standard deviation [nm]
$\left(uT\alpha L_{g(al)}\right)^2$	0.09	0.3
$\left(uT\alpha_{pzt}L_3\right)^2$	0.0013	0.036
$\left(uT\alpha_{g(gl)}L_{g(gl)}\right)^2$	0.000018	0.0042
$\left(uT\alpha_c L_{g(c)}\right)^2$	0.0044	0.066
$\left(\Delta T^2\alpha u L_{g(a)}\right)^2$	0.0009	0.029
$\left(\Delta T^2\alpha_{pzt}uL_3\right)^2$	0.000001	0.001
$\left(\Delta T^2\alpha_{gl}uL_{g(gl)}\right)^2$	0.000004	0.002
$\left(\Delta T^2\alpha_c uL_{g(c)}\right)^2$	0.000256	0.016
$\left(\Delta T^2 L_{g(al)}u\alpha\right)^2$	0.023	0.15
$\left(\Delta T^2 L_3 u\alpha_{pzt}\right)^2$	0.000324	0.018
$\left(\Delta T^2 L_{g(gl)}u\alpha_{gl}\right)^2$	0.000004	0.0021
$\left(\Delta T^2 L_{g(c)}u\alpha_c\right)^2$	0.0001076	0.033

Table 5.3: Summary of the thermal lengths.

Symbol	Length [mm]	Symbol	Length [mm]
L_1	41.9	L_2	10
L_3	18	L_4	17.5
L_5	13.5	L_6	36.4
L_7	0.15	L_8	1
L_9	0.45	L_{10}	0.45
L_{11}	1	L_{12}	2

5.3 Abbé error and cosine error

The Abbé error and cosine error are two commonly encountered measurement errors [5]. Theses errors occur if the stage motion straightness is not ideal and an angle, θ, is created between the axis of stage motion and the axis along which the displacement measurement is taken. The angle θ is indicated in Figure 5.4 and is formed by the lines OM and OM', where the line OM indicates the measurement axis and the line OM' represents the maximal straightness error of the stage movement relative to the measurement axis. The angle θ can be formed both in the X-Z and Y-Z plane, hence there are θ_x and θ_y error contributions. An Abbé error is related to a

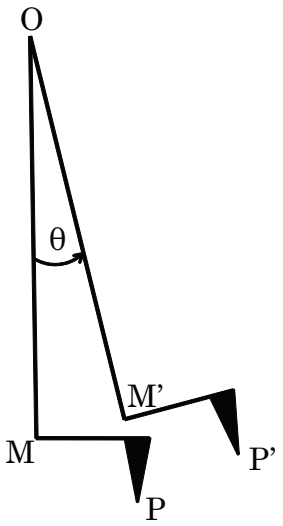

Figure 5.4: Abbé and cosine error illustration.

non-zero misalignment angle between the current axis of stage motion and the axis of capacitive measurement registering the motion, θ_x and θ_y. The error is created if there is a non-zero distance between the force measurement point (the point of AFM probe tip placement) and the axis of stage motion, also called the Abbé offset, δ_{Abbe}. The Abbé offset is shown in Figure 5.4 is line MP. The Abbé error is caused by a rotation, θ, of the Abbé arm MP, which in turn causes the vertical displacement of the probing point P

$$E_{Abbe} = MPsin(\theta). \tag{5.27}$$

The position measurement system, the capacitive sensor, would not register this rotation, thus the probing point displacement from P to P' becomes indistinguishable and the error E_{Abbe} is fed to the topography measurement. The Abbé error in X-Z plane originates from the measurement being taken at a point off-set from the measurement axis by a distance, δx_{Abbe}. The angle between measurement and motion axis about y, θ_y, is

$$E_{Abbe(x)} = \delta x_{Abbe} sin\left(\theta_y\right), \tag{5.28}$$

By analogy, the Abbé error in Y-Z plane, $E_{Abbe(y)}$, is represented by

$$E_{Abbe(y)} = \delta y_{Abbe} sin\left(\theta_x\right), \tag{5.29}$$

The Abbé offset can be measured by means of an optical measurement microscope with an uncertainty, uA_{Abbe}, of approximately 20 μm. The maximum expected Abbé offsets, δx_{Abbe} and δy_{Abbe}, can be evaluated based on the manufacturing tolerances, 0.25 mm and 0.08 mm, respectively. The straightness error angle, θ can be determined experimentally via recording of the stage rotation during full stroke. This can be achieved by measuring of the displacement at two points at stage bottom face. The achievable uncertainty of such measurement, $u\theta_x$, $u\theta_y$ can be better than 0.1 μrad. The maximum expected straightness error, θ_x, θ_y is 10 μrad. The maximum Abbé errors $E_{Abbe(x)}$, $E_{Abbe(y)}$ were calculated using (5.28) and (5.29) and are 2.5 nm and 0.8 nm, respectively. The Abbé error can be compensated up to the uncertainty level defined by

$$uE_{Abbe} = \sqrt{\left(\frac{\partial E_{Abbe}}{\partial \theta} u\theta\right)^2 + \left(\frac{\partial E_{Abbe}}{\partial \delta_{Abbe}} u\delta_{Abbe}\right)^2}, \tag{5.30}$$

which yields the uncertainties of the X-Z plane and Y-Z plane Abbe error

$$uE_{Abbe(x)} = \sqrt{\left(\delta x_{Abbe} cos\left(\theta_y\right) u\theta_y\right)^2 + \left(sin\left(\theta_y\right) u\delta x_{Abbe}\right)^2}, \tag{5.31}$$

and

$$uE_{Abbe(y)} = \sqrt{(\delta y_{Abbe} cos(\theta_x) u\theta_x)^2 + (sin(\theta_x) u\delta y_{Abbe})^2}. \tag{5.32}$$

Using Equations (5.31) and (5.32) the maximum expected uncertainties $uE_{Abbe(x)}$ and $uE_{Abbe(y)}$ were evaluated and both account for 0.2 nm. While the difference between Abbé offsets $\delta_{Abbe}(x)$ and $\delta_{Abbe}(y)$ significantly affects the corresponding Abbé errors values, it is much less visible if one compares the related uncertainties $uE_{Abbe(x)}$ and $uE_{Abbe(y)}$. The second measurement

Table 5.4: Summary of $uE_{Abbe(x)}$ and $uE_{Abbe(y)}$.

Component	Variance [nm^2]	Standard deviation [nm]
$\left(\delta x_{Abbe} cos\left(\theta_y\right) u\theta_y\right)^2$	0.000064	0.008
$\left(sin\left(\theta_y\right) u\delta x_{Abbe}\right)^2$	0.25	0.5
$(\delta y_{Abbe} cos(\theta_x) u\theta_x)^2$	0.000225	0.015
$(sin(\theta_x) u\delta y_{Abbe})^2$	0.25	0.5

artefact is related to the misalignment angle, θ, the cosine error. Cosine error occurs due to a measurement taken along an axis not parallel to the motion axis. Physically it means that the displacement is measured under a non-zero angle, θ, thus the measured value differs from the true displacement. In Figure 5.4, the cosine error can be seen as a length difference between the lines OM and OM' by

$$E_{cos} = OM - OM' = OM(1 - cos(\theta)). \tag{5.33}$$

The cosine error is a fraction of the true measured distance. Thus, its maximum value is typically evaluated for the case of full stroke measurement. Similar to the Abbé error, the cosine error is formed in the X-Z and Y-Z planes, and is expressed as

$$E_{cos(x)} = \delta z_{real} \left[\frac{1}{cos\left(\theta_y\right)} - 1\right] \text{ and} \tag{5.34}$$

$$E_{cos(y)} = \delta z_{real} \left[\frac{1}{cos(\theta_x)} - 1 \right], \tag{5.35}$$

where δz_{real} is the 'real' measured distance. The maximum cosine errors $E_{cos(x)}$, $E_{cos(x)}$ are 0.005 pm, which is a negligible value.

5.4 Other uncertainty sources

There are other measurement uncertainty sources evaluated in this research. The capacitive sensor noise and the amplifier noise were measured and contribute together 0.7 nm uncertainty. The capacitive sensor is deformed due to the actuation, as described in Section 3.4.5 and the predicted model accommodates 1 nm of related error. This value is however accounted in the stage static calibration uncertainty of 1.2 nm. Similar, the actuation induced probe displacement is calibrated within the calibration uncertainty. The sensor is expected to be deformed due to the squeeze film damping forces, introduces 0.5 nm error of the sensor measurement. Additionally, the dynamic reaction forces exerted on the structural frame introduce the error of 1.2 nm. The AFM probe also introduces uncertainty, which comprises the force measurement uncertainty and the uncertainty introduced by the probe electronics. Moreover, its dynamic characteristic is affected by the temperature and humidity changes, which increase the probe measurement uncertainty. There was, however, no research published which could be used as a reference in estimating the A-probe sensing uncertainty, yet investigating it would be a valuable continuation of the present research. Hence, the probe measurement uncertainty is not treated in this research.

5.5 Overall uncertainty calculation

The summary of all contributions to the overall scanner topography measurement uncertainty are listed in Table 5.5. The total uncertainty of the measurement system is a resultant of all uncertainty contributions. It was calculated according to the normal probability distribution (1σ and is equal to 2 nm.

Table 5.5: Uncertainty contributions and their values.

Component	Variance [nm^2]	Standard deviation [nm]
Thermal expansion	0.64	0.8
Scanner elastic deformation	1.44	1.2
Static calibration uncertainty	1	1
Abbé and cosine errors	0.504	0.71
Capacitive sensor/amplifier noise	0.49	0.7
Capacitive sensor elastic deformation	0.16	0.4
Total	4.25	2

Chapter 6

Conclusions and future work

6.1 Conclusions

The Atomic Force Microscope vertical scanner was developed according to the design specifications. The research began with a literature survey on AFM technology in the context of a vertical scanner design. The initial analysis treated the specifications of the required system. The conceptual design included the choice of the scanner as a monolithic flexure guidance mechanism integrated with the piezoelectric actuator, the capacitive position feedback system, and a self sensing - self oscillating AFM probe. During the research the initial concepts were readjusted relatively to the initial strategies due to the constraints and limitations imposed by the respective modules on each other or, for instance, the complicated manufacturing process. However, the initial assumptions held up to the finalisation of the design. The conceptual phase was followed by the modelling and detail design of stage components which finally lead to the manufacturing, assembling and testing of the developed scanner. The built system achieved the required bandwidth of over 2 kHz and the travel range of over 10 μm. The measurement system uncertainty was evaluated and is 2 nm. Yet, to reach the quoted uncertainty some additional steps must be made. They are briefly discussed in the later section. Nevertheless, the measurement uncertainty requirement is theoretically met at the current state of the research. It has been shown that the measurement error of 77 nm, introduced by the scanner thermal growth due to the environment temperature variation, can be minimized to the 1 nm uncertainty. Additionally, the analysis showed that the Abbé error can be reduced to the 0.8 nm uncertainty. The required resolution was difficult to achieve and the range to resolution issue was addressed. The current system was capable of making the 1.4 nm steps, which is defining its resolution.

As for designing for objectives of high resonance frequency and relatively large stroke, the design strategy for low mass coupled with the high stiffness and long stroke actuator was shown as valid. Additionally, the concept of compliant guidance coupled with the stiff actuator showed that the objectives for a low elastic stage deformation and yet reasonably high natural frequency are not necessarily mutually exclusive. Moreover, the deflection shaping of the stage frame decreased the actuation induced deformation. This reduced the inherent stage deformation induced measurement error by four times. Moreover, the structural optimization

of the scanner frame and the stiffening of the metrology brackets reduced the actuation induced deformation and the related error to a 1 nm level. The low deformation of the structural frame was also a result of low actuation forces used due to drive a small dynamic mass and low stiffness flexures. Extensive FEM modelling and optimization lead to a system with a minimum elastic deformation induced error, which without any compensation is below 6 nm. For comparison, the temperature variation of the temperature controlled environment contributes over 70 nm error.

The simultaneous optimization for the high resonance of both first and second resonance frequency yielded high resonances of 6 kHz and 8 kHz respectively. The first resonance was predicted by a coupled stage actuator model which spans a considerably large interval of predicted frequencies due to the variable characteristic of the piezoelectric actuator and its electromechanical coupling related stiffness. Both the models and the frequency response experiments confirmed the relationship of the piezoelectric actuator stiffness versus the amplitude of the voltage applied or the amplifier used. The measured first natural frequencies were in the anticipated range. The second mode was predicted within 2%, and it confirmed the design steps made to optimize for it to occur at sufficiently high frequencies. These were, for instance, the high movable frame box stiffness, large spacing between the bolting interfaces, stiffening effect of the metrology brackets and large chamfers designed, and stiffening efect of the protective cover. The last factor was proved by FEM analysis and validated experimentally. It follows from them, that a sliding fit cover which is sufficiently stiff adds more stiffness than mass to the stage assembly and thus inccreases the assembly's natural frequency.

Also, the squeeze film damping was predicted reasonably close (55%). The value of the damping measured implied, that the part of probe electrode area not overlaping with the target electrode plate contributed to the damping forces and hence should be taken into account when analyzing them. In addition, the adjustable sensing gap provided a useful and relatively simple way of adjusting the squeeze film damping forces and/or capacitive sensor sensitivity and noise if necessary.

The actuator placement in the stage by a flexure preload held it sufficiently and resulted in a compact solution. The design for high stress was robust enough to accommodate for manufacturing and actuator's dimensional tolerances when inserting it into the stage. The relatively large stroke actuator (20 μm) was not reduced due to the high flexures compliance relatively to the actuator stiffness. Moreover, the extra available stroke capability enabled faster closed loop operation, due to high overshoots possible and no actuator saturation. Additionally, operation at a fraction of the full actuator stoke shows lower ohmic heat generation, which was important for the stage temperature stability.

The capacitive sensor probe was designed and built. The sensor probe assembly fit the cut-out in the stage, so that the Abbé principle was obeyed. Additionally, the independent design capacitive probe did not impose any constraints on the flexural stage design, and vice versa. The commercial electronic demodulation circuit was used with the probe. Practical implementation issues of the sensor involved elimination of the grounding loops and sensor calibration by a laser interferometer.

The A-probe was chosen as the force sensor. The PCB boards for the 'pre-amplification'

of the probe signal and the 'self-oscillation and PLL' circuit with a phase locked loop were developed. The 'pre-amplification board' is specially integrated into the structural stage frame to make the electrical connections to the probe shorter and reduce the related parasitic effects. The quasi kinematic mount with a magnetic preload was designed and implemented. The pre-loading plate serves both as a mechanical probe preload and its electrical interface. The mount was tested with the A-probes for static conditions and provides a very simple and inexpensive solution.

The stage dynamics was identified by the frequency response experiments using the laser vibrometer and the position feedback sensor. The transfer function obtained via the laser vibrometer provided valuable knowledge about the system dynamics. The transfer function measured by the capacitive sensors showed that the modes other than the dominant resonant peak are unobservable. Based on this data a dynamic ARX model fit was developed. ARX model was further used to design the feedback controller. The controller was a PI control with a notch filter at 6 kHz resonant peak. It has been experimentally shown, that the stage can follow a sine input of over 10 μm peak to peak with a closed loop bandwidth higher than 2 kHz. As for the resolution, a clearly distinguishable 2.8 nm step can be made. The highest steps made by the stage were 13 μm. The controller is robust to accommodate the changing loop gain of the system depending on the distance travelled. An initially designed controller has a gain reduced by almost 30% for a sufficiently high phase margin (50°) at higher displacements (for 10 μm peak to peak sine input). This gain is also high enough to achieve the 2 kHz bandwidth at smaller displacement steps (order of 50 nm). The main limitation on the controlled bandwidth in the system was the time delay, affecting the achievebale stability margins.

6.2 Future work

Some future work must be done to meet the design requirements. As explained in Chapter 5, the temperature controlled environment and the temperature sensor should be implemented in the setup. In addition, the thermal expansion compensation described in Chapter 5 must be developed to reduce the stage thermal growth related error. Similarly, the straightness of the stage should be measured over a considerable amount of motion cycles to evaluate and compensate the Abbé and cosine errors, as explained in Chapter 5. As for the capacitive sensor, the noise floor present in the current research state must be reduced by, for example, an analogue low-pass post filter and/or by data averaging. The current research developed a working positioning stage which a kinematic mount for the selected Akiyama AFM probe. The PCB boards have been developed, however the first generation must still be tested. This will involve tuning of the potentiometer R7 on the 'pre-amplification' board which should balance the parasitic capacitance around the probe. Also the 'self-oscillating and PLL' board needs to be tuned for both the vibration amplitude adjustment, phase adjustment and the PLL oscillator tuning. If the probe is working, a new feedback loop should be built, so that the stage follows the probe's natural frequency setpoint. The setup needs to be calibrated statically (for instance by a reference vertical stage) to eliminate the probe inherent displacement and the related probe-sample force measurement error due to the stage elastic deformation.

6.3 Possible redesign

Any first generation of a designed instrument could be redesigned [17]. The future generations are developed to enhance the performance and/or to reduce machine overall cost [17]. The following section discusses possible improvements in the current setup, which should lead it. The feedback controller present in the current research was based on the identified transfer function model and was further tuned on-line. Experiments provided the knowledge of the system gain variation with the displacement travel and the controller gain was decreased to achieve the suitable stability and performance for the complete operation range of the stage. A more sophisticated control tools can be used to achieve better closed loop performance. The gain parameter variation could be obtained in a structural form and the H-infinity tools could be be used to design a synthesised controller of specified robust stability and performance [74]. Additionally, the quasi kinematic probe mount could be redesigned to achieve a higher stiffness mount. This involves both the positioning spheres on the stage, and the probe ceramic plate on the spheres interfaces. The first contact interface could be improved by making the cut-outs in the stage bottom face conical rather than a shaft shape. This would add more stiffness to the interface, since the spheres would rest tangently on the conical face. This provides more contact area than the line contact present in the current design. The A-probe magnetic mount design should additionally be improved to be hold the probe at higher frequencies and to provide better mounting stiffness. Even though a considerable amount of work was dedicated to this design, any better solution was not identified. Lastly, the capacitive demodulation system currently used could be replaced by a compact AC demodulation bridge which is placed on a single PCB [78]. This would significantly reduce the volume of the setup, which currently is mostly the size of large demodulation electronics box [1] and the reference capacitor system. The PCB board could be attached to the stage protective cover, which would result in an even more compact overall design.

Bibliography

[1] Ingenieursbureau-SensTech. Prototyoe capacitance meter 62.5 kHz. Lange Voort 233, 2343 CE Oegstgeest, The Netherlands;.

[2] Nanosensors;. http://www.akiyamaprobe.com.

[3] Binnig G, Quate CF, Gerber C. Atomic force microscope. Physical Review Letters. 1986;**56**(9):930 – 933.

[4] Danzebrink HU, Koenders L, Wilkening G, Yacoot A, Kunzmann H. Advances in Scanning Force Microscopy for Dimensional Metrology. CIRP Annals - Manufacturing Technology. 2006;**55**(2):841–878.

[5] Smith ST. Developments in Nanotechnology - Foundations of ultraprecision mechanism design. vol. **2**. Gordon and Breach Science Publishers; 1992.

[6] Yacoot A, Koenders L. topical review: Aspects of scanning force microscope probes and their effects on dimensional measurement. Journal of Physics D Applied Physics. 2008 May;**41**(10):103001–+.

[7] Jalili N, Laxminarayana K. A review of atomic force microscopy imaging systems: application to molecular metrology and biological sciences. Mechatronics. 2004;**8**(14):907–945.

[8] ParkAFM. XE Mode Note: basic contact AFM, Dynamic Force Microscope (DFM), basic topographic imaging. http://www.parkafm.com/publications; 2009.

[9] Giessibl FJ. Advances in atomic force microscopy. Reviews of Modern Physics. 2003;**75**(3):949–983.

[10] Abramovitch DY, Andersson SB, Pao LY, Schitter G. A Tutorial on the Mechanisms, Dynamics, and Control of Atomic Force Microscopes. In: Proceedings of the 2007 American Control Conference.; 2007. p. 3488–3502.

[11] Itoh T, Lee C, Suga T. Deflection detection and feedback actuation using a self excited piezoelectric Pb(Zr,Ti)O3 microcantilever for dynamic force microscopy. Applied Physics Letters. 1996;**69**(14):2036–2038.

[12] Itoh T, Suga T. Development of a force sensor for atomic force microscopy using piezoelectric thin films. Nanotechnology. 1993;**4**(4):218–224.

[13] Akiyama T, Staufer U, de Rooij N. Integrated atomic force microscopy array probe with metal-oxide-semiconductor field effect transistor stress sensor, thermal bimorph actuator, and on-chip complementary metal-oxidesemiconductor electronics. Journal of Vacuum Science and Technology B. 2000;**18**(6):2669–2675.

[14] Pedrak R, Ivanov T, Ivanova K, Gotszalk T, Abedinov N, Rangelow IW, et al. Micromachined atomic force microscopy sensor with integrated piezoresistive sensor and thermal bimorph actuator for high-speed tapping-mode atomic force microscopy phase-imaging in higher eigenmodes. Journal of Vacuum Science and Technology B: Microelectronics and Nanometer Structures. 2003;**21**(6):3102–3107.

[15] Blanc N, Brugger J, de Rooij NF, Dürig U. Scanning force microscopy in the dynamic mode using microfabricated capacitive sensors. Journal of Vacuum Science and Technology B. 1996;**14**(2):901–905.

[16] García R. Dynamic atomic force microscopy methods. Surface Science Reports. 2002;**47**(6-8):197–301.

[17] Buice ES. Implementation of a dynamic positioning machine for nano-scale engineering. The University of North Carolina at Charlotte; 2007.

[18] Sader JE. Susceptibility of atomic force microscope cantilevers to lateral forces. Review of Scientific Instruments. 2003;**74**(4):2438–2443.

[19] Beyder A, Sachs F. Microfabricated torsion levers optimized for low force and high-frequency operation in fluids. Ultramicroscopy. 2006;**106**(8-9):838 – 846. Proceedings of the Seventh International Conference on Scanning Probe Microscopy, Sensors and Nanostructures, Proceedings of the Seventh International Conference on Scanning Probe Microscopy, Sensors and Nanostructures.

[20] Pittenger B. HarmoniXTM Microscopy for Materials Characterization, application note. www.veeco.com/pdfs/appnotes; 2009.

[21] Sulchek T, Hsieh R, Adams JD, Yaralioglu GG, Minne SC, Quate CF, et al. High-speed tapping mode imaging with active Q control for atomic force microscopy. Applied Physics Letters. 2000;**76**(11):1473 –1475.

[22] Kawakatsu H, Kawai S, Saya D, Nagashio M, Kobayashi D, Toshiyoshi H, et al. Towards atomic force microscopy up to 100 MHz. Nature Reviews Microbiology. 2008;**6**(1):674–680.

[23] Walters DA, Cleveland JP, Thomson NH, Hansma PK, Wendman MA, Gurley G, et al. Short cantilevers for atomic force microscopy. Review of Scientific Instruments. 1996 Oct;**67**:3583–3590.

[24] Nanoworld;. http://www.nanoworld.com.

[25] Mazzeo AD, Stein AJ, Trumper DL, Hocken RJ. Atomic force microscope for accurate dimensional metrology. Precision Engineering. 2009;**33**(2):135 – 149.

[26] Fukuma T, Kimura M, Kobayashi K, Matsushige K, Yamada H. Development of low noise cantilever deflection sensor for multienvironment frequency-modulation atomic force microscopy. Review of Scientific Instruments. 2005;**76**(5):0537041–0537048.

[27] Erlandsson R, McClelland GM, Mate CM, Chiang S. Atomic force microscopy using optical interferometry. Journal of Vacuum Science and Technology A: Vacuum, Surfaces, and Films. 1988;**6**(2):266–270.

[28] Bentley JP. Principles of Measurement Systems. vol. **4**. Pearson Education Limited; 2005.

[29] Sasaki M, Hane K, Okuma S, Hino M, Bessho Y. Improved differential heterodyne interferometer for atomic force microscopy. Review of Scientific Instruments. 1994;.

[30] Schönenberger C, Alvarado SF. A differential interferometer for force microscopy. Review of Scientific Instruments. 1989;**60**:3131–3134.

[31] Oral A, Grimble RA, Özer HÖ, Pethica JB. High-sensitivity noncontact atomic force microscope/scanning tunneling microscope (nc AFM/STM) operating at subangstrom oscillation amplitudes for atomic resolution imaging and force spectroscopy. Review of Scientific Instruments. 2003;**74**:3656–3663.

[32] Ruf A, Abraham M, Diebel J, Ehrfeld W. Integrated Fabry-Perot distance control for atomic force microscopy. Journal of Vacuum Science and Technology B: Microelectronics and Nanometer Structures. 1997;**15**(3):579–585.

[33] Putman CAJ, de Grooth BG, van Hulst NF, Greve J. A theoretical comparison between interferometric and optical beam deflection technique for the measurement of cantilever displacement in AFM. Ultramicroscopy. 1992;**42-44**(Part 2):1509 – 1513.

[34] Putman CAJ, de Grooth BG, van Hulst NF, Greve J. A detailed analysis of the optical beam deflection technique for use in atomic force microscopy. Journal of Applied Physics. 1992;**72**(1):6–12.

[35] Tortonese M, Barrett RC, Quate CF. Atomic resolution with an atomic force microscope using piezoresistive detection. Applied Physics Letters. 1993;**62**:834–836.

[36] Rogers B, Manning L, Sulchek T, Adams JD. Improving tapping mode atomic force microscopy with piezoelectric cantilevers. Ultramicroscopy. 2004;**100**(3-4):267 – 276. Proceedings of the Fifth International Conference on Scanning Probe Micrscopy, Sensors and Nanostructures.

[37] Lee C, Itoh T, Suga T. Self-excited piezoelectric PZT microcantilevers for dynamic SFM–with inherent sensing and actuating capabilities. Sensors and Actuators A: Physical. 1999;**72**(2):179 – 188.

[38] Brugger J, Buser RA, de Rooij NF. Micromachined atomic force microprobe with integrated capacitive read-out. Journal of Micromechanics and Microengineering. 1992;**2**(3):218–220.

[39] Neubauer G, Cohen SR, McClelland GM, Horne D, Mate CM. Force microscopy with a bidirectional capacitance sensor. Review of Scientific Instruments. 1990;**61**:2296–2308.

[40] Watanabe S, Fujii T. Micro-fabricated piezoelectric cantilever for atomic force microscopy. Review of Scientific Instruments. 1996;**67**:3898–3903.

[41] Minne SC, Manalis SR, Quate CF. Parallel atomic force microscopy using cantilevers with integrated piezoresistive sensors and integrated piezoelectric actuators. Applied Physics Letters. 1995;**67**:3918–3920.

[42] Akiyama T, Staufer U, de Rooij NF, Frederix P, Engel A. Symmetrically arranged quartz tuning fork with soft cantilever for intermittent contact mode atomic force microscopy. Review of Scientific Instruments. 2003;**74**(1):112–117.

[43] Marcus RB, Ravi TS, Gmitter T, K C, Liu D, Orvis WJ, et al. Formation of silicon tips with 1 nm radius. Applied Physics Letters. 1990;**56**:236–238.

[44] Kwon J, Hong J, Kim YS, Lee DY, Lee K, min Lee S, et al. Atomic force microscope with improved scan accuracy, scan speed, and optical vision. Review of scientific instruments. 2003;**74**(10):4378–4383.

[45] Schitter G. Advanced Mechanical Design and Control Methods for Atomic Force Microscopy in Real-Time. In: American Control Conference 2007; 2007. p. 3503–3508.

[46] El Rifai OM, Youcef-Toumi K. In-contact dynamics of atomic force microscopes. In: International Conference on Advanced Intelligent Mechatronics 2000. Proceedings. vol. **2**; 2000. p. 1325–1328.

[47] El Rifai OM, Youcef-Toumi K. Design and control of atomic force microscopes. In: Proceedings of the 2003 American Control Conference. vol. **5**; 2003. p. 3714–3719.

[48] Tien S, Zou Q, Devasia S. Iterative control of dynamics coupling-caused errors in piezoscanners during high-speed AFM operations. IEEE Transactions on Control Systems Technology. 2005;**13**(6):921– 931.

[49] Ando T, Kodera N, Maruyama D, Takai E, Saito K, Toda A. A high-speed atomic force microscope for studying biological macromolecules. ChemPhysChem. 2003;**4**(11):1196 – 1202.

[50] Humphris AD, Miles MJ, Hobbs JK. A mechanical microscope: High-speed atomic force microscopy. Applied Physics Letters. 2005;**86**(3):341061–341063.

[51] Fantner GE, Schitter G, Kindt JH, Ivanov T, Ivanova K, Patel R, et al. Components for high speed atomic force microscopy. Ultramicroscopy. 2006;**106**(8-9):881 – 887. Proceedings of the Seventh International Conference on Scanning Probe Microscopy, Sensors and Nanostructures, Proceedings of the Seventh International Conference on Scanning Probe Microscopy, Sensors and Nanostructures.

[52] Kindt JH, Fantner GE, Cutroni JA, Hansma PK. Rigid design of fast scanning probe microscopes using finite element analysis. Ultramicroscopy. 2004;**100**(3-4):259–265.

[53] Salapaka S, Sebastian A, Cleveland JP, Salapaka MV. High bandwidth nano-positioner: A robust control approach. Review of Scientific Instruments. 2002;**73**(9):3232–3241.

[54] Schitter G, Astrom KJ, DeMartini BE, Thurner PJ, Turner KL, Hansma PK. Design and Modeling of a High-Speed AFM-Scanner. IEEE Transactions on Control Systems Technology. 2007;**15**(5):906–915.

[55] Salapaka S, De T, Sebastian A. Sample-profile estimate for fast atomic force microscopy. Applied Physics Letters. 2005;**87**(5):053112.

[56] DIT-Holland;. http://www.ditholland.nl.

[57] Powermagnetshop;. http://www.powermagnetshop.de.

[58] AustralianMagneticSolutions;. http://www.magneticsolutions.com.au.

[59] KJ-magntentics;. http://www.kjmagnetics.com/calculator.

[60] Smith ST. Flexures. Elements of Elastic Mechanisms. CRC Press; 2000.

[61] PhysikInstrumente. Piezo University: tutorial;. http://www.physikinstrumente.com.

[62] Americanpiezo;. http://www.americanpiezo.com.

[63] Tsuji T, Saito S, Fukuda K, Yamanaka K, Ogiso H, Akedo J, et al. Significant stiffness reduction at ferroelectric domain boundary evaluated by ultrasonic atomic force microscopy. Applied Physics Letters. 2005;**87**(7):071909 –071909–3.

[64] Piezomechanik. Electronic supplies for piezomechanics: An introduction;. http://www.piezomechanik.com.

[65] Matweb;. http://www.matweb.com.

[66] Smith ST, Seugling RM. Sensor and actuator considerations for precision, small machines. Precision Engineering. 2006;**30**(3):245 – 264.

[67] Capacitive Sensor Operation and Optimization - technical note. Lion Precision;.

[68] Bao M, Yang H. Squeeze film air damping in MEMS. Sensors and Actuators A: Physical. 2007;**136**(1):3 – 27. 25th Anniversary of Sensors and Actuators A: Physical.

[69] Darling RB, Hivick C, Xu J. Compact analytical modeling of squeeze film damping with arbitrary venting conditions using a Green's function approach. Sensors and Actuators A: Physical. 1998;**70**(1-2):32 – 41.

[70] Croft D, Shed G, Devasia S. Creep, Hysteresis, and Vibration Compensation for Piezoactuators: Atomic Force Microscopy Application. Journal of Dynamic Systems, Measurement, and Control. 2001;**123**.

[71] Wesseling J. Multisine MATLAB toolbox;.

[72] Byle K, Trumper D. DSA1103 signal analyzer toolbox;.

[73] Skogestad S. Probably the best simple PID tuning rules in the world; 2001. www.eq.ufrj.br.

[74] Skogestad S. Multivariable Feedback Control. Wiley; 1996.

[75] Cox M, Harris M. Software Support for Metrology Best Practice Guide No. 6 - Uncertainty Evaluation. National Physical Laboratory, Hampton Road, Teddington, Middlesex, United Kingdom; 2006.

[76] GUM. Evaluation of measurement data — Guide to the expression of uncertainty in measurement. Joint Committee for Guides in Metrology; 2008.

[77] Doiron T, Stoup J. Uncertainty and Dimensional Calibrations. Journal of Research of the National Institute of Standards and Technology;**102**.

[78] InsituTec;. I45 Odell School Rd. Suite A, Concord, NC 28027, North Carolina.

Appendix A

Technical drawings

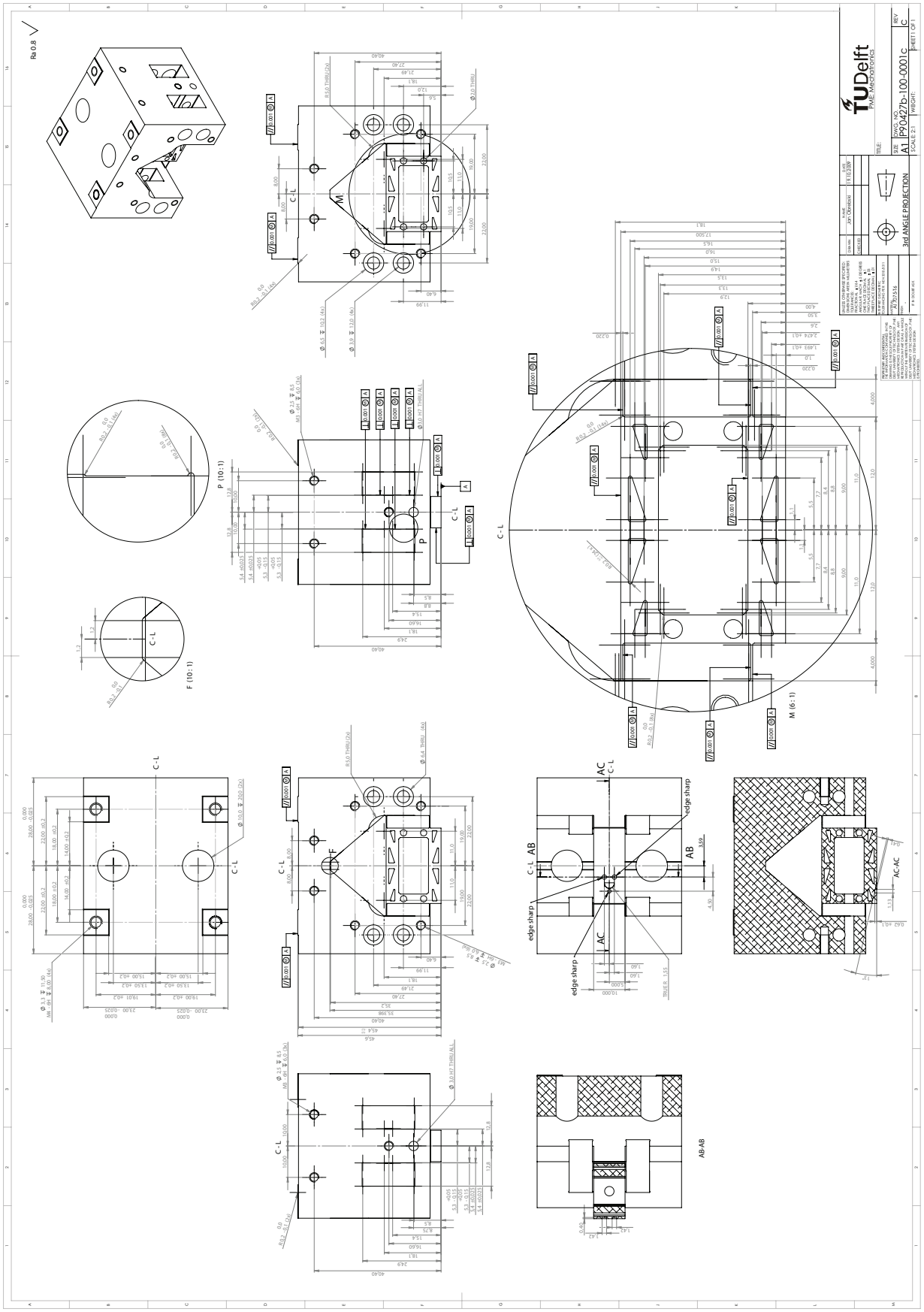
TUDelft
PME-MECHATRONICS
DWG. NO. P90427b-100-0001c
REV C
SIZE A1
SCALE 2:1
WEIGHT
SHEET 1 OF 1
3rd ANGLE PROJECTION
TITLE
M (6:1)
P (10:1)
F (10:1)
AB-AB
AC-AC
edge sharp
C-L

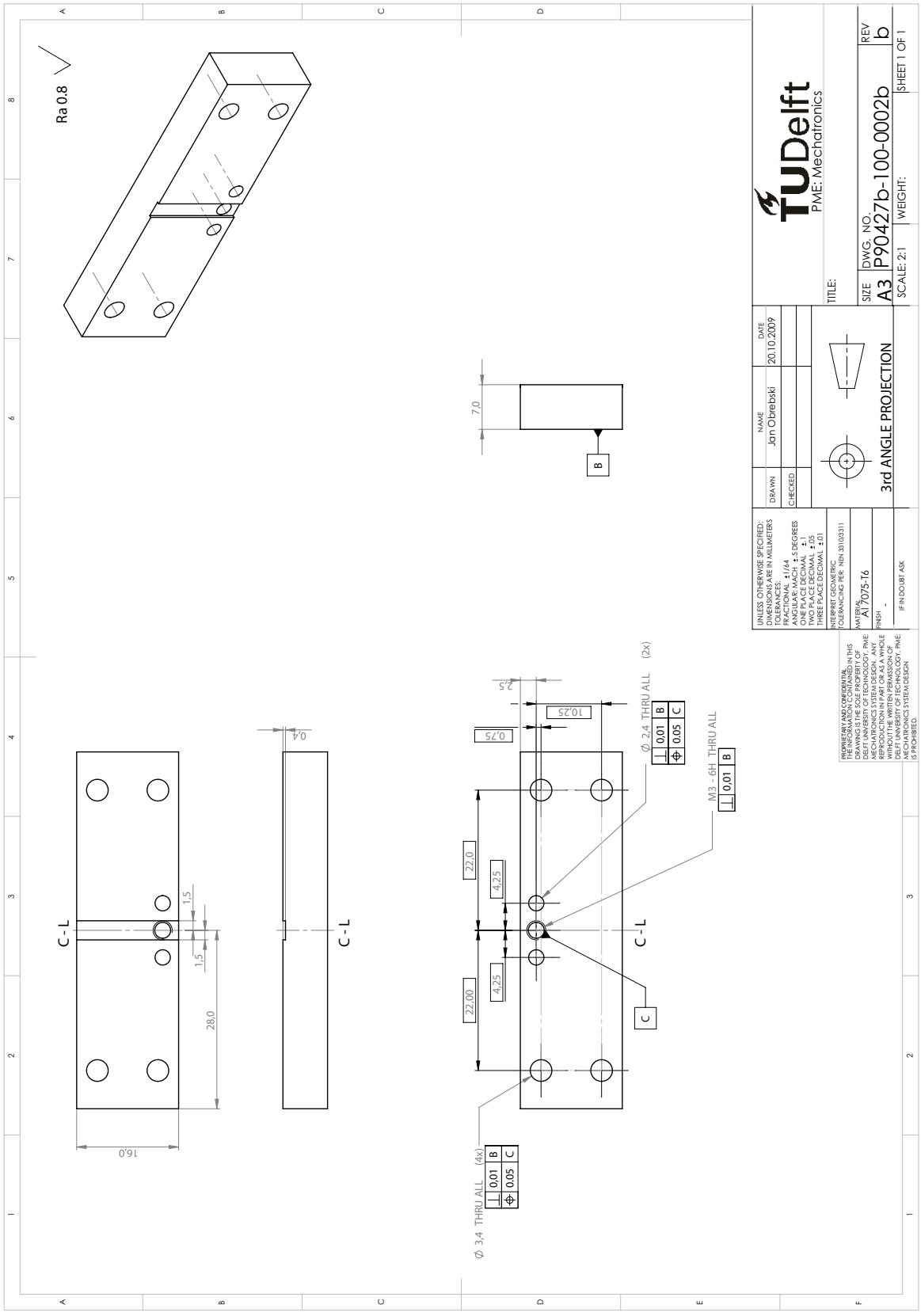
Ra 0.8
7,0
B
C - L
16,0
1,5
1,5
28,0
0,4
C - L
2,5
10,25
0,75
22,0
4,25
4,25
22,00
C - L
Ø 2,4 THRU ALL (2x)
⊥ 0,01 B
⌖ 0,05 C
M3 - 6H THRU ALL
⊥ 0,01 B
C
Ø 3,4 THRU ALL (4x)
⊥ 0,01 B
⌖ 0,05 C
UNLESS OTHERWISE SPECIFIED:
DIMENSIONS ARE IN MILLIMETERS
TOLERANCES:
FRACTIONAL ± 1/64
ANGULAR: MACH ± 5 DEGREES
ONE PLACE DECIMAL ± .1
TWO PLACE DECIMAL ± .05
THREE PLACE DECIMAL ± .01
INTERPRET GEOMETRIC
TOLERANCING PER: ASME Y14.5M-1994
MATERIAL
Al 7075-T6
FINISH
-
DRAWN
CHECKED
NAME
Jan Obrebski
DATE
20.10.2009
TITLE:
3rd ANGLE PROJECTION
SIZE
A3
DWG. NO.
P90427b-100-0002b
REV
b
SCALE: 2:1
WEIGHT:
SHEET 1 OF 1
IF IN DOUBT ASK
TUDelft
PME: Mechatronics
PROPRIETARY AND CONFIDENTIAL
THE INFORMATION CONTAINED IN THIS
DRAWING IS THE SOLE PROPERTY OF
DELFT UNIVERSITY OF TECHNOLOGY, PME
MECHATRONICS SYSTEM DESIGN. ANY
REPRODUCTION IN PART OR AS A WHOLE
WITHOUT THE WRITTEN PERMISSION OF
DELFT UNIVERSITY OF TECHNOLOGY, PME
MECHATRONICS SYSTEM DESIGN
IS PROHIBITED.

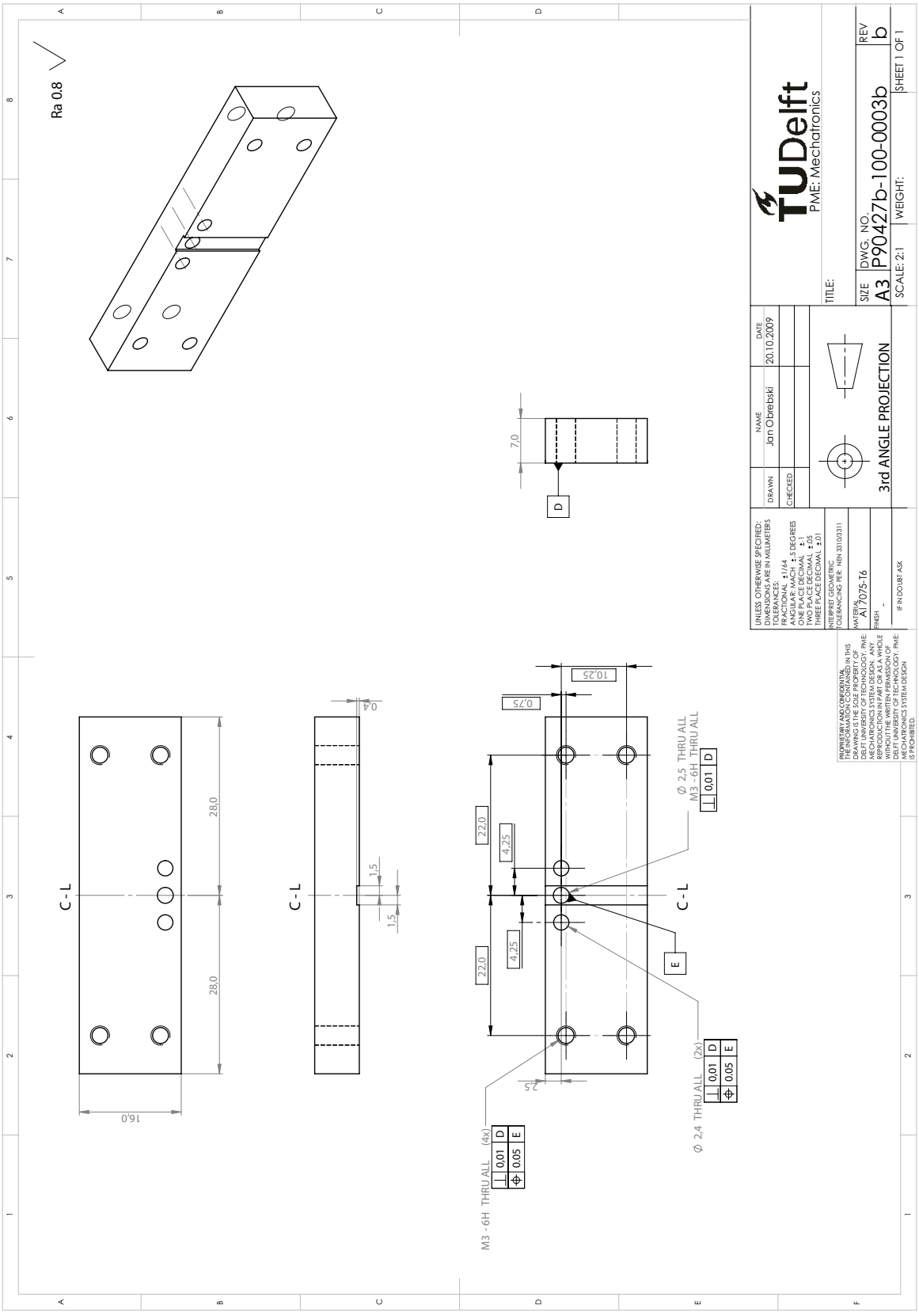
Ra 0.8
C - L
28.0
28.0
16.0
1.5
1.5
0.4
10.25
0.75
22.0
4.25
4.25
22.0
2.5
Ø 2.5 THRU ALL
M3 - 6H THRU ALL
⊥ 0.01 D
Ø 2.4 THRU ALL (2x)
⊥ 0.01 D
⌖ 0.05 E
M3 - 6H THRU ALL (4x)
⊥ 0.01 D
⌖ 0.05 E
7.0
D
E
UNLESS OTHERWISE SPECIFIED:
DIMENSIONS ARE IN MILLIMETERS
TOLERANCES:
FRACTIONAL ± 1/64
ANGULAR: MACH ± 5 DEGREES
ONE PLACE DECIMAL ± .1
TWO PLACE DECIMAL ± .05
THREE PLACE DECIMAL ± .01
INTERPRET GEOMETRIC
TOLERANCING PER: ASN 31.10.0311
MATERIAL
Al 7075-T6
FINISH
-
DRAWN
CHECKED
NAME
Jan Otrebski
DATE
20.10.2009
3rd ANGLE PROJECTION
TITLE:
TUDelft
PME: Mechatronics
SIZE
A3
DWG. NO.
P90427b-100-0003b
REV
b
SCALE: 2:1
WEIGHT:
SHEET 1 OF 1
IF IN DOUBT ASK
PROPRIETARY AND CONFIDENTIAL
THE INFORMATION CONTAINED IN THIS
DRAWING IS THE SOLE PROPERTY OF
DELFT UNIVERSITY OF TECHNOLOGY, PME
MECHATRONICS SYSTEM DESIGN. ANY
REPRODUCTION IN PART OR AS A WHOLE
WITHOUT THE WRITTEN PERMISSION OF
DELFT UNIVERSITY OF TECHNOLOGY, PME
MECHATRONICS SYSTEM DESIGN
IS PROHIBITED.

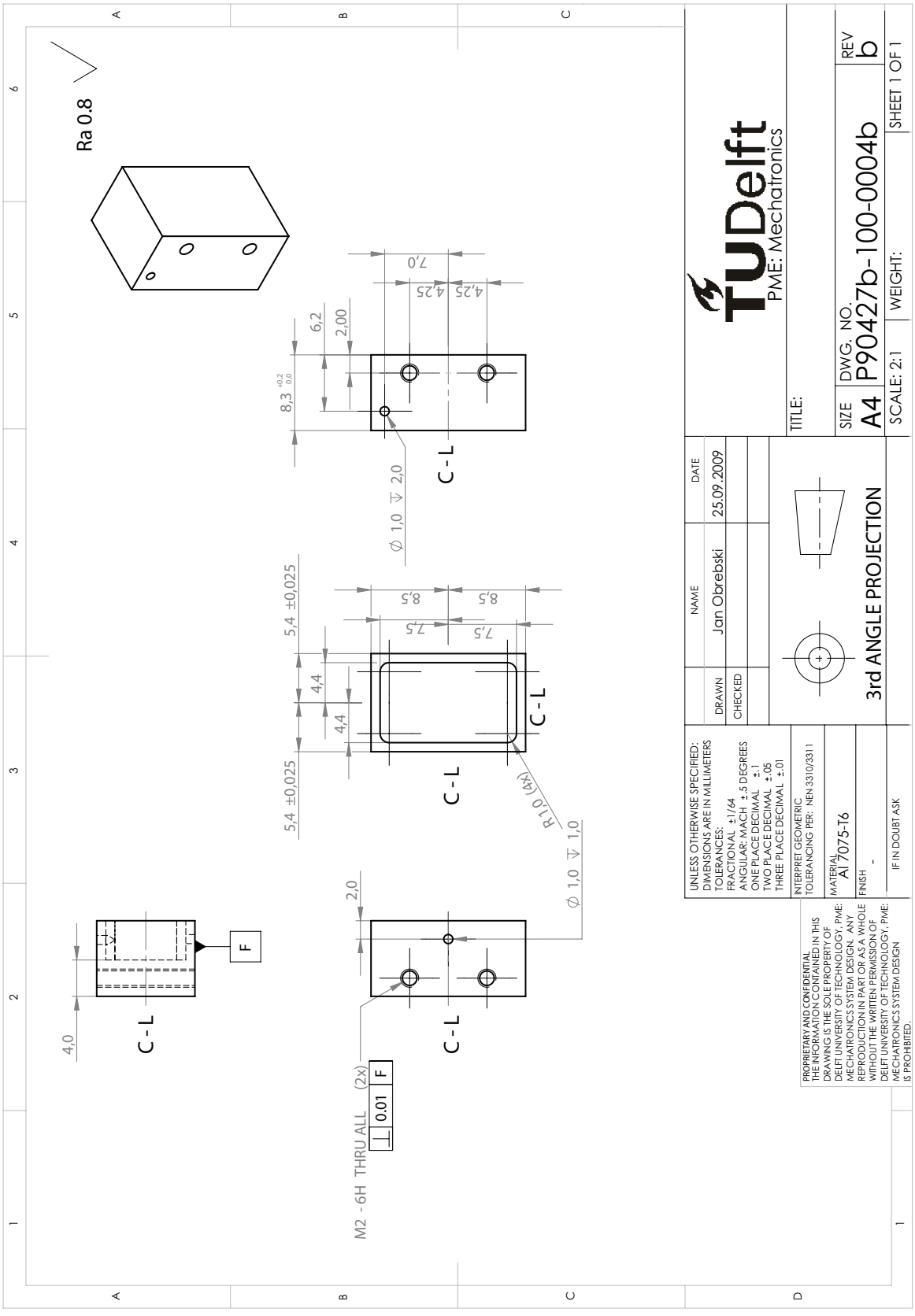
Ra 0.8
M2 - 6H THRU ALL (2x)
⊥ 0.01 F
C - L
F
4,0
2,0
Ø 1,0 ↧ 1,0
R1,0 (4x)
5,4 ±0,025
4,4
8,5
7,5
8,3 +0,2 0,0
6,2
2,00
4,25
7,0
Ø 1,0 ↧ 2,0
TUDelft
PME: Mechatronics
TITLE:
SIZE A4
DWG. NO. P90427b-100-0004b
REV b
SCALE: 2:1
WEIGHT:
SHEET 1 OF 1
NAME
DATE
DRAWN Jan Obrebski 25.09.2009
CHECKED
3rd ANGLE PROJECTION
UNLESS OTHERWISE SPECIFIED:
DIMENSIONS ARE IN MILLIMETERS
TOLERANCES:
FRACTIONAL ±1/64
ANGULAR: MACH ±.5 DEGREES
ONE PLACE DECIMAL ±.1
TWO PLACE DECIMAL ±.05
THREE PLACE DECIMAL ±.01
INTERPRET GEOMETRIC
TOLERANCING PER: NEN 3310/3311
MATERIAL
Al 7075-T6
FINISH
-
IF IN DOUBT ASK
PROPRIETARY AND CONFIDENTIAL
THE INFORMATION CONTAINED IN THIS
DRAWING IS THE SOLE PROPERTY OF
DELFT UNIVERSITY OF TECHNOLOGY, PME:
MECHATRONICS SYSTEM DESIGN. ANY
REPRODUCTION IN PART OR AS A WHOLE
WITHOUT THE WRITTEN PERMISSION OF
DELFT UNIVERSITY OF TECHNOLOGY, PME:
MECHATRONICS SYSTEM DESIGN
IS PROHIBITED.

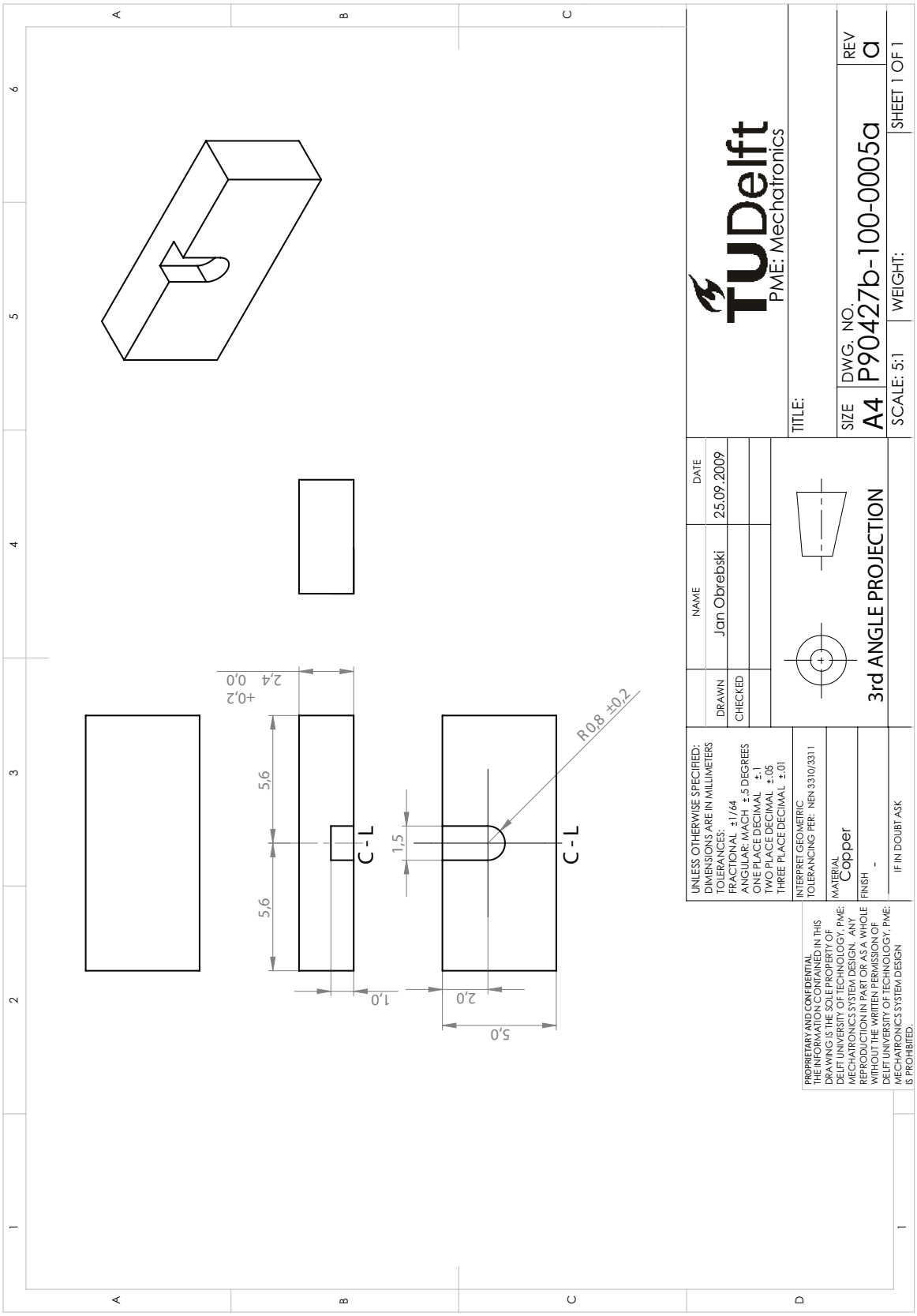
2,4 +0,2 0,0
5,6
5,6
C - L
1,5
R0,8 ±0,2
C - L
1,0
2,0
5,0
UNLESS OTHERWISE SPECIFIED:
DIMENSIONS ARE IN MILLIMETERS
TOLERANCES:
FRACTIONAL ±1/64
ANGULAR: MACH ±.5 DEGREES
ONE PLACE DECIMAL ±.1
TWO PLACE DECIMAL ±.05
THREE PLACE DECIMAL ±.01
INTERPRET GEOMETRIC
TOLERANCING PER: NEN 3310/3311
MATERIAL
Copper
FINISH
-
IF IN DOUBT ASK
PROPRIETARY AND CONFIDENTIAL
THE INFORMATION CONTAINED IN THIS
DRAWING IS THE SOLE PROPERTY OF
DELFT UNIVERSITY OF TECHNOLOGY, PME:
MECHATRONICS SYSTEM DESIGN. ANY
REPRODUCTION IN PART OR AS A WHOLE
WITHOUT THE WRITTEN PERMISSION OF
DELFT UNIVERSITY OF TECHNOLOGY, PME:
MECHATRONICS SYSTEM DESIGN
IS PROHIBITED.
NAME
DATE
DRAWN
Jan Obrebski
25.09.2009
CHECKED
3rd ANGLE PROJECTION
TITLE:
TUDelft
PME: Mechatronics
SIZE
A4
DWG. NO.
P90427b-100-0005a
REV
a
SCALE: 5:1
WEIGHT:
SHEET 1 OF 1

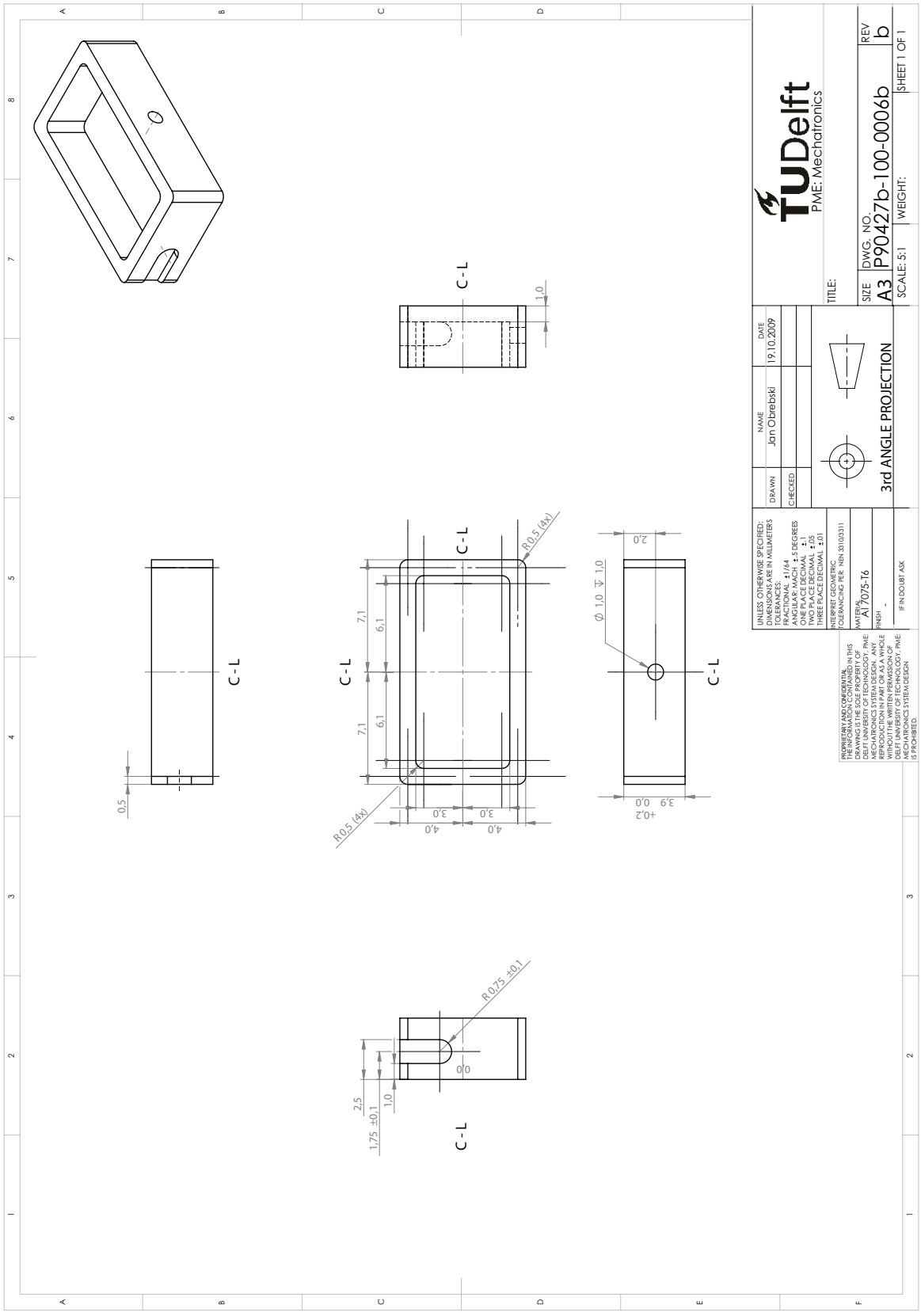
TUDelft
PME: Mechatronics
TITLE:
SIZE A3
DWG. NO. P90427b-100-0006b
REV b
SCALE: 5:1
WEIGHT:
SHEET 1 OF 1
3rd ANGLE PROJECTION
DRAWN Jan Obrebski 19.10.2009
CHECKED
UNLESS OTHERWISE SPECIFIED:
DIMENSIONS ARE IN MILLIMETERS
TOLERANCES:
FRACTIONAL ±1/64
ANGULAR: MACH ± .5 DEGREES
ONE PLACE DECIMAL ±.1
TWO PLACE DECIMAL ±.05
THREE PLACE DECIMAL ±.01
INTERPRET GEOMETRIC TOLERANCING PER: ASME Y14.5M-1994
MATERIAL Al 7075-T6
FINISH -
DO NOT SCALE DRAWING
IF IN DOUBT ASK
PROPRIETARY AND CONFIDENTIAL
THE INFORMATION CONTAINED IN THIS DRAWING IS THE SOLE PROPERTY OF DELFT UNIVERSITY OF TECHNOLOGY, PME. ANY REPRODUCTION IN PART OR AS A WHOLE WITHOUT THE WRITTEN PERMISSION OF DELFT UNIVERSITY OF TECHNOLOGY, PME. MECHATRONICS SYSTEM DESIGN IS PROHIBITED.
C - L
R0.5 (4x)
R0.75 ±0.1
Ø 1.0 ⩛ 1.0
+0.2 3.9 0.0
4.0
3.0
7.1
6.1
2.5
1.75 ±0.1
1.0
0.5
2.0

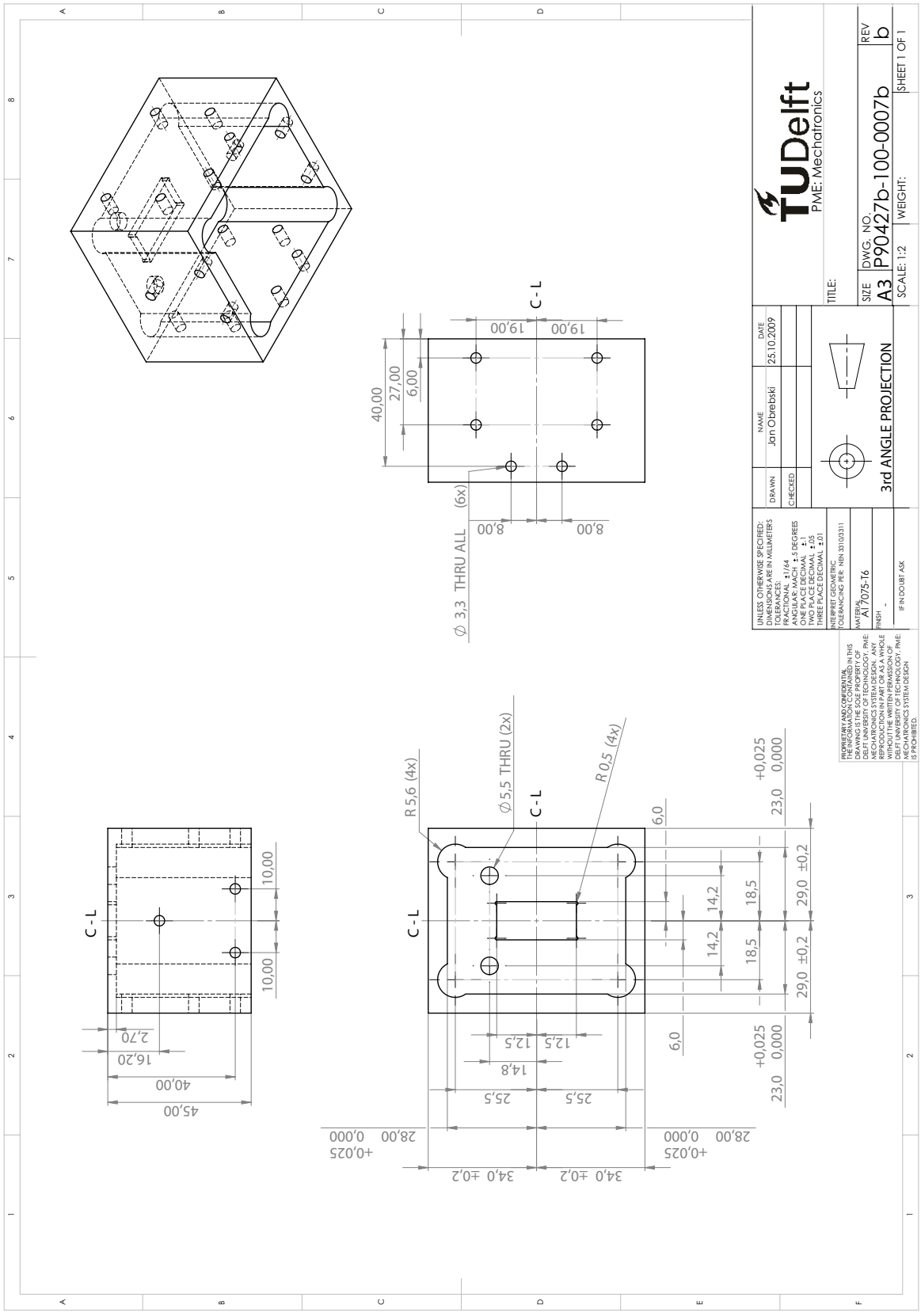
TUDelft
PME: Mechatronics
TITLE:
SIZE A3
DWG. NO. P90427b-100-0007b
REV b
SCALE: 1:2
WEIGHT:
SHEET 1 OF 1
3rd ANGLE PROJECTION
DRAWN Jan Olbrebski 25.10.2009
CHECKED
UNLESS OTHERWISE SPECIFIED:
DIMENSIONS ARE IN MILLIMETERS
TOLERANCES:
FRACTIONAL ± 1/64
ANGULAR: MACH ± .5 DEGREES
ONE PLACE DECIMAL ± .1
TWO PLACE DECIMAL ± .05
THREE PLACE DECIMAL ± .01
INTERPRET GEOMETRIC TOLERANCING PER: ASME Y14.5M-1994
MATERIAL Al 7075-T6
FINISH -
DO NOT SCALE DRAWING
IF IN DOUBT ASK
PROPRIETARY AND CONFIDENTIAL
THE INFORMATION CONTAINED IN THIS DRAWING IS THE SOLE PROPERTY OF DELFT UNIVERSITY OF TECHNOLOGY, PME. ANY REPRODUCTION IN PART OR AS A WHOLE WITHOUT THE WRITTEN PERMISSION OF DELFT UNIVERSITY OF TECHNOLOGY, PME. MECHATRONICS SYSTEM DESIGN IS PROHIBITED.
C - L
40,00
27,00
6,00
19,00
19,00
8,00
8,00
Ø 3,3 THRU ALL (6x)
R 5,6 (4x)
Ø 5,5 THRU (2x)
R 0,5 (4x)
6,0
14,2
14,2
18,5
18,5
29,0 ±0,2
29,0 ±0,2
23,0 +0,025 0,000
23,0 +0,025 0,000
12,5
12,5
14,8
25,5
25,5
28,00 +0,025 0,000
28,00 +0,025 0,000
34,0 ±0,2
34,0 ±0,2
10,00
10,00
2,70
16,20
40,00
45,00

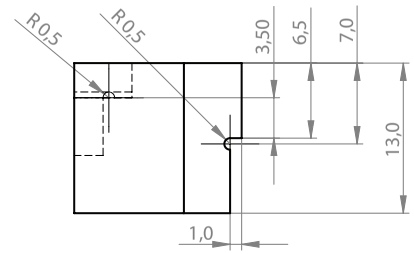

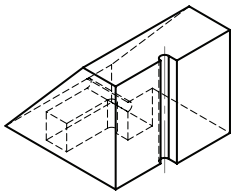

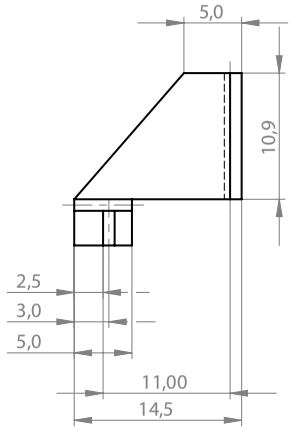

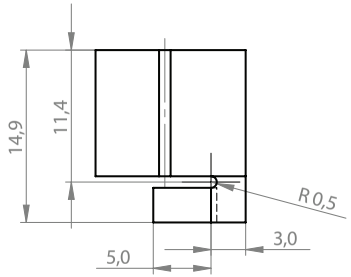

UNLESS OTHERWISE SPECIFIED: DIMENSIONS ARE IN MILLIMETERS TOLERANCES: FRACTIONAL ±1/64 ANGULAR: MACH ±.5 DEGREES ONE PLACE DECIMAL ±.1 TWO PLACE DECIMAL ±.05 THREE PLACE DECIMAL ±.01		NAME / DATE
	DRAWN	Jan Obrebski / 25.09.2009
	CHECKED	
INTERPRET GEOMETRIC TOLERANCING PER: NEN 3310/3311		
MATERIAL Al 7075-T6		
FINISH -		
IF IN DOUBT ASK		

3rd ANGLE PROJECTION

TUDelft
PME: Mechatronics

TITLE:

SIZE	DWG. NO.	REV
A4	P90427b-100-0008b	b

SCALE: 2:1 | WEIGHT: | SHEET 1 OF 1

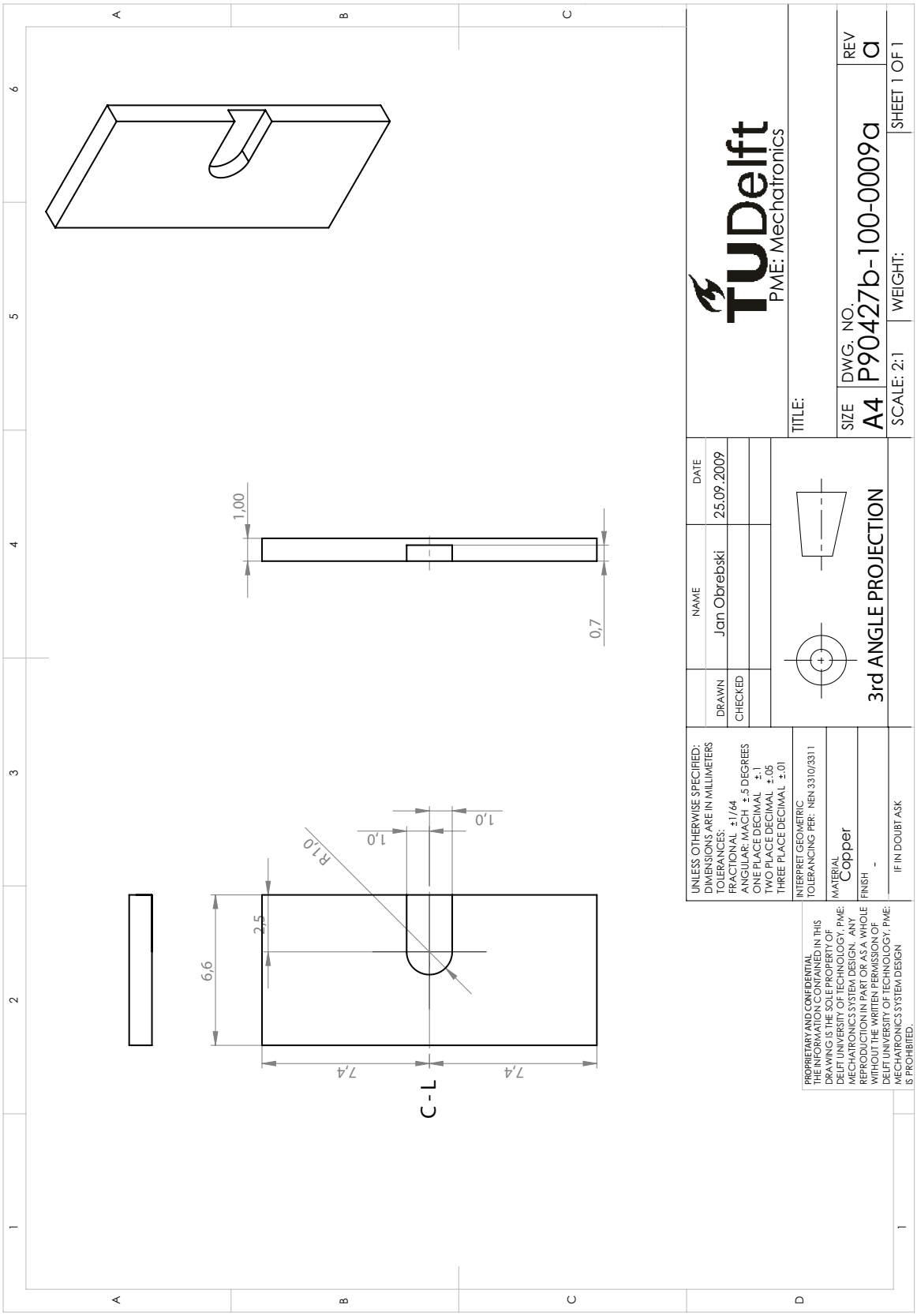
1,00
0,7
R1,0
1,0
1,0
2,5
6,6
7,4
7,4
C - L
UNLESS OTHERWISE SPECIFIED:
DIMENSIONS ARE IN MILLIMETERS
TOLERANCES:
FRACTIONAL ±1/64
ANGULAR: MACH ±.5 DEGREES
ONE PLACE DECIMAL ±.1
TWO PLACE DECIMAL ±.05
THREE PLACE DECIMAL ±.01
INTERPRET GEOMETRIC
TOLERANCING PER: NEN 3310/3311
MATERIAL
Copper
FINISH
-
IF IN DOUBT ASK
DRAWN
CHECKED
NAME
Jan Obrebski
DATE
25.09.2009
3rd ANGLE PROJECTION
TITLE:
SIZE
A4
DWG. NO.
P90427b-100-0009a
REV
a
SCALE: 2:1
WEIGHT:
SHEET 1 OF 1
TUDelft
PME: Mechatronics
PROPRIETARY AND CONFIDENTIAL
THE INFORMATION CONTAINED IN THIS
DRAWING IS THE SOLE PROPERTY OF
DELFT UNIVERSITY OF TECHNOLOGY, PME:
MECHATRONICS SYSTEM DESIGN. ANY
REPRODUCTION IN PART OR AS A WHOLE
WITHOUT THE WRITTEN PERMISSION OF
DELFT UNIVERSITY OF TECHNOLOGY, PME:
MECHATRONICS SYSTEM DESIGN
IS PROHIBITED.

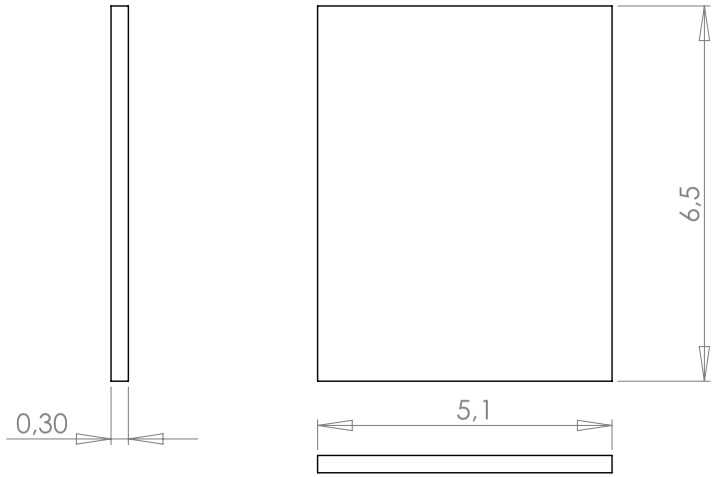

UNLESS OTHERWISE SPECIFIED: DIMENSIONS ARE IN MILLIMETERS TOLERANCES: FRACTIONAL ±1/64 ANGULAR: MACH ±.5 DEGREES ONE PLACE DECIMAL ±.2 TWO PLACE DECIMAL ±.05 THREE PLACE DECIMAL ±.01		
INTERPRET GEOMETRIC TOLERANCING PER: NEN 3310/3311		
MATERIAL Stainless Steel 431		
FINISH -		
IF IN DOUBT ASK		

	NAME	DATE
DRAWN	Jan Obrebski	30.09.2009
CHECKED		

3rd ANGLE PROJECTION

TUDelft
PME: Mechatronics

TITLE:

SIZE	DWG. NO.	REV
A4	P90427b-100-00010d	d

SCALE: 20:1	WEIGHT:	SHEET 1 OF 1

Appendix B

Proceedings of the euspen International Conference - Delft - June 2010

Acknowledgements

First of all, I would like to express my sincere gratitude to my supervisors, Mr. Eric S. Buice, Mr. Jonathan Ellis, and Mr. Jo Spronck for all their support, excellent coaching and research enthusiasm. I also wish to thank prof. Rob Munnig Schmidt for his help and co-authorship of eu**spen** conference proceedings where my research has been published. My words of gratitude go to Mr. Muammer Ozbek, Mr. Rik van den Hoeven, Mr. Piet van Rens, Mr. Jeroen van Schieveen, Mr. Rudolf Saathof, Mr. Friedjof Heuck, Mr. Alexander Steenhoek, Mr. Jasper Wesselingh, Mr. Rob Luttjeboer, Mr. Harry F.L. Jansen, and Mr. Patrick van Holst. I wish to thank Mr. Paolo Tiso for agreeing to be part of my examination committee. I would like to thank Shell Group and Delft University of Technology for awarding me The Shell Centenary Scholarship Fund scholarship. Last but not least, I wish to thank my family for all their love and support.